ADAPTIVE HOT-SPOT COOLING OF INTEGRATED CIRCUITS USING DIGITAL MICROFLUIDICS
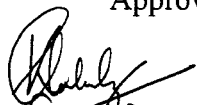
by

Philip Y. Paik
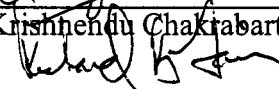
Department of Electrical and Computer Engineering
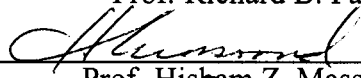Duke University

Date: _April 25, 2006_

Approved:

_____
Prof. Krishnendu Chakrabarty, Advisor

_____
Prof. Richard B. Fair

_____
Prof. Hisham Z. Massoud

_____
Dr. Vamsee K. Pamula

_____
Dr. Pradip Bose

Dissertation submitted in partial fulfillment of the
requirements for the degree of Doctor of Philosophy
in the Department of Electrical and Computer Engineering
in the Graduate School of
Duke University

2006

UMI Number: 3271003

INFORMATION TO USERS

The quality of this reproduction is dependent upon the quality of the copy submitted. Broken or indistinct print, colored or poor quality illustrations and photographs, print bleed-through, substandard margins, and improper alignment can adversely affect reproduction.

In the unlikely event that the author did not send a complete manuscript and there are missing pages, these will be noted. Also, if unauthorized copyright material had to be removed, a note will indicate the deletion.

UMI®

ABSTRACT

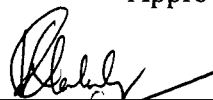(Engineering—Electrical and Computer)

ADAPTIVE HOT-SPOT COOLING OF INTEGRATED CIRCUITS USING DIGITAL MICROFLUIDICS
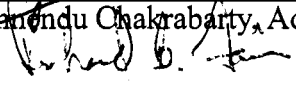
by

Philip Y. Paik

Department of Electrical and Computer Engineering
Duke University

Date: _____April 25, 2006_____

Approved:

_____
Prof. Krishnendu Chakrabarty, Advisor

_____
Prof. Richard B. Fair

_____
Prof. Hisham Z. Massoud
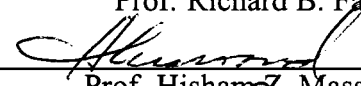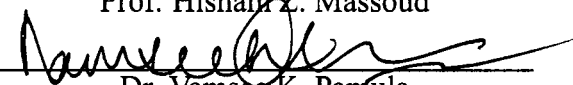
_____
Dr. Vamsee K. Pamula

_____
Dr. Pradip Bose

An abstract of a dissertation submitted in partial
fulfillment of the requirements for the degree
of Doctor of Philosophy in the Department of
Electrical and Computer Engineering in the Graduate School of
Duke University

2006

Abstract

Thermal management is a critical issue in integrated circuit (IC) design. With each new IC technology generation, feature sizes decrease,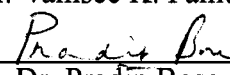 while operating speeds and package densities increase. These factors contribute to elevated die temperatures detrimental to circuit performance and reliability. Furthermore, hot-spots due to spatially non-uniform heat flux in ICs can cause physical stress that further reduces reliability. A number of techniques to address these issues have been proposed to date, yet most are unable to handle the varying thermal profile of an IC due to their inherent lack of reconfigurability.

In this thesis, we introduce two alternative cooling architectures based upon a "digital microfluidic" platform. In a flow-through approach, cooling droplets are actuated independently via electrowetting through user-defined reprogrammable flow paths and speeds. This high level of reconfigurability enables us to create an "adaptive" hot-spot cooling module that can be affixed directly onto the IC itself, whereby the system reconfigures itself on-the-fly in response to a changing thermal profile. In a programmable thermal switch approach, an array of liquid-metal droplets can be manipulated such that any area in the cooling device can be selectively switched from a low-to-high or high-to-low thermal conductivity mode. In this way, a higher heat flux can be drawn away from the hot-spot, resulting in a uniform thermal profile.

This thesis first studies the temperature-dependent behavior of digital microfluidic systems. It is shown that the transport of droplets immersed in oil is facilitated at elevated temperatures. Various hot-spot cooling prototypes were designed, based on a coplanar electrowetting scheme developed to simplify fabrication and assembly steps. For flow-through based systems, cooling prototypes were used to demonstrate the closed-loop dispensing, transport, and recycling of droplets necessary for adaptive cooling. Heat transfer using moving droplets is shown to improve significantly for higher mass flow rates and heat

flux densities. However, while the proof-of-concept for this flow-through technique was successfully demonstrated, the maximum flow-rates using current prototypes appear to be insufficient in view of the high heat-flux densities in today's IC devices. Future studies of alternative dielectric materials will help to overcome these limits.

For a programmable thermal switch-based architecture, heat transfer parameters of mercury droplets were studied in both steady-state and transient conditions, in which the cooling of hot-spots was shown to be dependent on parameters such as effective cooling areas and the number of conductive vias. These parameters are manipulated on-the-fly to create a non-uniform thermal conductance layer corresponding to the thermal profile of the IC substrate. The ability to manipulate a dense array of these liquid-metal droplets in response to changing heat-flux densities allows for a completely self-automated adaptive cooling system.

The work presented in this thesis addresses the fundamental design challenges in developing an adaptive cooling architecture based on the digital microfluidic platform. The two cooling methods developed and characterized here demonstrate the feasibility to adaptively perform thermal management to dynamically cool hot-spots. Such an adaptive hot-spot cooling system will pave the way for new IC thermal management design strategies to perform temperature-aware cooling.

Acknowledgements

Contents

List of Tables

List of Figures

xix

Chapter 1

Background and Motivation

1.1 Introduction

Thermal management is an increasingly important issue in integrated circuit (IC) design. Decreasing feature sizes, increasing operating frequencies, and increasing package densities of ICs will soon render current package-level cooling techniques inadequate. Poor thermal design and management often results in overheating, which, according to recent statistics, accounts for a large portion of field failures. In addition, it has been predicted in the 2003 International Technology Roadmap for Semiconductors (ITRS) that the peak power consumption of high-performance desktops will jump by 92% (150W to 288W) in 2014, and by 95% (81W to 158W) in lower-end desktops in 2016 [9].

High die temperatures and non-uniform thermal distributions in ICs are known to cause a number of problems. For example, the mean-time-to-failure due to electromigration decreases exponentially with increasing temperatures. MOS transistor drive capability is found to decrease almost 4% for every 10°C rise in temperature, whereas interconnect delay increases at the same rate [10], resulting in performance degradation. Furthermore, an uneven thermal distribution (i.e., "hot-spots") within the die can result in chip failure due to physical stress.

While various techniques have been explored to reduce power consumption, and thus heat dissipation, in ICs [11, 12], power consumption for these ICs continues to increase. This is being largely driven by higher operating frequencies, increased gate leakage, higher overall capacitances, and larger chip size. IC design engineers can no longer rely only on design techniques for low power. Similarly, traditional thermal management techniques, which address heat transfer issues at the packaging level, will no longer be adequate. Such

methods are already inadequate for portable, battery-operated systems that require compact packaging. Even at reduced operating voltages, the predicted growth rate of functionality per chip will require substantially more power than supported by known thermal packaging options. New techniques are therefore needed to develop embedded cooling methods, methods for IC-level integration of thermal sensors and heat sinks, and systematic synthesis techniques for ICs that contain embedded heat dissipation mechanisms.

To date, a number of novel techniques to address these issues has been proposed, many of which are leaning toward microfluidic solutions. For example, a closed-loop two-phase microchannel cooling system based on electroosmotic pumping of liquids has been developed at Stanford, whereby an electroosmotic pump is connected to a microchannel heat exchanger, which in turn is connected to a heat rejecter [5]. Researchers at Georgia Tech have developed a cooling module based on piezoelectric generation of droplets, where secondary droplets are formed from a primary droplet and then impinged on the hot surface where it is immediately vaporized [6]. While some of these techniques have been shown to dissipate heat more effectively than conventional fan-based techniques, many of these systems require external actuators or high-voltage regulators, thereby making IC-level integration difficult. More importantly, nearly all of these systems are based on architectures that are inherently unable to address the cooling of hot-spots.

In this thesis, we propose a droplet-based cooling system for ICs that can adaptively perform thermal management to dynamically cool hot-spots through real-time reprogrammable flow. Using a platform developed at Duke University called digital microfluidics [13], cooling droplets can be independently moved in user-defined patterns over a 2-D planar array of discrete electrodes. Since these patterns can be redefined on-the-fly, hot-spots can be detected and subsequently cooled at an accelerated rate, maintaining uniformity in the thermal profile of an IC. Furthermore, due to its low power consumption and simple architectural requirements, this digital microfluidic adaptive hot-spot cooling technique can

be integrated into standard IC design and fabrication processes with minimal difficulty.

In the remainder of the chapter, we categorize and review existing techniques for chip cooling, focusing primarily on techniques that use microfluidics for active cooling. In Chapter 2, adaptive hot-spot cooling principles and design are discussed, with focus on the digital microfluidic platform as an enabling technology. The design, fabrication, and operation of basic digital microfluidic devices are described. Two implementations of digital microfluidic adaptive cooling are then presented: a flow-through approach using cooling liquids and a thermal switch approach using liquid metals. The design and implementation of temperature feedback mechanisms are also discussed. Chapter 3 explores the technological developments of the digital microfluidic platform in order to address IC cooling. The thermal effects of droplet transport are studied in Chapter 4, where it is shown that the transport of a droplet immersed in oil is facilitated at elevated temperatures. In Chapter 5, the effectiveness of heat transfer between nano- to micro-liter sized droplets and hot-spots in a flow-through based system is characterized, however, due to current limitations in droplet transport speeds, the flow rates necessary to cool hot-spots was not achievable. Thus, in Chapter 6, we explore the possibility of employing liquid metal droplets to create a reconfigurable thermal conductance layer which can address non-uniform heat-flux densities. Using mercury, several parameters are investigated for their effects on the heat-transfer in this system. In Chapter 7, we discuss future directions for both the flow-through based and thermal switch-based methods of cooling, with aims toward a manufacturable and easily integrable adaptive hot-spot cooling system.

1.2 Newton's Law of Cooling

The study of heat-transfer in microfluidic systems begins with an understanding of heat convection between a solid and a moving liquid. Given a solid surface at temperature T_b and an adjacent moving liquid at a temperature T_f, where $T_b > T_f$, the rate of energy

3

transfer from the surface of the solid to the liquid is quantified by the following empirical expression

$$\frac{dQ_c}{dt} = hA(T_b - T_f),$$ (1.1)

known as Newton's law of cooling. In Equation (1.1), A is the surface area and h is a proportionality factor called the heat transfer coefficient. It is important to understand that the heat transfer coefficient is an empirical parameter that incorporates into the heat transfer relationship the nature of the flow pattern near the surface, the fluid properties, and geometry. For example, in forced convection, such as the case of fans blowing across an IC chip, the value of the heat transfer coefficient is much higher since new flow patterns are introduced to the otherwise slow buoyancy-induced motion of the air in free convection.

Throughout this study, the heat transfer coefficient serves as a measure of cooling efficiency. Hence, emphasis is placed on maximizing the heat transfer coefficient for the droplet-solid interface in our digital microfluidic system.

1.3 Categorization of IC Cooling Techniques

1.3.1 Passive vs. Active Cooling

Cooling methods can be broadly classified as being either passive or active. Passive cooling includes thermal conduction (e.g., pastes, metal lines, and vias), natural convection (e.g., finned heat sinks and ventilation slots), and radiation (e.g., coatings and paints). Heat pipes and thermosyphons also fall in the category of passive methods, but they offer higher performance.

Active cooling requires input power, and includes external methods such as forced convection (e.g., fans and nozzles), pumped loops (e.g., heat exchangers and cold plates), and refrigerators (e.g., Peltier/thermoelectric and vapor-compression-based).

4

1.3.2 Adaptive vs. Non-adaptive Cooling

We extend the concept of active cooling by adding the notion of "adaptability" to IC cooling. An adaptive cooling system incorporates closed-loop feedback of the temperature of the chip (either by direct or indirect measurement) to create a temperature-aware adaptive cooling system that can dynamically cool hot-spots.

A non-adaptive cooling system lacks such a feedback mechanism, and thus cannot respond to spatially non-uniform thermal profiles or hot-spots.

1.4 Current Methods for IC Cooling

1.4.1 Fan-based Cooling

The most widespread technique for cooling chips today is based on the use of air-based methods. A metal finned heatsink is typically mounted to a chip, on top of which a fan circulates air through the fins, thus dissipating the heat. Air is directly available in many cases and does not require complex, expensive packaging. Figure 1.1 presents an example of a modern CPU cooling heatsink and fan. While small improvements in heat-sink design and chip interface have been over the past several years, this technology has remained basically unchanged over many years.

1.4.2 Macrofluidic-based Cooling

Liquid cooling methods at the macro scale ($> \mu l$ scales) can be classified as direct and indirect cooling. Direct cooling methods involve the immersion of electronic chips in a pool of inert dielectric liquid. Indirect liquid cooling methods are usually based on two-phase flow. Examples of the latter include thermosyphons and heat pipes. In thermosyphons, a liquid evaporates with applied heat and condenses dissipating that heat elsewhere, in a closed system. The condensed liquid is typically returned to the hot area through gravity. A heat
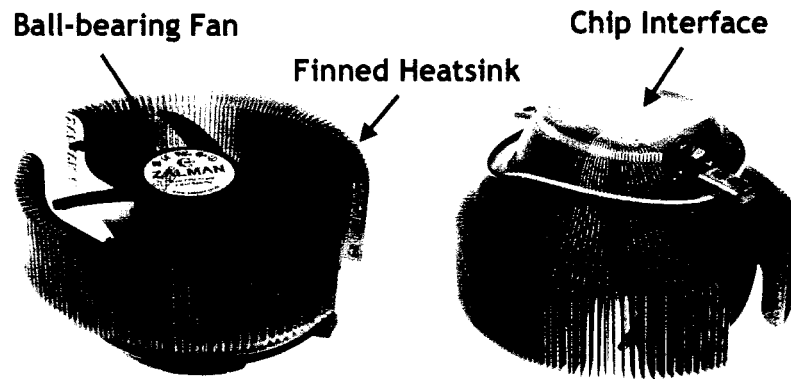
Figure 1.1: Front and back views of a Zalman CNPS7000B-ALCU CPU heatsink and fan. The fan operates anywhere from 1350-2600 rpm, depending on the die temperature obtained from a nearby thermistor. Image courtesy of Zalman, Inc.

pipe is a sealed and evacuated vacuum-tight container partially filled with a fluid. When heat is applied locally, the fluid in that part of the pipe is vaporized and it travels to the low pressure areas and condenses. This condensate reaches the hot area through the wick structures that line the heat pipes, thus ensuring uniform distribution of heat. Heat pipes are passive cooling devices and are used in many of today's notebook and quiet desktop computers, such as that used by Apple's PowerMac G5 (see Figure 1.2).

Microchannel heat sinks were first proposed by Pease and others at Stanford. Microchannel heat sinks are minute flow channels fabricated on the back of a thin silicon chip substrate with hydraulic diameters ranging from 10 μm to 30 μm. These heat sinks are characterized by extremely high surface area per unit volume of working fluid and low thermal resistance. However, microchannel heat sinks requiring an external, pressurized supply of cooling liquid have not been economically or practically feasible. An external, pressure source for liquid supply is inherently unsuitable for compact, embedded systems. Thus, there remains a technology void and a pressing need for cooling of ICs in compact packages. MEMS (microelectromechanical systems) and microfluidic pumping technology offer promising solutions for cooling chips.
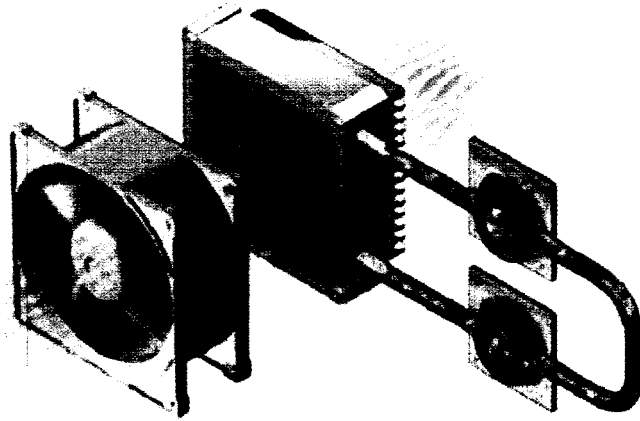
Figure 1.2: Cooling using heat pipes: A continuous flow of thermally conductive fluid that transfers heat from processors. The heated fluid then flows through a radiant grille, where air passing over cooling fins returns the fluid to its original temperature. Image courtesy of Apple Computer, Inc.

1.4.3 MEMS-based Cooling

Air is usually preferred over liquids for cost-effective implementation and simple assembly. MEMS-based air cooling methods that were proposed include arrays of microfabricated membranes actuated electromagnetically to produce air microjets [1], and air impinging-jet heat exchangers [2], as shown in Figure 1.3.

A bulk micromachined microfin array heat sink was fabricated, which enhances hydrodynamic mixing. As shown in Figure 1.4, the array consists of warped bimorph microcantilevers that undergo vibration when an air jet is impinged on them, creating vortices and dissipating heat faster compared to a plain-wall heat sink [3].

7
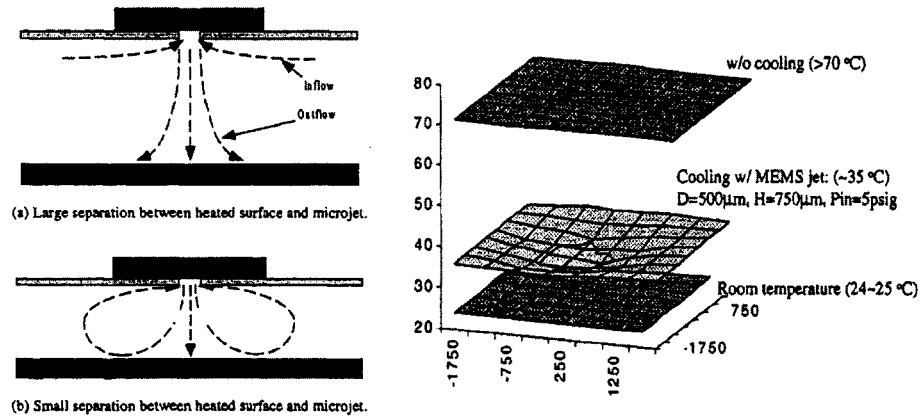
Figure 1.3: Air circulation patterns of a MEMS-based microjet cooling system (left) [1]. Temperature profiles showing the effectiveness of impinging jet cooling with a single nozzle [2].
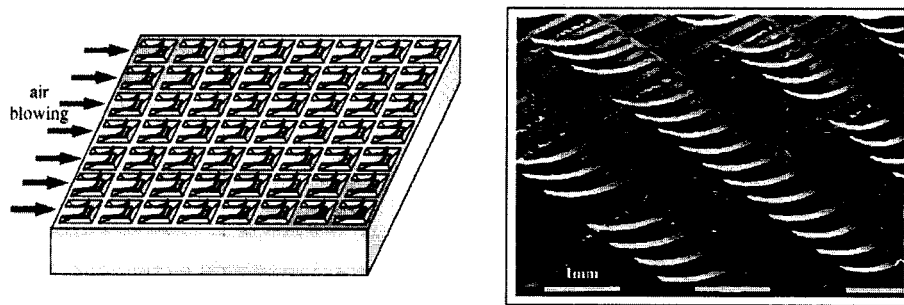
Figure 1.4: Schematic view of a microfin array heat sink (left). SEM photograph of the fabricated microfin array with initial deflection. [3]

1.4.4 Microfluidics-based Cooling

As power and heat flux continues to rise and microfluidic pumping technology matures, liquid cooling, which was successfully introduced in mainframe computers and supercomputers in the early 1980s, is receiving renewed attention. Micro- and mini-channel devices have been made to miniaturize the cooling hardware. Micro-channel cooling loops have high cooling performance, large heat transfer coefficients, small channel volumes, and small cooling inventory. They can be mass manufactured using traditional IC microfabrication techniques. However, large pressure gradients are required to force liquids through the micro-channels due to increased surface areas. For fully developed laminar flow (which is typical in such microchannels) and constant heat flux, chip temperatures increase linearly from the inlet to the outlet.

Two conventional strategies based on Newton's law of cooling can be employed to improve the forced-convection heat transfer rate with a specified temperature difference. One is to increase the surface area of the heat sink and the other is to increase the heat transfer coefficient. The surface area can be increased with microchannels and the heat transfer coefficient can be increased using microfluidic pumping solutions.

A pumpless loop has been presented with micro-channel surfaces for cooling [4]. It relies on fluid density differences between two vertical, parallel tubes to induce fluid motion, as shown in Figure 1.5. The top ends of both tubes are connected to a reservoir. When one of the tubes is heated, the liquid vaporizes and the bubbles rise up through the reservoir liquid into an air-cooled condenser. The condensed liquid drips down back into the reservoir. Due to the difference in density between the liquids in the hot tube and the cold tube, a non-equilibrium hydrostatic pressure is developed, which in turn induces a flow. This method does not require any external pumps and as the temperature increases, the flow becomes faster. It is a passive way of cooling without any external power requirements. However, this technology cannot be used in applications where specific cooling of

9

hot spots is necessary.
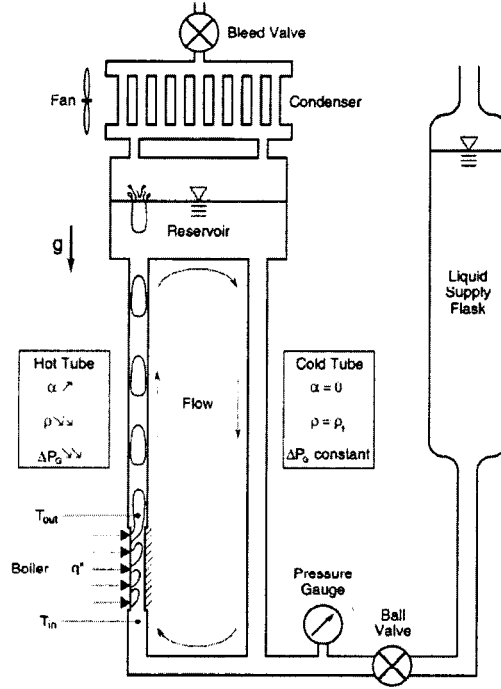
Figure 1.5: Pumpless loop cooling concept and experimental setup [4].

Recently, much attention has been focused on developing reliable micropumps that are capable of pumping liquids through microchannels. Experiments have been performed in rectangular, triangular, and diamond-shaped microchannels in both the single-phase and two-phase regimes with water as the cooling liquid. Very high pressure drops are required to achieve low thermal resistance. In order to increase the heat flux from a microchannel with single phase cooling, it is necessary to increase the heat transfer coefficient by either increasing the liquid flow rate or decreasing the hydraulic diameter. In two phase regimes, the evolution of the phase change from liquid to vapor in microsystems is different from that in macro-systems. A closed-loop two-phase microchannel cooling system based on electroosmotic pumping of liquids was developed at Stanford [5], as shown in Figure 1.6.

The electroosmotic pump is connected to a microchannel heat exchanger which in turn

10

Planar view (dimensions in millimeters)

manifold
inlet/outlet
microchannel
Si substrate

Cross-sectional view

microchannel — glass
— silicon
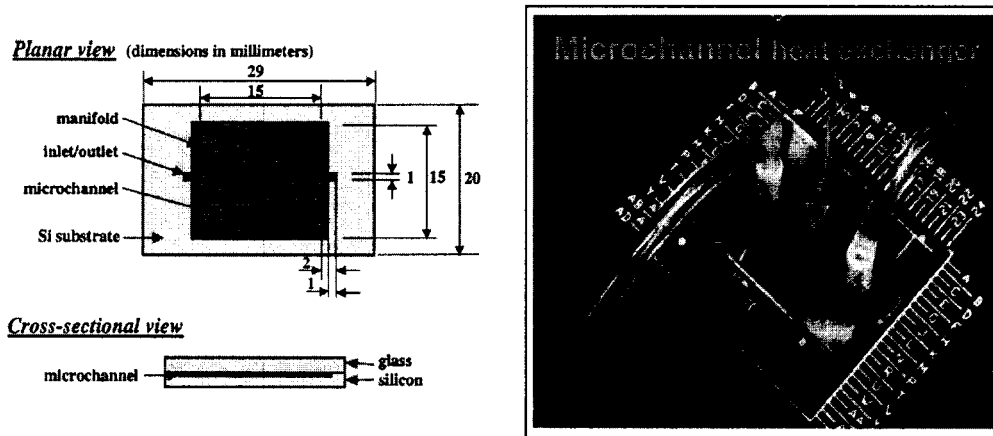
Figure 1.6: Schematic (left) and photograph (right) of a microchannel heat exchanger as proposed by Jiang et al. [5]

is connected to a heat rejecter. This pump was observed to remove 38W with a pump power of 2W. This is the first demonstration of a hermetically-sealed electroosmotic cooling system.

A MEMS-based micro capillary pumped loop (micro-CPL) has been fabricated on a silicon wafer where an evaporator, condenser, reservoir, and liquid lines are all integrated [14]. Micro-CPLs offer greater geometric freedom over heat pipes and can also carry greater heat loads due to the simultaneous flow of vapor and liquid, in contrast to counter-current flows in conventional heat pipes.

A cooling module based on piezoelectric generation of droplets has been developed by researchers at Georgia Tech [6], as shown in Figure 1.7. In this structure, secondary droplets are formed from a primary drop and then impinged on the hot surface. Unlike a heat pipe, there is no need to have wick structures to continuously supply the liquid to the hot area of the chip. The droplets upon impinging the hot surface evaporate and do not form an insulating vapor blanket as found in pool boiling situations. The momentum of the atomized droplets is sufficient to propel the droplets to penetrate through the vapor layer and spread into a thin film on the hot surface.

11
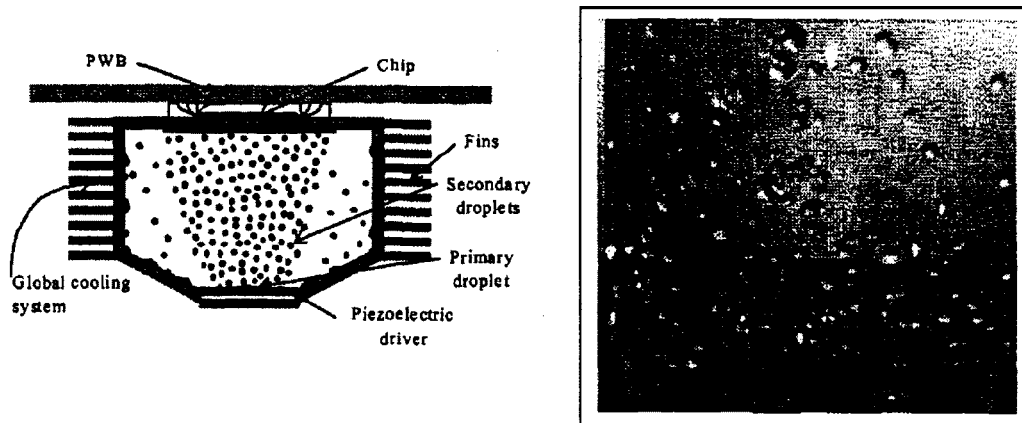
Figure 1.7: Schematic of a vibration-induced droplet atomization cooling device (left). Photograph of ejected secondary droplets from the device (right) [6].

1.5 Chapter Summary and Conclusions

In this chapter, we categorize and review current techniques used to address the thermal management of ICs, the most promising of which have been microfluidics approaches. While the cooling ability in these devices have been shown to perform better than the fan-based approaches used today, many are unable to address the changing thermal profiles in the IC due to inherent limitations in their design. In the following chapter, we look toward an alternative microfluidic platform in which an array of cooling droplets are independently moved such that the motion of each droplet can be reconfigured on-the-fly. This inherent flexibility in droplet flow allows for a dynamic response to changes in the thermal profile of the IC, thus resulting in an adaptive cooling platform.

12

Chapter 2

Adaptive Hot-Spot Cooling Principles and Design

The techniques reviewed in Chapter 1 are not adequate for the dynamic on-the-fly cooling of hot spots; many of those techniques are package-level solutions where high thermal conductivity standoffs are interfaced between the microprocessor chips and the lid of the package. Any thermal variations within the IC must be addressed in advance by permanently fixing higher cooling densities near the regions of highest heat flux. While the cooling efficiency of these devices has been shown to be higher than traditional fan-based methods, their inherently inflexible architectures cannot be reconfigured for adaptive cooling. In this chapter, we propose an alternative solution by first describing the requirements to achieve a reconfigurable IC-level cooling solution. We then explore a droplet-based microfluidic technology called "digital microfluidics" as an enabling platform and present two implementations of digital microfluidic adaptive cooling: the flow-through of cooling liquids and the switching of liquid-metals. In addition, we present a number of feedback mechanisms necessary for our proposed systems to be truly adaptive.

2.1   Requirements for Adaptive Hot-Spot Cooling

An ideal thermal management solution should satisfy the following requirements at the architectural level:

1. The system should have a mechanism to transfer and remove heat efficiently.

2. The system should be closed-loop.

3. The system should be able to detect the changing thermal profile of the IC.

13

4. The system should be able to adapt itself in response to a changing thermal profile.

At the implementation level:

1. The system should have an easily integrable control mechanism.

2. The system should be self-regulating.

3. The system should easily interface with the integrated circuit.

4. In the event that the primary cooling method fails, the system should revert to a backup cooling mechanism.

While current state-of-the-art technologies have been able to address one or two requirements from each list, most are unable to address them all. For example, all continuous-flow microfluidic based solutions presented to date are unable to address spatially varying thermal profiles in ICs due to the restrictions arising from permanently-etched channels. Furthermore, integration at the IC level has proven to be difficult due to bulky external pumps.

We take an alternative approach by presenting a droplet-based electrowetting-driven microfluidic system, whereby a large number of discrete droplets can be independently programmed and re-programmed to address the changing thermal profiles in an IC. As we will discuss in the remainder of this chapter, this "digital microfluidic" platform is amenable to both hot-spot cooling and IC-level integration, and able to satisfy all the requirements for successful adaptive hot-spot cooling.

2.2 Digital Microfluidics as a Cooling Platform

A micro-pump utilizing the phenomenon of electrowetting has been developed at Duke University in which discrete droplets can be formed and manipulated electrostatically

[13, 15]. The division of liquids into independently-controlled packets of liquid for manipulation provides several important advantages over continuous-flow or mist-based systems. First, microfluidic operations can be reduced to a set of basic discrete operations (i.e., move one unit of liquid one unit step), which allows for a hierarchical and cell-based design approach to be used. We refer to this approach as "digital microfluidics", as it is analogous to the design techniques in digital microelectronics. Second, the absence of permanently etched structures allows for a completely reconfigurable system. The only active component, an actuating electrode, is embedded within a planar surface of the device, requiring no additional components or structures such as pumps and valves. Third, given a two dimensional array of actuating electrodes, liquid droplets can be manipulated laterally in any arbitrary path without the need for external pumps and valves. The absence of permanently-fixed structures found in continuous-flow devices allows for this digital microfluidic system to be completely virtual and reconfigurable. Fourth, liquid flow has been shown to inherently increase with increasing temperature. Thus, local hot-spots on a chip could potentially have an inherently increased cooling rate without the need for external sensors.

We begin our discussion of our digital microfluidic-based hot-spot cooling concept with the principles of actuating droplets using electrowetting. Since droplets in chip cooling applications are subject to a wide range of temperatures, we start by studying the contact lines of the droplets during motion, as they can be affected by thermal imbalances within the droplet. We continue with discussing the steps necessary to build and operate a digital microfluidic device. We then propose two implementations of this platform for adaptive hot-spot cooling: a flow-through based architecture and a switch-based architecture.

2.2.1 Electrowetting-based Actuation of Droplets

The motion of droplets by the use of electrowetting is based on the principle of differences between contact angles in the advancing and receding lines of a droplet. When a droplet rests on a non-wetting solid surface, the forces acting at the solid-liquid-vapor interface equilibrate and result in a contact angle θ between the droplet and solid, as described by *Young's equation*,

$$\gamma_{LV} cos(\theta) = \gamma_{SV} - \gamma_{SL},\tag{2.1}$$

where γ_{LV}, γ_{SV} and γ_{SL} are the liquid-vapor, solid-vapor and solid-liquid surface energies.
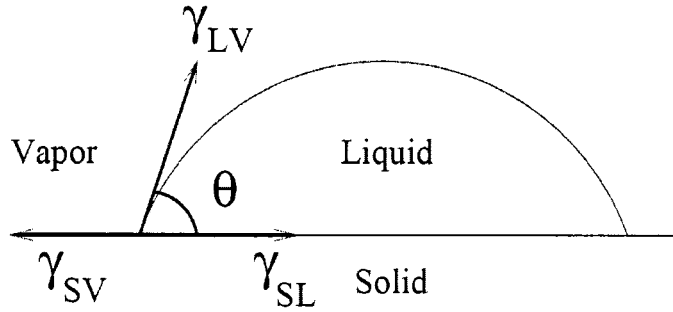
Figure 2.1: Cross-section of equilibrium forces acting on one side of a non-wetting droplet in contact with a horizontal solid surface.

When an imbalance in these surface energies occurs, as in the case of a droplet resting on a surface with a gradient surface energy, a net force is induced which may initiate droplet motion. This imbalance can be induced by chemical, thermal, or electrostatic means. In the case of thermally induced droplet motion, a surface tension gradient can be induced by differentially heating the ends of a droplet, since the surface tension of a liquid decreases with temperature. A number of droplet-based microfluidic systems have been developed based on this method [16][17][18].

In electrowetting-based actuation of droplets, electrical fields are used to induced surface tension gradients. This method takes advantage of the electrowetting effect, in which
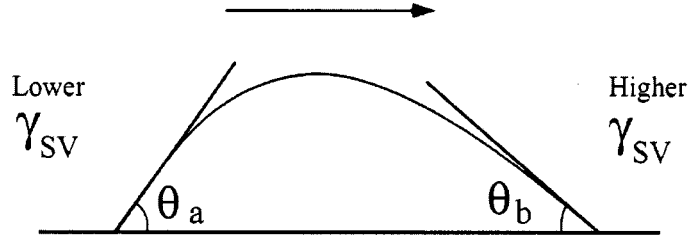
Figure 2.2: Cross section of a droplet resting on a surface having a surface energy gradient. The arrow indicates the direction of motion.

the surface energy can be directly modified by the application of an electric field. Consider a droplet resting on a electrode separated by a hydrophobic insulator. The droplet consists of a conductive and/or polarizable liquid. A potential is applied between the droplet and the electrode, resulting in a capacitive energy E stored in the insulator. The resulting energy is

$$E = \frac{\epsilon_0 \epsilon_r A}{2d} V^2,$$ (2.2)

which causes the solid-liquid interfacial tension to change such that

$$\gamma_{SL}(V) = \gamma_{SL}(0) - \frac{\epsilon_0 \epsilon_r A}{2d} V^2.$$ (2.3)

The resulting contact angle change can thus be calculated from Equation 2.2 such that

$$cos\theta(V) = cos\theta(0) + \frac{\epsilon_0 \epsilon_r A}{2d\gamma_{LV}} V^2.$$ (2.4)

Equation 2.4 thus states that application to the electrode results in the contact angle to decrease, causing the droplet to spread or effectively wet the surface. If we divide the bottom electrode into discrete electrodes, we can induce motion in the droplet to any adjacent electrode simply by applying voltages to that electrode. This method for droplet transport will be explained later in this chapter.

17
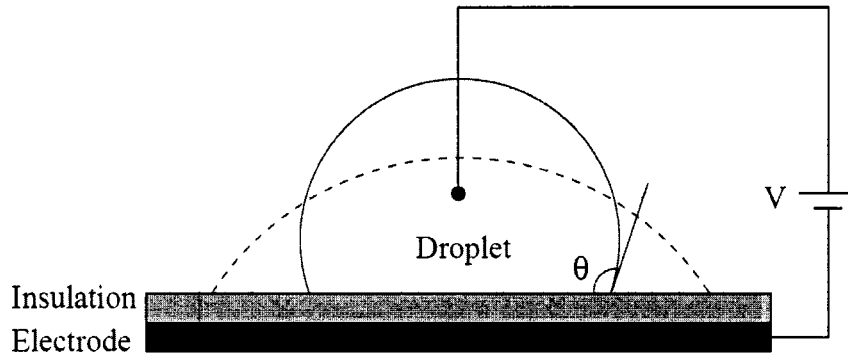
Figure 2.3: The electrowetting effect.

While droplet actuation by thermocapillary and electrostatic methods has been rigorously studied as independent methods, the presence of both mechanisms in the same system has not yet been explored. The transport of droplets through a thermal gradient by electrowetting could potentially be hindered as the surface energies of the droplet are dependent on two variables - differential temperature and voltage. We must therefore be wary of both effects when studying the effectiveness of droplets to cool thermally non-uniform substrates, particularly at localized hot-spots.

2.2.2 Fabrication of Digital Microfluidic Devices

Digital microfluidic devices are typically fabricated using standard micro-fabrication techniques, ranging from a single-mask, single metal layer design to a multi-layer design. They have traditionally been fabricated on glass substrates, but can also be fabricated using alternative processes such as printed circuit board techniques as we will discuss in Chapter 3.

Metal layers, vias, patterned insulators, and gaskets are designed using a CAD tool (e.g., Mentor Graphics IC or TurboCAD). Masks made of mylar or glass are then tooled from these designs. For a glass-based process, photoresist is patterned using the masks on chrome-plated glass plates, and wet-etched to realize the chrome pattern on glass. The process is repeated if multiple metal layers are required, separating each layer with an insu-

lator (typically polyimide). The design of a simple linear-array of interdigitated electrodes is shown in Figure 2.4.
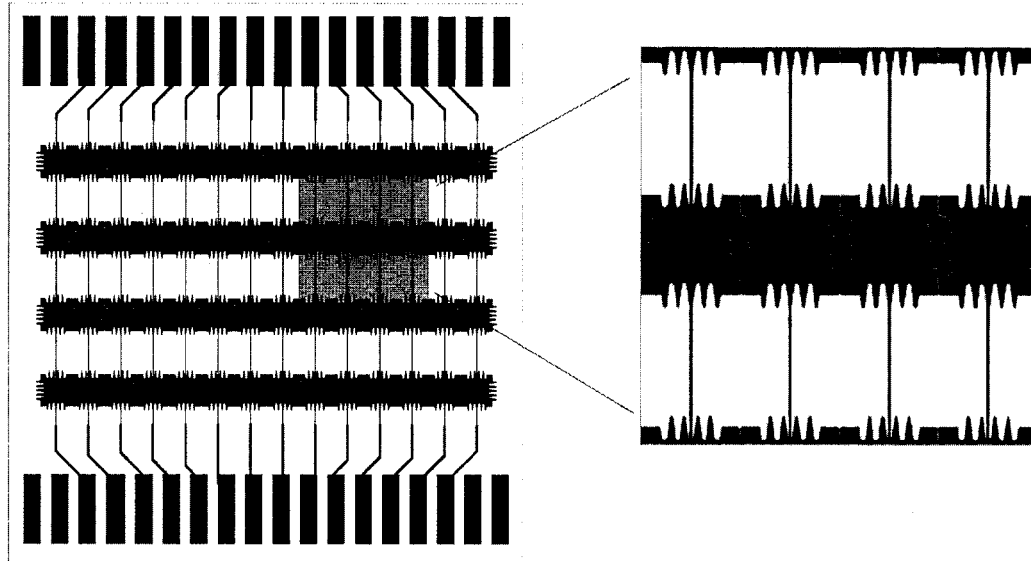
Figure 2.4: The design of a simple linear-array of 1.5 mm pitch interdigitated electrodes generated using CAD tools from Mentor Graphics.

After the chrome layer is patterned, an insulation layer of Parylene C (800 nm) is then deposited using wafer-tape to mask the contacts. Both the patterned bottom plate and conductive top plate (i.e. ITO-coated glass) are then spin-coated with Teflon AF 1600 (50 nm) to create a thin hydrophobic layer.

A glass spacer can used to separate the top and bottom plates, yielding a fixed gap. Alternatively, a patternable gasket can be added on the bottom plate before the hydrophobization step. For chips that require on-chip dispensing, the gasket layer is used to define the reservoirs, and it provides the proper geometry for on-chip dispensing.

The height of the gap, given a certain electrode pitch size, has been shown to have a significant influence on the behavior of droplet motion and functions. This geometry can be quantified into a dimensionless number known as the aspect ratio. The aspect ratio is defined as the ratio of the gap height to the electrode pitch size. A schematic of the final

assembled glass-based chip is shown in Figure 2.5.
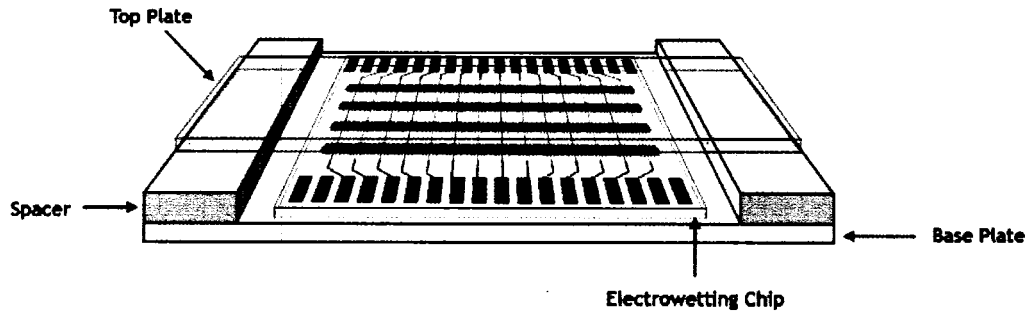
Figure 2.5: Schematic of the assembled digital microfluidic electrowetting chip using the design shown in Figure 2.4.

2.2.3 Digital Microfluidic Operations

Droplet Transport

Microdroplets in a digital microfluidic-based platform are actuated by the electrowetting phenomenon as demonstrated by Pollack *et al* [15]. Since electrical fields can be easily modulated and precisely localized through the use of photolithographically-defined electrodes, electrowetting can provide a very high level of control across the surface of a substrate. As shown in Figure 2.6, a droplet of polarizable and/or conductive liquid is sandwiched between the bottom plate of electrodes and a top plate. A constant ground potential is applied to the droplet, either through the top plate or through coplanar ground lines on the bottom plate. The electrodes on the bottom plate are buried underneath an insulator layer as to prevent current from flowing through the droplet. The surfaces of both the top and bottom plates are coated with a hydrophobic material. Finally, an oil-based filler fluid, while not necessary, is typically used in order to surround the droplet. The presence of the filler fluid facilitates droplet motion and prevents evaporation of the droplet liquid.

The actuation mechanism is the result of oil-water interfacial tension gradients induced in a droplet when a potential is applied to the underlying electrodes. Consider the system

20
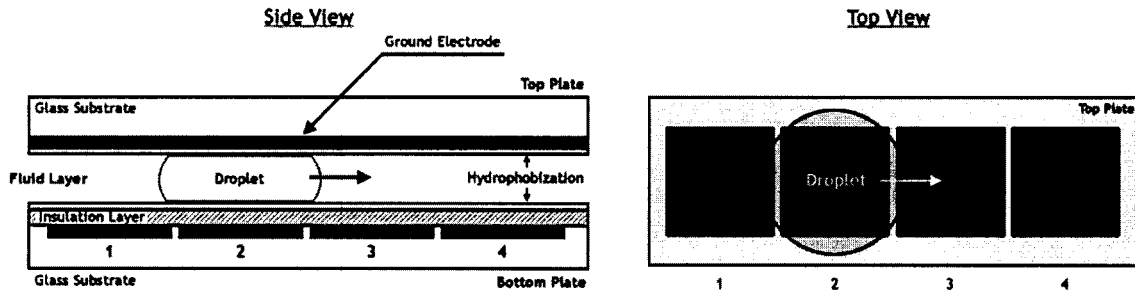
Figure 2.6: Schematic side and top views of the electrowetting chip.

shown in Figure 2.7 as shown from the top, where a droplet rests upon an array of four electrodes, e_1 through e_2.

When a voltage is applied to electrode e_2 beneath the droplet, the droplet is charged and an increased surface energy causes the droplet to change its interfacial tension with the surrounding oil (if present), consequently wetting the surface of the electrode. When the voltage is turned off under the current electrode and applied to an adjacent electrode, e_3, an interfacial tension gradient is created, causing the droplet to move until the interfacial tension equilibrates when the droplet moves completely onto the activated electrode. This method of droplet actuation is the basis for all microfluidic operations.
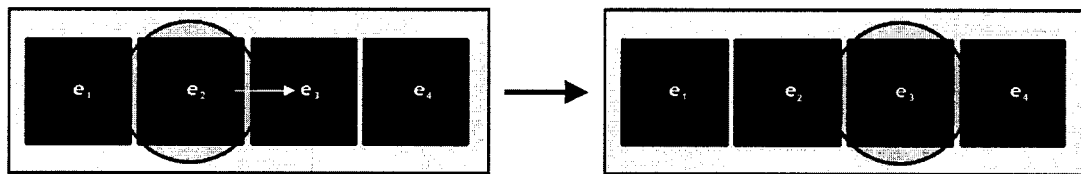
Figure 2.7: Basic droplet transfer with a sufficiently-sized droplet.

The volume of the droplet is chosen such that it is slightly larger than the pitch of the electrodes, ensuring overlap between the electrode on which the droplet currently resides and its adjacent electrode. This overlap is necessary in order for droplet motion to be successful. A variety of electrode shapes and sizes can be utilized, as long as the overlap

21

requirements are met.

Droplet Formation/Dispensing

Droplets can be dispensed either by the use of external pressure from an off-chip reservoir or from an on-chip reservoir using only electrowetting forces. In the case of using external pressure [15, 19], droplets are formed by injecting liquid into the chip through a hole in the top plate. An electrode is then activated, and the liquid is pulled backed, producing a droplet in the process.
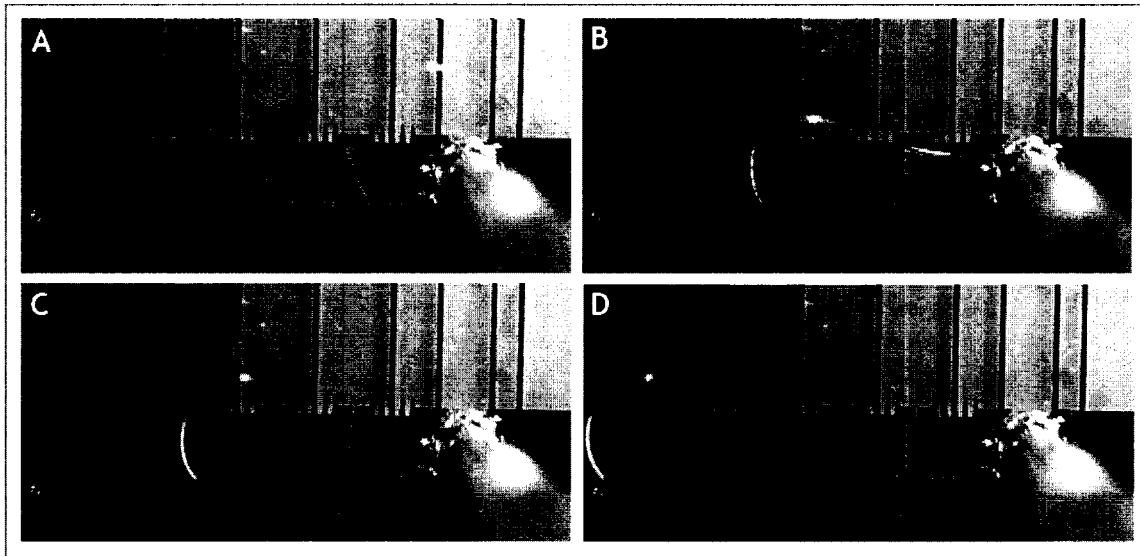
Figure 2.8: Time-lapsed sequence of droplet dispensing using an external pressure source. Interdigitated electrodes are spaced 1mm apart.

On-chip dispensing is accomplished by first extending a liquid column from an on-chip reservoir by activating a series of electrodes [20, 21], as shown in Figure 2.9. Liquid is delivered via a micro-pipettor to the reservoir through a small loading channel connected to a loading port. The electrodes other than those where the droplet is to be formed are then deactivated. The electrode in the reservoir is then activated to retract the liquid, pinching off a droplet in the process. The accuracy and repeatability of this volume depends on

22
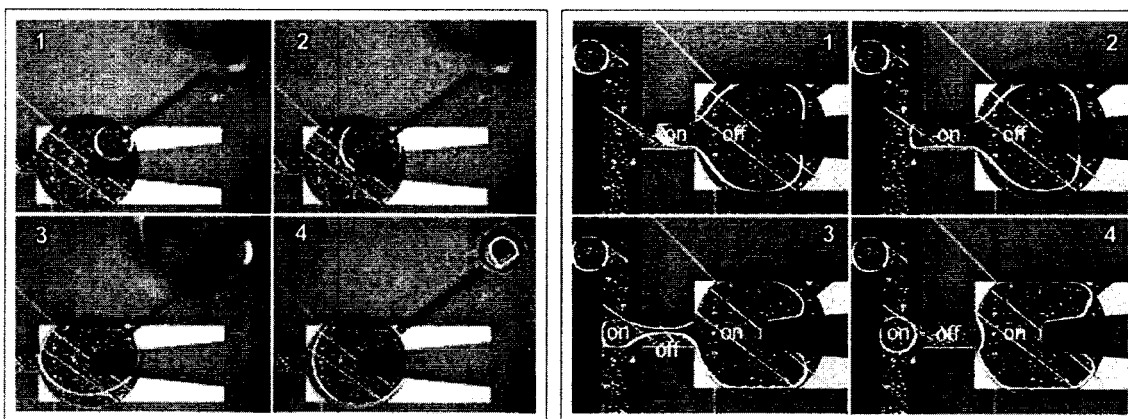
Figure 2.9: Time-lapsed sequence of loading of liquid (left) and on-chip dispensing of droplets (right) as viewed from the top. Electrodes are spaced $500\mu m$ apart.

several factors, including aspect ratio (L/H), droplet/oil interfacial tension, liquid volume in the reservoir, number of pinch-off electrodes, actuation voltage and control sequence. All these factors contribute to the variations of droplet volume. From data obtained in two different droplet generation experiments, the calculated variation of the volume is less than 3%. To minimize this variation, a capacitive feedback method can be developed to allows for dynamic control of the droplet volume by calculating the droplet footprint on the electrode based on capacitance measurements on the respective electrodes. This capacitive feedback system will be discussed in greater detail in Chapter 3.

Recycling of Liquids

Droplets that are no longer needed can either be removed to a "waste" reservoir or recycled back into a droplet-dispensing reservoir. While waste reservoirs have been previous designed and used in biological and biochemical applications [20], the concept of recycling has not yet been introduced. In the case of a closed-loop microfluidic device, the recycling of liquids is a requirement, preferably on-chip. Figure 2.10 illustrates how droplet recycling can be performed, and will be discussed in greater detail in Chapter 3.

23

Droplets Dispensed: 1
Droplets Received: 1
Net Volume Change: 0

Droplets Dispensed: 1
Droplets Received: 1
Net Volume Change: 0
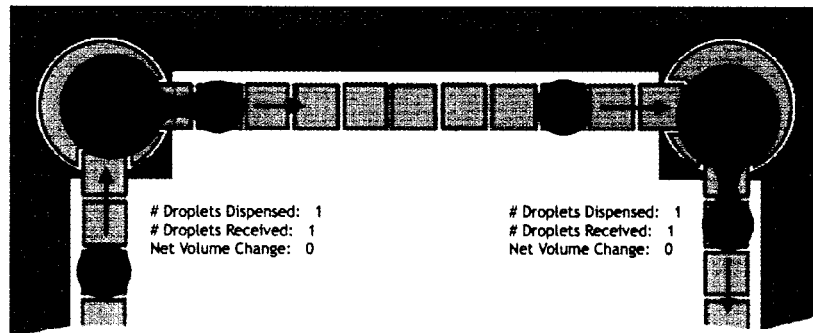
Figure 2.10: Droplet recycling is performed by returning dispensed droplets back into a reservoir, as shown in this simple closed-loop design.

2.2.4   Digital Microfluidic Adaptive Cooling - Flow-through Method

While digital microfluidic devices have been traditionally used to develop biological and chemical labs-on-a-chip, the same architecture and droplet-based operations can be directly implemented for IC cooling applications in a number of ways. One method is to continually dispense and transport cooled droplets across the surface of an IC, whereby the droplets transfer, store, and carry heat away from the IC substrate to a cooling reservoir. Once the droplet has cooled, it can be re-dispensed to repeat the cooling process.

Figure 2.11 shows a schematic top and side views of a this flow-through cooling method. The system consists of reservoirs of liquid sandwiched between a bottom microfluidic chip and a top plate. The microfluidic chip consists of an array of electrodes connected to the reservoirs from which cooling droplets are formed. Once the droplets are formed, they are transported across the array. The top plate can either consist of a thermally conductive material on top of which rests the IC chip to be cooled, or can be the IC chip itself.

Since a large number of droplets can be transported in user-defined patterns over a two-dimensional array of electrodes, a variety of flow paths for optimal cooling can be
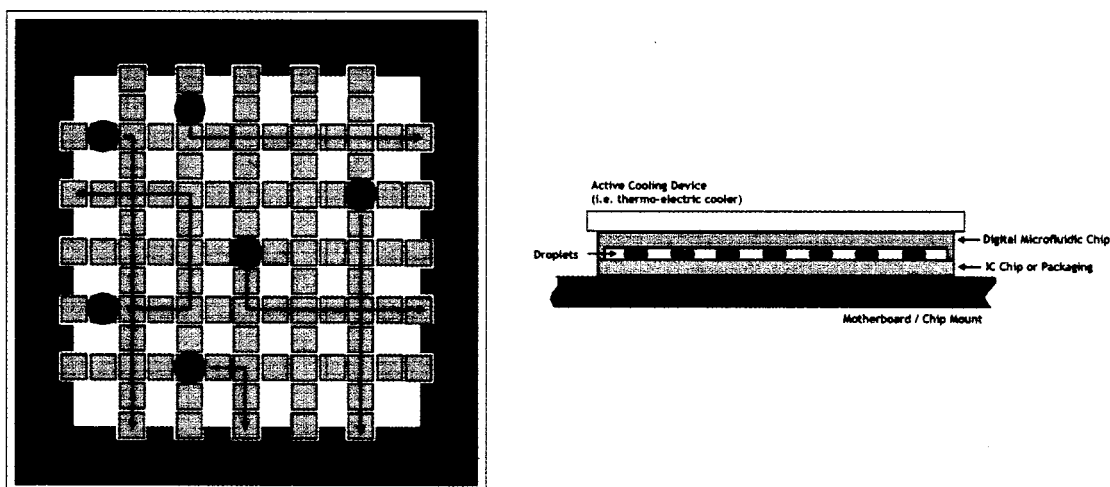
Figure 2.11: Top view (left figure) and side view (right figure) of a proposed cooling architecture using digital microfluidics. Droplets which are either in direct contact to an IC or via an intermediate thermal conductor are formed from reservoirs and transported in reconfigurable flow paths back to the reservoirs where they are recycled.

programmed, depending on the thermal profile of the IC. These thermal profiles can be either obtained in advance, or determined in real time via a thermal feedback mechanism. In both cases, the location of thermal hot-spots on the chip can be readily determined and the flow of droplets can be reconfigured for its optimal cooling, as shown with the simple case of a two-droplet system in Figure 2.12. Furthermore, the speed at which droplets are transported (i.e. their effective flow rates) can be varied, adding an extra degree of controllability. This on-the-fly reconfigurability inherent to digital microfluidics enables us to create an adaptive cooling platform.

To determine the efficiency of using droplets to cool a target substrate, let us consider a die with a total area of 1.5 X 1.5 cm^2 and dissipating a power of 200 W. If we assume we have 10 square electrodes per array with a pitch of 1.5 mm and a total of 10 such arrays, the power dissipation per a single electrode can be calculated as 2W. Considering that this power is dissipated into the droplet with a temperature rise to about 45°C, we can use the specific heat equation to calculate the volume flow rate required to transport this heat away

25
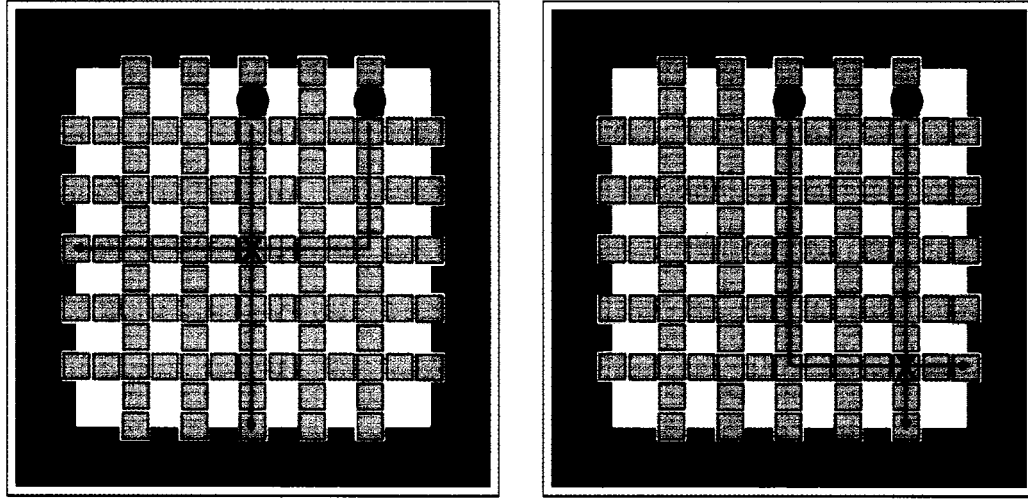
Figure 2.12: The flow of two droplets over an array of electrodes with different thermal profiles, where the red 'x' indicates a location of a hot-spot. The location of the hot-spot determines the path the droplets will take to maximally cool the hot-spot in order to create a uniform thermal profile. These hot-spots can be pre-determined (i.e. where and when an FPU is used is already known) or can be determined on-the-fly through an array of temperature sensors.)

by the droplets

$$\Delta Q = m \cdot c_p \cdot \Delta T, \tag{2.5}$$

where ΔQ is the heat applied to the droplet, m is the mass of the droplet, c_p is the specific heat of the droplet, and ΔT is the droplet's temperature rise. For water, $c_p = 4.186$ J/g·K, thus the required volume flow rate is about 10 μL/s. With an electrode pitch of 1.5 mm and droplet height of 600 μm, we have demonstrated volume flow rates of about 170 μL/sec which is about 17 times the required flow rate.

The presence of laminar flow will reduce the ability to transfer heat efficiently compared to turbulent flow. We have observed that flow reversibility, which is a result of laminar flow due to the low Reynolds number, is pronounced when the droplets are transported back and forth over a few electrodes. The flow reversibility reduces as the droplets are transported over distances of about 5 times the droplet's length or when transported with higher speeds [22], thereby increasing heat transfer.

26

2.2.5 Digital Microfluidic Adaptive Cooling - Programmable Thermal Switch Method

An alternative method to promote heat transfer across a thermally non-uniform substrate is the concept of a liquid-metal based thermal switch. This method, while it does not address the absolute cooling of a target substrate, allows for a simple programmable thermal conductance layer between the target substrate and an external cooling device, such as a heat-sink-fan.
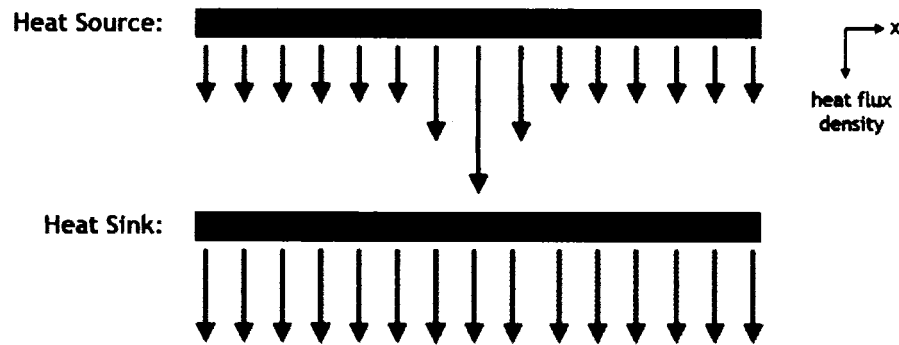
Figure 2.13: Diagram illustrating the one-dimensional heat flux from a non-uniform heat source and a uniform heat sink.

Consider the one-dimensional case of a target substrate that has a uniform background heat flux and a hot-spot which is significantly hotter, as shown in Figure 2.13. We assume we have a heat sink that has constant heat-flux, as is the case with most cooling systems (heat sinks, peltiers, etc.) today. If we were to directly attach the heat sink to the heat source, the resulting temperature profile of the target substrate would be non-uniform, as illustrated in Figure 2.14. Because the thermal resistance between the heat sink and the heat source is uniform, the hot-spot from the target substrate would cause non-uniformity in the substrate's temperature profile.

However, if we were to spatially vary the thermal resistance between the heat source and heat sink, then it is possible to obtain a uniform temperature in the target substrate, as

27
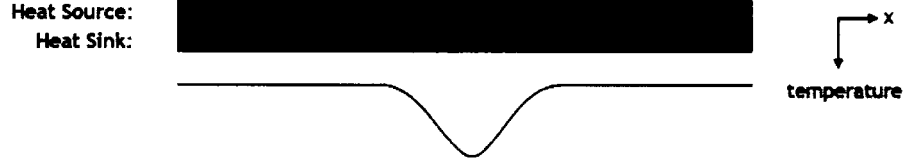
Figure 2.14: Diagram illustrating the resulting one-dimensional temperature profile of a non-uniform heat source coupled with a uniform heat sink.

illustrated in Figure 2.15.

Figure 2.15: Diagram illustrating the resulting one-dimensional temperature profile of a non-uniform heat source coupled with a uniform heat sink with an intermediate thermal conductivity layer. The highest thermal conductivity is in the center of the layer.

A simple one-dimensional conduction model can be constructed to illustrate this concept. We base this model on the general equation of heat conduction derived from *Fourier's law*,

$$\frac{\partial}{\partial x}(k\frac{\partial T}{\partial x}) + \frac{\partial}{\partial y}(k\frac{\partial T}{\partial y}) + \frac{\partial}{\partial z}(k\frac{\partial T}{\partial z}) + \dot{q} = \rho c\frac{\partial T}{\partial t} \tag{2.6}$$

where $\dot{q}$ is the volumetric energy addition (W/m^3), ρ is the density of the liquid-metal (kg/m^3), and c is the specific heat of the liquid metal (J/kg·K).

Consider a thermal conductance layer of thickness L that is to be inserted between the target substrate and the heat sink, as illustrated in Figure 2.15. We divide this layer into a $m \times n$ mesh where each element has a thermal conductivity $k_{m,n}$. The temperatures at the two faces of each element are fixed at $T_{m,n}^{top}$ and $T_{m,n}^{bottom}$, where $T^{top} > T^{bottom}$. For steady conditions with no internal heat generation, the appropriate form of the general heat

28

conduction equation, Eq. 2.6, is

$$\frac{d^2T}{dx^2} = 0 \tag{2.7}$$

with the boundary conditions as

$$T(y = 0) = T_{m,n}^{top}, T(y = L) = T_{m,n}^{bottom}. \tag{2.8}$$

Integration of Eq. 2.7 with the boundary conditions from Eq. 2.8 gives the linear temperature distribution

$$T(y) = T_{m,n}^{top} + (T_{m,n}^{bottom} - T_{m,n}^{top})\frac{y}{L} \tag{2.9}$$

and application of Fourier's law gives a heat transfer of

$$q = \frac{kA(T_{m,n}^{top} - T_{m,n}^{bottom})}{L} \tag{2.10}$$

where A is the wall area normal to the direction of heat transfer). From these equations, we can calculate the temperature profile of the $m \times n$ mesh given either uniform or non-uniform thermal conductivities and heat densities.

A 1 cm $\times$ 1 cm thermal conductance layer was modeled to have a thickness of 100μm and a mesh size of 100 ($m = 10, n = 10$). The top of the layer was such that it had a background heat flux density of 100 W/cm^3, with a hot-spot in the center of 600 W/cm^3, as shown in Figure 2.16a. The bottom of the layer had a boundary of 30°C.

Assuming each element in the mesh has a thermal conductivity of 8 W/m·K, the resulting temperature profile of the target substrate is non-uniform, as shown in Figure 2.16b. The resulting hot-spot has a maximum temperature of 163°C, with a background temperature of 50°C. Using Equation 2.10, we can calculate the required thermal conductivity of each element to maintain a uniform thermal profile. The result is shown in Figure 2.16c, where the thermal conductivity reaches as high as 53.3W/cm·K. The resulting thermal conductivity values results in a completely uniform temperature of 50°C.

29
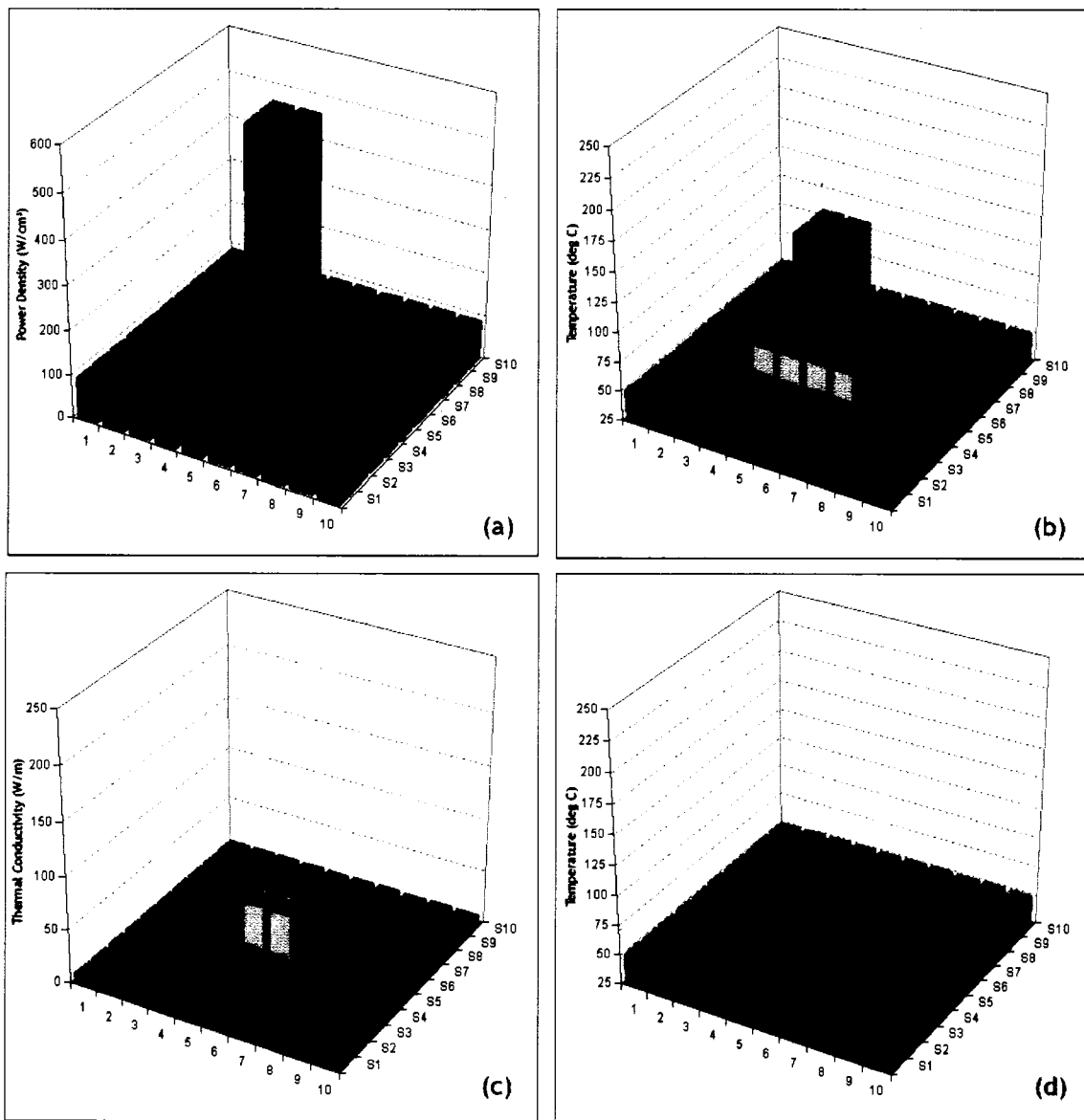
Figure 2.16: Heat conductance model of a theoretical thermal conductance layer used to serve as the interface between a target substrate and a heat sink. The heat flux density of each element is shown in (a), with the resulting temperature profile (b). From (b), the thermal conductance of each element can be calculated (c) such that the resulting temperature profile is completely uniform (d).

30

In the substrate of an actual microprocessor, the presence of hot-spots dynamically changes depending on the workload of the system. Thus, the thermal conductivity between the target substrate and the heat sink needs to also be dynamically changing. Consider a digital microfluidic chip that contains an array of cells which covers the entire area of a target IC chip we wish to cool, as illustrated in Figure 2.17. Each cell contains a single electrode, on top of which a droplet of liquid metal sits. Above the microfluidic chip is the IC substrate. Beneath each droplet is a metal via that travels to the backside of the microfluidic chip. The backside of the microfluidic chip can be attached to a traditional cooling method (i.e. heatsink/fan).
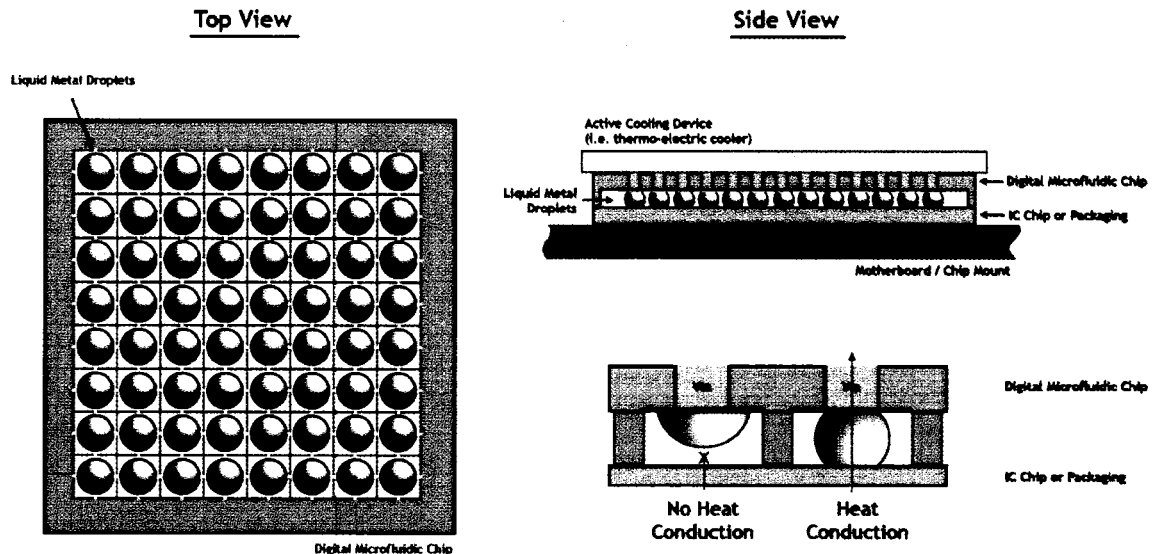
Figure 2.17: If an electrode or device fails in this case, the default position is "OFF" so maximum heat transfer will take place.

The liquid metal droplet acts a conduit between the IC substrate and the heat-sink. By default, all of the electrodes are actuated "ON". When this happens, the liquid metal droplet is detached from the top surface of the IC substrate. The thermal resistance between the IC substrate and the microfluidic chip is now that of the oil.

When a hot-spot is detected over a cell, the electrode within the cell is turned "OFF".

31

This causes the liquid metal droplet to relax and subsequently come into contact with the top plate. This reduces the thermal resistance between the hot-spot and the microfluidic chip / heat-sink by orders of magnitude, and heat is now able to be passed more efficiently from the hot-spot to the heat-sink. This behavior is demonstrated by Cell A and Cell B in the figure above.

An alternative method to the liquid metal switch is a "gradient switch," which allows each cell to specify how much contact into the metal vias to the heat-sink the liquid metal droplet is in contact (Figure 2.18). In this system, droplets move laterally, instead of simply "on/off" position. In the figure below, if there is no hot-spot, the droplet remains off of the metal vias (Cell A). If there is a maximally intense hot-spot, the droplet is positioned into the maximum number of vias (Cell B). A lower number of vias can be covered if there is a less intense hot-spot.
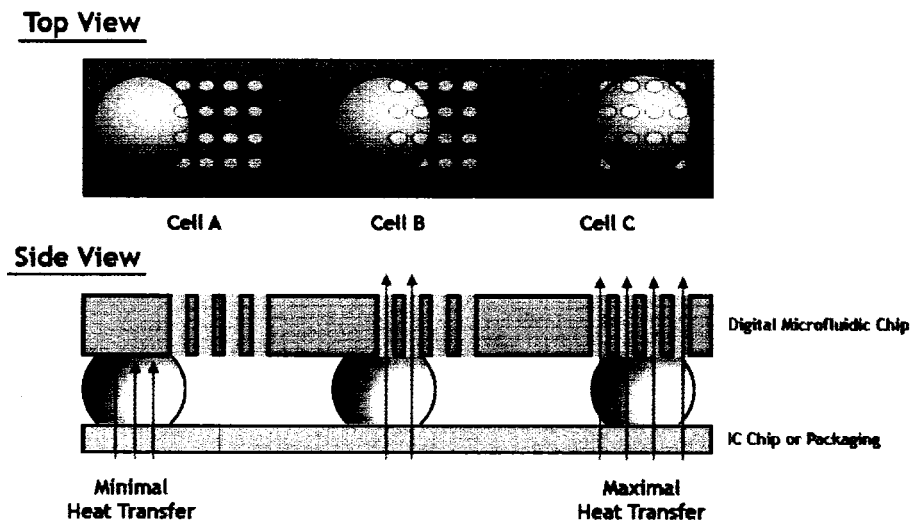
Figure 2.18: Figure illustrating a "gradient switch" which allows a single metal droplet to conduct a variable amount of heat depending on how many conductive vias it contacts.

This gradient switch approach allows for the finer control in creating a programmable thermal resistance layer between the IC chip and heat-sink.

2.3 Feedback Control Mechanisms

Feedback of an IC's thermal profile is crucial to the success of any adaptive cooling platform, as it provides a mechanism for which on-the-fly reconfigurability of droplet flow can work. There are three mechanisms for droplet flow control, each offering their own trade-offs in terms of flexibility, sensing, and computational overhead.

2.3.1 Thermal Sensor Feedback Control

Thermal sensor feedback control is a straightforward method where an array of temperature sensors maps the thermal profile of an IC for feedback to the droplet actuation system. For the flow-through based approach, droplet generation rates, flow paths and flow rates are dynamically adjusted based on the thermal profile on the chip. For the thermal switch-based approach, the number of liquid-metal droplets in contact with the target substrate would depend on these thermal sensor readings. This completely regulated approach offers the maximum flexibility as it dynamically adjust flow rates based on sensor readings, but it requires overhead for sensing, computation, and electronic control. For the programmable thermal switch-based approach, thermal sensors are the only method for feedback control.

2.3.2 Flow-Rate Feedback Control

It has been demonstrated that the flow of droplets is inherently increased at elevated temperatures [23]. This behavior is studied in greater detail in Chapter 4, where it is argued that the reduction in the silicone oil's viscosity enables faster transport. A flow-rate feedback control mechanism takes advantage of this behavior by having the flow direction regulated electronically, but the flow rate controlled by temperature.

A capacitive flow-rate detection system has been developed to provide the appropriate feedback of the flow rate to control the droplet generator. By measuring the change in capacitance between the top plate and an electrode when a droplet moves between them, the

droplet's velocity can be calculated. Since droplets move faster at elevated temperatures, the location of a hot-spot can be interpolated.

The use of this flow-rate feedback control allows for faster heat removal in the presence of a thermal gradient, ensuring that hotter areas receive a larger number of droplets. This method minimizes the overhead needed for sensing and computation.

2.3.3 Electro- and Thermo-Capillary Feedback Control

This method utilizes both thermocapillary-driven flow and electrowetting to achieve thermal self-regulation of droplet flows without the need for any external feedback mechanism to sense the hot spots. The droplets are so small that surface tension is a major force in comparison to bulk forces, and a temperature gradient induces a pressure difference across the length of the droplet. Since the droplet would be on a hydrophobic substrate, it will move towards a hot-spot due to thermocapillary action. The droplet can then be removed from the hot spot by electrowetting and returned to the heat sink. No external mechanism is needed to drive the droplets towards the heat source; we have utilized the undesirable hot-spot to attract the cooling droplets towards it. Thus this process requires no external energy in doing so. The droplets will then be returned to a reservoir through electrowetting to dissipate heat.

Electro- and thermo-capillary feedback control would be the most attractive method of feedback since power is consumed only in returning the droplets to the heat sink and then placing them back on strategic locations on the chip. The power consumption in this scheme would be much less than the power consumption of the previous two schemes. However, in order for thermocapillary forces to be effective on droplets, droplet volumes will most likely have to be in the nanoliter and sub-nanoliter regime.

In all the schemes mentioned above, we are using a single phase cooling method, even though two phase methods are also feasible. Based on the measured flow rates attained

34

with the electrowetting-based system, it appears that single-phase cooling will suffice. In microchannels, two-phase systems typically need greater pressures to move the vapor bubbles that may form. In micropumps, an uncondensed vapor bubble can cause a vapor lock in the pump. Temperature can overshoot if a thin film of vapor forms over the hot surface preventing further supply of cold liquid and overheating the chip, therefore sufficient care has to be taken to ensure high flow rates.

2.4   IC Level Integration

Since the only active component in the digital microfluidic cooling architecture is embedded within a planar surface of the device, no additional components or structures such as pumps and valves are required. Hence, this architecture possesses inherent advantages in IC integration over other microfluidic solutions. Electrode sizes of 500μm and droplet volumes of 25nL have already been demonstrated [20], where performance in droplet formation and transport has been shown to improve due to this absolute scaling. Given these dimensions, a 1.5 X 1.5 cm^2 area can accommodate a 30x30 array of electrodes, allowing for high resolutions in droplet flow reconfigurability.

As we will discuss Chapter 3, we can eliminate the need for a conductive top plate by implementing grounding rails coplanar with the drive electrodes. This method isolates all microfluidic components and control mechanisms (e.g. supply voltage and fluidic inputs) to a single plane. Hence, the IC itself can act as the top plate without the need for it to be conductive, eliminating any additional processing steps.

2.5 Performance Comparisons for Flow-through Methods

2.5.1 Implementation Parameters

Table 2.1 is a comparison of the state-of-the-art microfluidic techniques used for heat removal. In other approaches, high voltage sources (for electrokinetic flows), piezoelectric actuators (for voltage induced droplet actuation), and pressure sources are required for fluid transport. Piezoelectric actuators have moving parts which might have potential reliability issues. While electrokinetic pumps do not have moving parts, power consumption would be high. If bubbles are generated due to electrolysis of water, it will reduce the flow rates in electrokinetic transport.

	Stanford's Approach [5]	GA Tech's Approach [6]	Proposed Approach
Principle of operation	Electroosmotic flow in a porous medium in 1D microchannels	Breakup of a liquid into droplets by a piezoelectric actuator and impingement onto the hot surface	Interfacial tension modification of droplets through electrowetting
Mode of heat transfer	Two phase	Two phase	Single phase (two phase possible)
Fluid input/output	Self contained	Self contained	Self contained
Orientation of Operation for Portable Applications	Not known	Horizontal, as the condensed fluid is returned to the source through gravity	Any, as gravity would not be significant compared to surface tension at such low volumes of droplets
Power consumption / Voltage requirement	Watts (100's of Volts)	Milliwatts (10's of Volts)	Microwatts (10's of Volts)
Flow rate	7 mL/min	N/A	10 mL/min
Cooling capability	Entire chip cooling in 1D fixed channels	Entire chip cooling	Entire chip cooling in 1D in open paths and on-demand 2D cooling of hot spots

Table 2.1: Comparison of the state-of-the-art microfluidic chip cooling technologies.

Unlike piezoelectric actuators, electrowetting-based systems would have no moving parts thus prevent mechanical reliability problems. Unlike electrokinetic actuation, electrowetting requires relatively low voltages and thus reduce power consumption. Very high

Author	Volume flow-rate (cm^3/s)	Heat-Flux Density (W/cm^2)	Velocity (cm/s)
Skidmore *et al.* [24]	45	1450	45
Colgan *et al.* [25]	25	275	6.25
Phillips *et al.* [26]	20	500	5
Pease *et al.* [27]	8.6	790	8.6
Pease *et al.* [27]	6.5	277	6.5
Pease *et al.* [27]	4.7	181	4.7
Patel *et al.* [28]	4.16	60	4.16
Jiang *et al.* [5]	2.5	9.8	1.25
Zhang *et al.* [29]	1.67	275	1.67
Yerkes *et al.* [30]	1.25	2	1.67

Table 2.2: Performance measures of several continuous-flow microfluidic-based cooling systems.

flow rates have been achieved in electrowetting transport without the use of high pressure sources since the flow is electronically controlled. The power consumption for transporting a droplet over one electrode is less than 1 μW. The orientation of an electrowetting system can be variable and is not limited to horizontal orientation. A unique feature of a digital microfluidic system over other microfluidic cooling technologies is the ability to cool hot spots on demand and on-the-fly. A single digital microfluidic platform can be adapted under a variety of cooling situations by optimizing the performance for each application and by simply reconfiguring the system in software.

From an implementation standpoint, a digital microfluidic-based solution to chip cooling is advantageous over current alternatives. However, one important measure, the effectiveness of droplets for heat transfer, must also be considered.

2.5.2 Heat-Transfer Parameters

A literature survey allows us to compare a variety of continuous-flow microfluidic-based cooling systems. Volume flow rates (i.e. how quickly liquid was pumped through the channels) and their effective heat dissipation were compared, as listed in Table 2.5.2 and shown Figure 2.3. Design parameters such as channel width and height were neglected, as

37

they were all similar in size (hundreds of microns).
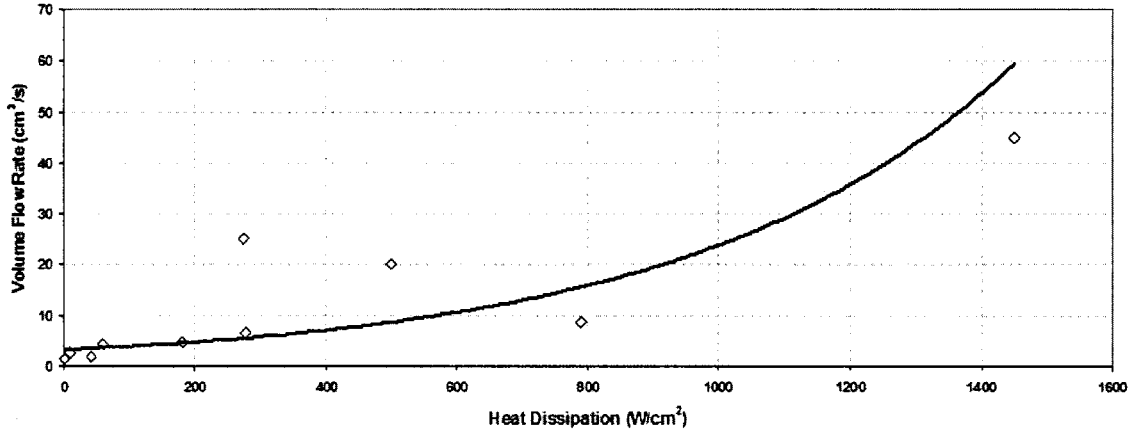
Table 2.3: Volume flow rates versus heat dissipation in a variety of continuous-flow based cooling devices.

To facilitate the comparison of our proposed droplet-based flow-through system with these continuous-flow systems, we calculate out the area over which the liquid is being pumped through, obtaining an effective flow velocity of each system. This allows us to determine a range of speeds at which cooling liquids are moving, as shown in Figure 2.4. We can see in the next graph that the flow velocities reach up to 45 cm/s to dissipate 1450 W/cm^2 of heat. A more realistic target would be to look at IBM's continuous-flow system where they dissipate 500 W/cm^2 of heat by pushing liquids at a flow velocities of 6.25 cm/s.

The reported maximum flow velocities we have reported in digital microfluidic systems is 2.5 cm/s. In the bottom graph of Figure 2.4, we can determine the range into where our technology roughly falls. By observing the cut-off line drawn in the graph, the maximum heat dissipation, assuming heat transfer characteristics are the same as continuous-flow systems, is 70 W/cm^2. This value already falls below current power densities of 90 W/cm^2 in today's commercial systems. Additionally, we are neglecting the fact that in continuous flow systems, fluid is pushed through silicon channels which allow for heat to conduct

38
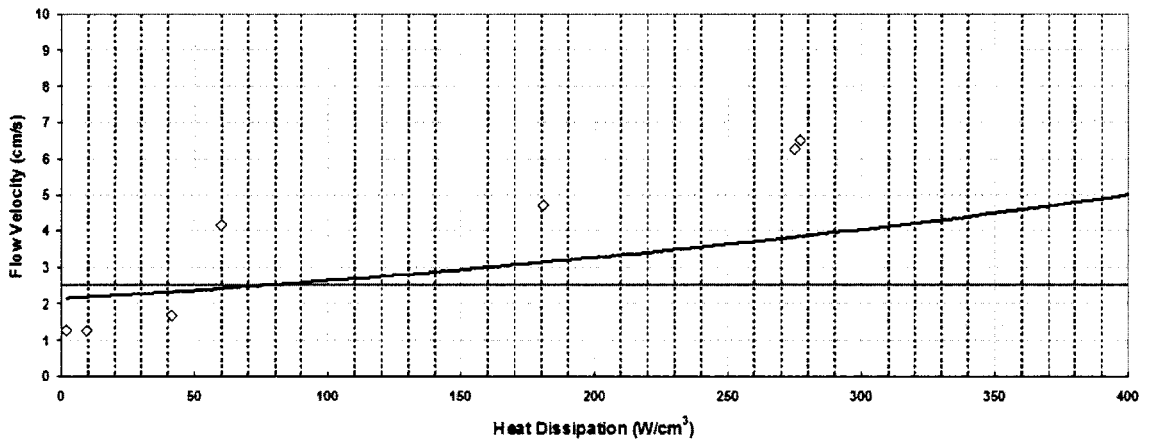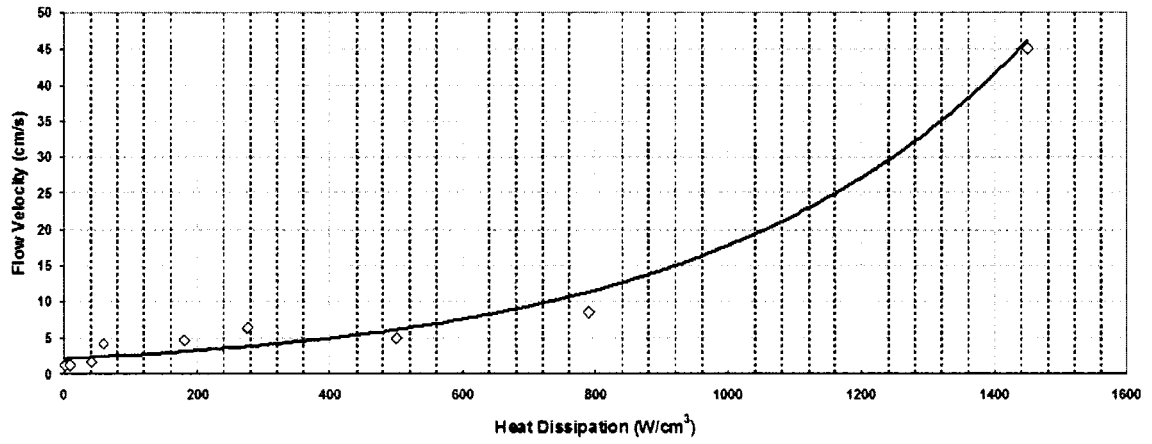
Table 2.4: Flow velocity versus heat dissipation in a variety of continuous-flow based cooling devices.

into the cooling liquid from all four sides of the wall, whereas in our system, heat is largely conducted from only the topside of the droplet and the rest through the silicone oil of much lower thermal conductivity.

The numbers here suggest that the limits of transport speeds must be pushed higher in order for a flow-through based method to adequately cool current and future microprocessors. We must consider, however, that many of the limitations in transport speeds lie in alterable parameters such as the dielectric used to insulate the electrodes from the droplet. Current dielectrics exhibit contact angle saturation and dielectric breakdown when larger driving voltages are used to increase the speed of droplet transport. However, a wide range of dielectrics have not yet been tested; new materials can significantly increase the maximum attainable droplet speed.

Additionally, heat transfer into droplets can be greatly improved by either doping or finding oils that result in higher thermal conductivities.

2.6 Chapter Summary and Conclusions

An electrowetting-based "digital" microfluidic system developed at Duke University is the basis for the development and study of an adaptive IC cooling architecture. There are number of advantages in using this approach, namely the reconfigurability of droplet flow and seamless integration with the target IC.

In this chapter, we outlined several criteria necessary to achieve a reconfigurable IC-level cooling solution. We then described the elements that comprise a digital microfluidic device: droplet formation and dispensing, transport, and recycling. Based on these elements, we proposed two cooling architectures that can be easily integrated with an IC. In the flow-through based approach, a large number of droplets are dispensed and transported over any arbitrary hot-spot, carrying away heat as it returns to the cooled reservoirs. In the programmable thermal switch-based method, liquid-metal droplets are used to create a pro-

grammable thermal conductance layer, resulting in a uniform temperature profile despite the non-uniform power densities in the target substrate.

In order to make these approaches "adaptive," several thermal profiling feedback mechanisms were introduced. The on-the-fly reconfigurability of droplets coupled with these feedback mechanisms enables real-time detection and cooling of hot-spots.

Chapter 3

Technology Development

In Chapter 2, we proposed two adaptive IC chip cooling approaches based on the digital microfluidic platform, which until recently, has typically been targeted toward biological and chemical lab-on-a-chip applications. As a result, many of the technological strategies for digital microfluidic devices have been geared toward biological sample handling and on-chip biological and chemical assay development. While some of these strategies can be adapted for chip cooling applications, new challenges specific to chip cooling need to be addressed. For example, methods for temperature measurement and hot-spot detection in a digital microfluidic device have never been demonstrated and need to be developed. Furthermore, issues of platform integration with existing devices (i.e., the IC substrate) need to be explored. In this chapter, we discuss the necessary strategies that will enable the development of a digital microfluidic adaptive cooler.

3.1   Temperature Measurement

One of the first challenges that needs to be addressed is the development of a temperature measurement method that can be integrated into our system. In biological applications where temperature plays a critical role (i.e. on-chip polymerase chain reaction (PCR)), thermocouples have traditionally been used [31]. Thermocouples consist of two wires of different metal alloys shorted together and work by generating a temperature-dependent voltage across the junction, referred to as the Seebeck voltage. The Seebeck voltage is the result of temperature differences causing current to flow in a circuit made of dissimilar metals. The resulting voltage is typically on the order of millivolts. While thermocouples are relatively low in cost and can cover a wide range of temperatures (typically 0

to 800 °C), the thinnest probes available have a thickness of 25μm, which can interfere with droplet transport. Furthermore, thermocouples typically have a measurement error of >1°C, which is unsuitable for temperature-critical applications such as PCR or sensitive thermal profiling. Integration and alignment of an array of thermocouples onto our device would thus be bulky and impractical. The use of thermocouples in this work was therefore limited to cases where only a few measurement points were needed and spatial resolution was not critical, such as the measurement of system-wide temperatures in the experiments performed in Chapter 4. For cases where a higher resolution and continuous thermal profiling was required, two alternative methods were employed: infrared imaging and resistive temperature device (RTD) integration.

3.1.1 Infrared Imaging

Infrared (IR) imaging works by collecting infrared light emitted by a heated object in much the same way that a conventional camera collects visible light. Heat from an object, which is emitted as infrared radiation, is collected through and focused using an IR-filter lens which is typically coated with Germanium, an IR-bandpass material. The infrared light is then captured onto a bolometer or an array of infrared detector elements. Thermal IR cameras operate in the long-wave IR spectrum (3 to 30μm), and can sense temperatures ranging from -20 to 2000 °C, with a typical error of about 0.5°C. This method requires no contact with the target object, making it the least intrusive method to measure heat.

Despite the many advantages of this non-contact method, thermal IR imaging has several limitations associated with it. First, the resolution of the infrared imager depends on the emissivity of the material being imaged. The infrared energy emitted by an object differs according to the composition of the object's surface and the physical state of the object. Water and polished copper, for example, emit different levels of infrared energy since they have very different emissivities (0.98 versus <.05), even though they are at the

same temperature. Furthermore, if the polished copper begins to oxidize, its emissivity increase accordingly. In order to obtain the true temperature reading, it is thus necessary to calibrate the infrared camera for the emissivity of each object being measured, as well as account for any surfaces changes of the target material. This complicates the calibration of the IR camera by requiring a separate calibration for each material observed. A second limitation of IR imaging is that many materials that are transparent in the visible spectrum are opaque in the long-wave IR spectrum, and vice-versa. The glass and plastic materials typically used as a top plate in our system are examples of such materials. This imposes serious restrictions on the type of materials that are compatible with our system. For example, while IR-transparent materials, such as silicon and zinc-selenide (see Figure 3.1) are available for use as a top plate in our system, the machining of holes as fluidic input ports is prohibitively difficult to implement. Fortunately, a solution to this problem became apparent during the development of printed circuit board based microfluidic devices discussed later in this chapter. The ability to machine PCB material easily allowed us to drill fluidic input ports through the microfluidic chip itself, a technique not possible with glass substrates traditionally used.

The infrared imager used in this work is a long-wave IR camera (JTL1 Infrared Imager, Edmund Optics, Barrington, NJ, USA) with a 50mm IR-transparent Germanium lens. Due to the inadequate field of view provided by the stock lens, extension rings were machined in aluminum to heights corresponding to the desired field of view. The camera has a frame rate of 30 frames per second, a resolution of 160h x 120v pixels, and is equipped with a programmable range and offset setting to image a user-designated range of temperatures. Settings can be programmed and images can be directly downloaded from the infrared camera through an RS-232 serial connection. A customized program was written in Microsoft Visual Studio C++ to allow for automated control of the camera, as well as to coordinate and record temperature readings during calibration.

44
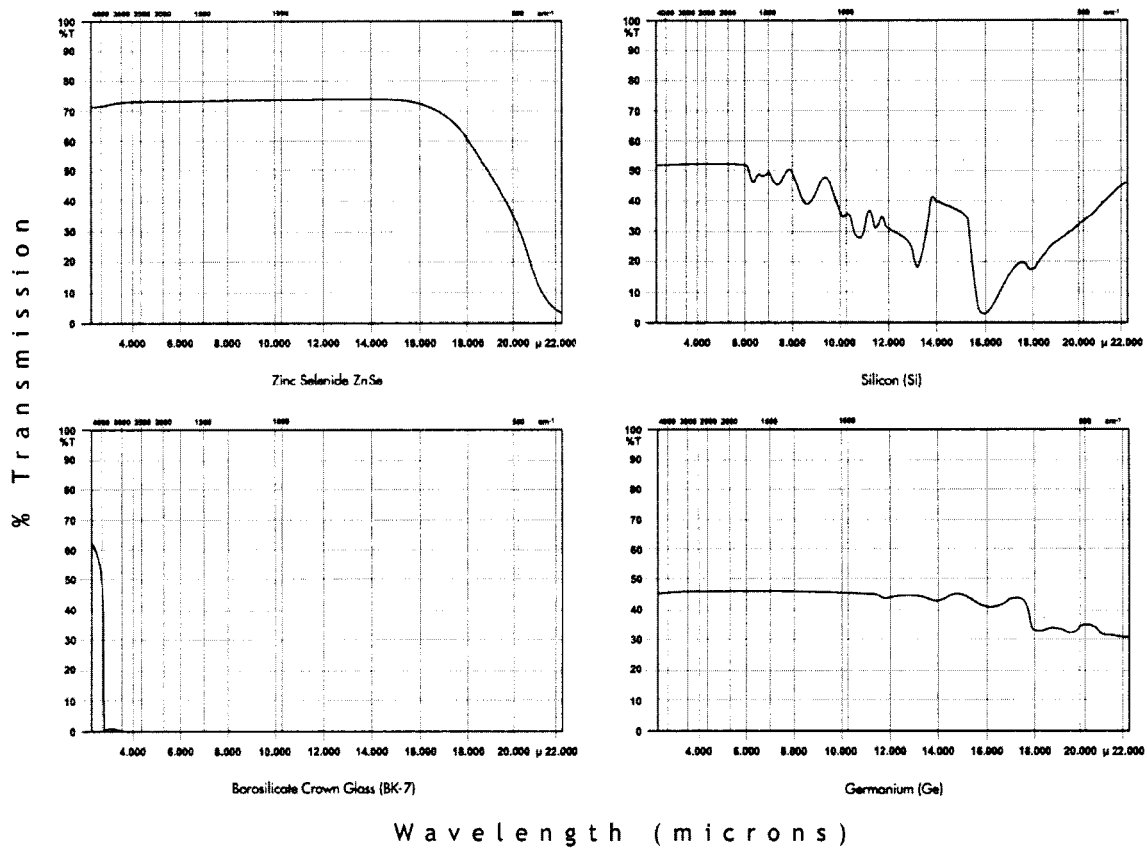
Figure 3.1: Transmission graphs of ZnSe, Si, Borosilicate Glass, and Ge. The typical range of wavelengths used for our studies is 8 to 14 μm. Note that the transmissivity of borosilicate glass is zero throughout this range.

45

Figure 3.2 is a screen capture of the program written to control the JTL IR camera. This program was found to be very useful when calibrating the camera for various materials, as it automated many of the functions necessary to find the correct range and offset settings.
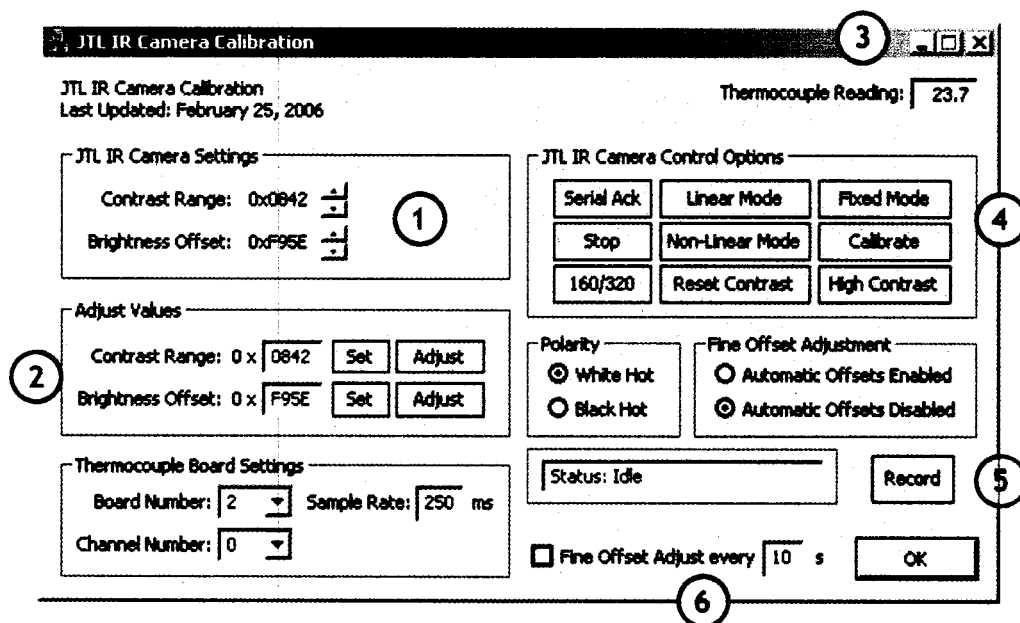
Figure 3.2: Screen capture of the software written for the JTL IR Camera. The software consists of 1) display and ability to increment/decrement the contrast range and brightness offset of the camera, 2) the ability to arbitrarily set the range and offset values, 3) the display of the temperature as read from a thermocouple, 4) the entire array of commands to program the IR camera, 5) the ability to record the thermocouple data at a given sampling rate, and 6) the ability to enable the fine offset adjustment (since this camera is an uncooled camera, this feature is necessary to correct for the bolometer's sensitivity to the ambient temperature).

Calibration Methods

Calibration for the JTL IR camera was performed by using a silicon wafer as a heater source and fixing it to the designated target material that will be calibrated. In the case of a glass coverslip, the glass was fixed to a strip of silicon using epoxy, making sure the epoxy does not wick into the gap between the silicon and the glass (see Figure 3.3). Resistors (35 Ω) were put at the far ends of the silicon strip. Applying current through the resistors

46

provided heat across the silicon wafer, and due to the silicon's high thermal conductivity, uniformly heated the glass coverslip.
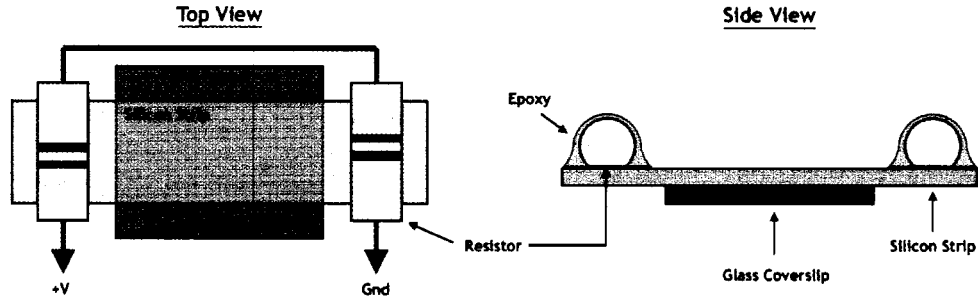
Figure 3.3: Schematic of the IR camera calibration setup.

Rough calibration settings for the JTL IR camera were obtained by having two silicon/coverslip strips side by side, and by setting one to an upper limit temperature of 90°C, and the other one to a lower limit temperature of 30°C. The range and offset settings were adjusted such that the hot strip showed the highest white values (close to 255 on an 8-bit grayscale), and the cool strip showed the lowest dark values (toward 0 on an 8-bit grayscale). The hex-value setting that was recorded was SPAN=0x0842, and OFFSET=0xF95E, with the high contrast mode ON.

Actual calibration curves were then obtained by placing a thermocouple onto the glass coverslip, and recording the video on a digital video recorder as the temperature is being simultaneously recorded through the JTL IR Camera Calibration software.

The video was then post-processed using a custom-written MATLAB 6.0 R12 program (see Appendix A) which reported relative intensity units as a function of time. This allowed us to match the time-varying intensity with the time-varying temperature as recorded from the thermocouple such that a calibration curve was obtained.

Calibration was performed for both the IR camera looking through the silicon down to the coverslip as well as the bare coverslip itself. A sixth-degree polynomial curve-fitting algorithm was applied to the data. The raw data and the calibration curve-fit for a repeated

47

Calibration Curve
Viewed through Silicon on Glass Coverslip

$y = 4.2386571721E-12x^6 - 2.1121376884E-09x^5 + 2.6582428021E-07x^4 + 3.0737453136E-05x^3 - 1.0616109265E-02x^2 + 1.0722875935E+00x + 2.0676960371E+01$

$R^2 = 9.9634718049E-01$

Calibration Curve
Viewed through Silicon on Glass Coverslip

$y = 4.8869150507E-12x^6 - 3.1105136873E-09x^5 + 6.9473306212E-07x^4 - 4.7241062383E-05x^3 - 4.2123435831E-03x^2 + 8.6262063280E-01x + 2.2254384024E+01$

$R^2 = 9.9698221115E-01$

Figure 3.4: Calibration curves obtained for two repeated experiments (top and bottom graphs) for a glass coverslip attached a silicon heater. This data was obtained using the JTL IR camera which views the glass coverslip through the silicon heater. The sixth-degree polynomial curve-fitting is shown for both runs. The error of the curve fits between the two repeated experiments was calculated to be less than 0.5°C throughout the entire calibration range.

experiment on a glass coverslip is shown in Figure 3.4. The results were checked in a math analysis program (Maple) to check for error between the multiple runs of calibration. The error was found to be $<0.5°C$ throughout the entire calibration range, suggesting that this method of calibration leads to low error.

Image-processing Techniques

Once calibrated, the IR camera can now be used for experiments requiring temperature measurements. The video from each experiment is digitally recorded, where it is later post-processed using the Droplet Cooling Measurement Tool software written in MATLAB.

The temperature of a region of interest (ROI) can be obtained for each frame of the video from which the program outputs a temperature vs time data. An example image of a post-processed frame is shown in Figure 3.5. Details and MATLAB code for the Droplet Cooling Measurement Tool can be found in Appendix A.

(a)   (b)
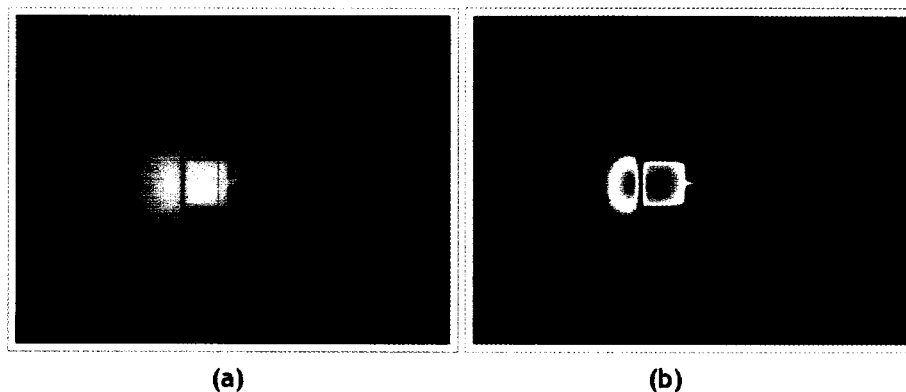
Figure 3.5: Top view of a linear array of seven electrodes with a simulated hot-spot in the center electrode as captured by the infrared camera. Images are shown in a) white-hot gray scale and b) false color.

3.1.2 On-Chip Resistive Temperature Devices (RTDs)

Resistive temperature devices (RTDs) are metal resistors whose resistance increase with increasing temperature. RTDs are typically made from platinum, copper, and nickel as these metals offer the best linearity. The metals are either wire-wound on a form or vacuum-deposited or sputtered on an insulating surface as a thin film device. Thin film versions typically have temperature limits of -200 to 650°C and exhibit an error that is dependent on the voltmeter used to measure the resistance of the device. Figure 3.6 shows the resistivity response of platinum, copper, and nickel RTDs with a 100Ω nominal resistance at 0°C.
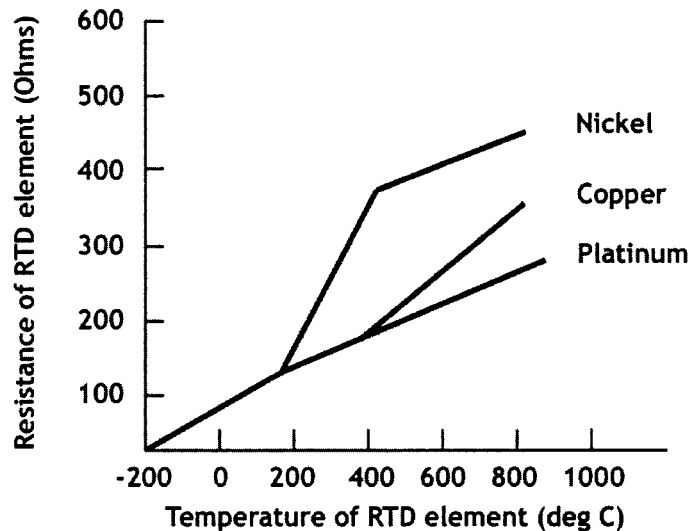
Figure 3.6: Resistance response to temperature of 100Ω nominal RTDs using platinum, copper, and nickel metals. The linear temperature response of these metals make them attractive for measuring devices. [7]

There are three different configurations by which to assemble thin film RTDs. The first is a 2-wire input, which is the easiest and cheapest to construct. The two wires that provide the RTD or thermistor with its excitation current are also used to measure the voltage across the sensor. Because of the low nominal resistance of RTDs, measurement accuracy can be drastically affected by lead wire resistance. For example, lead wires with a resistance of

50

$1\,\Omega$ connected to a $100\,\Omega$ platinum RTD cause a 1% measurement error. A 3-wire or 4-wire connection method can eliminate the effects of lead wire resistance by placing leads on a high impedance path through the measurement device, effectively eliminating error caused by lead wire resistance. Using the 4-wire method provides the most accurate measurement, as excitation current flows through 2 wires and the other 2 wires are used to measure the voltage across the RTD. The circuit schematics for the 2-, 3-, and 4-wire configurations are shown in Figure 3.7.

2 WIRE	Used where lead length is short. There is no compensation for resistance of lead wires.
3 WIRE	Most common type of RTD assembly. Typically connected to standard bridge circuit, which allows lead wire resistance to be compensated.
4 WIRE	Where higher accuracy is demanded. Lead wire resistance errors are eliminated in this configuration by measuring the voltage across the RTD element supplied with a constant current.

Figure 3.7: Circuit schematics for input to an RTD using a 2-, 3-, and 4-wire configuration.

The maximum current used for thin-film RTDs should be kept low ($\sim$0.5 to 2 mA) to limit self heating effects. Furthermore, a quality constant current source is recommended to be used to minimize error.

In our system, RTDs were implemented by patterning RTD elements to either the top or bottom plate of our devices. Copper or platinum was sputtered on a glass substrate with a thickness of $\sim$1000 Å and patterned using either a lift-off, etching, or laser direct-write process. A bonding layer of either chrome or titanium ($\sim$200 Å) was used to promote adhesion between the metal and glass. The nominal resistance of the RTDs varied anywhere

51

between 200-2500Ω, depending on the dimensions of the RTD.

Calibration Methods

Calibration of these devices was initially performed using a 4-wire configuration against a thermocouple. A thermal couple was placed on top of the RTD using tape, and the heater was cycled through various temperatures. The resistance of the RTD and the temperature of the thermocouple were recorded, producing a calibration curve. Figure 3.8 shows the results of this calibration method.

While this method of calibration appeared to be accurate for a single RTD, calibration of multiple RTDs using this method was found to be imprecise. Significant variation of absolute temperature among the multiple RTDs was observed.

An alternative method for calibrating the platinum RTD top plates was developed. The 4-wire measurement protocol was used with the supply current fixed using a constant current supply (CALEX 930 Programmable Current Source, CALEX Mfg Co., Concord, CA). The entire substrate on which the RTDs were patterned was placed in a bath of mineral oil set at a constant temperature, which was measured through a thermocouple. The top plate was allowed to reach steady state by leaving it in the system for a fixed amount of time, typically 5 minutes for the higher temperature, and 10 minutes for the lower temperature. The voltage of each RTD and the temperature of the bath were recorded, and the slopes and offsets were calculated. This method is different from the previous method in that only two data points were taken instead of a continuous range of temperatures. The two temperatures chosen were typically 28°C and 100°C.

A customized program was written in Microsoft Visual Studio C++ .NET to facilitate the acquisition and calculation of the calibration data, and is shown in Figure 3.9

This calibration proved to be more precise than the previous method. RTD-to-RTD temperature variations were typically less than 0.5°C, much lower than the 1-5°C seen
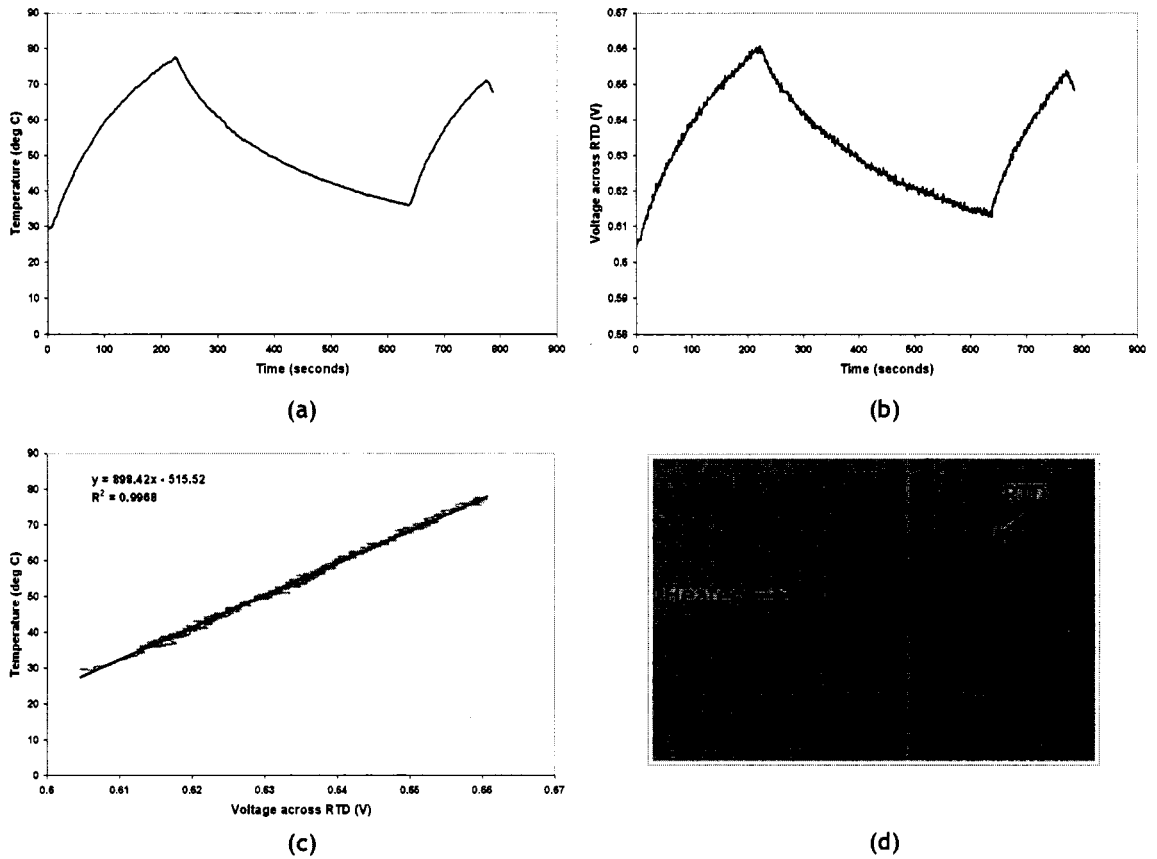
Figure 3.8: The calibration data of a thin-film copper RTD (d) with a nominal resistance of 230Ω. A constant current supply was used to provide 3 mA to the RTD in a 4-wire configuration. An external heater source was used to vary the temperature of the RTD and measured using a thermocouple (a). The resulting changes in voltage across the RTD was recorded (b), and a calibration curve was produced (c). Linearity was observed and there was virtually no hysteresis effect.
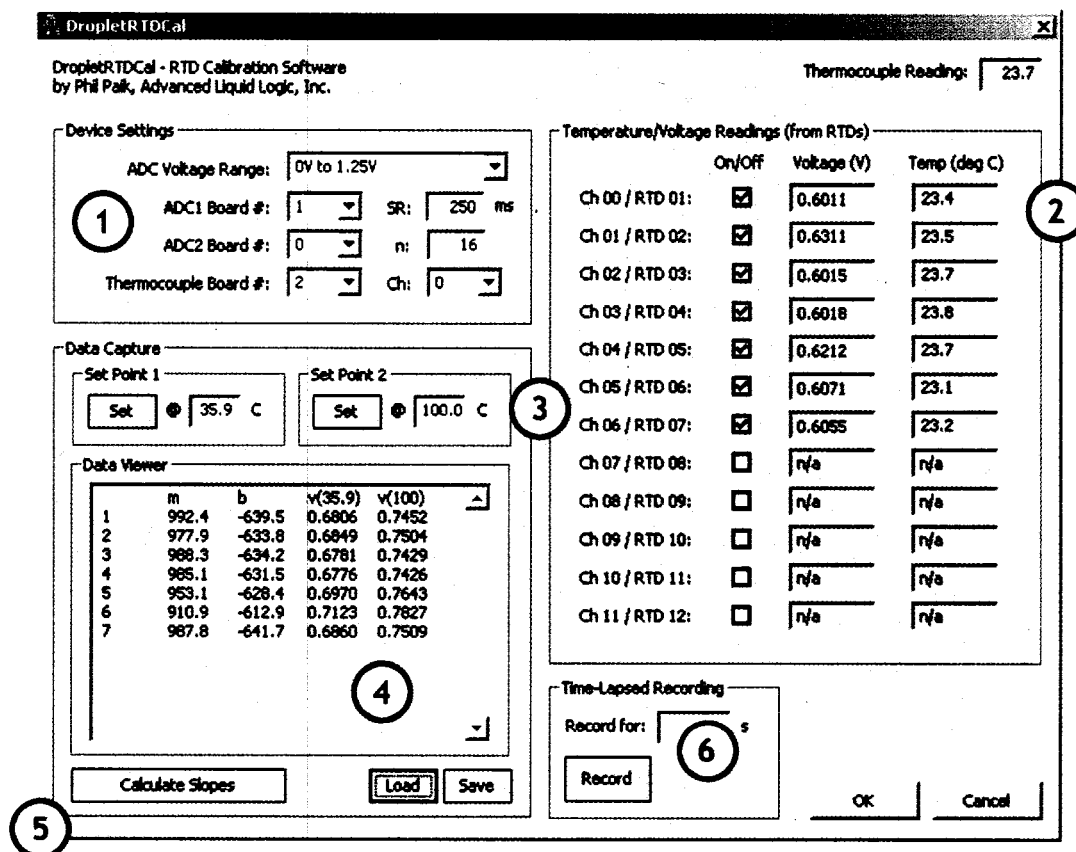
Figure 3.9: Screen capture of the software written for the JTL IR Camera. The software consists of 1) device settings for the data acquisition boards, 2) a temperature and voltage readout of the RTDs, 3) data capture feature which allows the temperature and voltage to be recorded, 4) a readout of the raw data and calculated slopes and offsets (if any), 5) the ability to calculate the linear slope given two data points, and 6) the ability to perform a time-lapsed recording to capture any transient changes in temperature.

previously. This error can be minimized by maintaining the surface of the RTD clean. Since the surface of the top plates was sensitive to contaminants, moisture and dirt end inadvertently deposited on the surface resulted in changes in resistance of the RTDs and disrupting the calibrated values. Thus, it was important to keep the surface clean when calibrating and when in use. The RTD devices were therefore sonicated in a 1g/1L solution of Alconox in DI water for at least 5 minutes, after which they were sonicated in an ethanol bath for another 5 minutes.

3.2   Hot-Spot Source Design

A method to simulate hot-spots on-chip was a second challenge that needed to be addressed. Since droplets would ultimately be in direct contact with the target IC to be cooled, the hot-spots need to be simulated and integrated into either the top plate or bottom microfluidic plate of our system. Furthermore, the simulated hot-spot must be programmable such that the amount of power delivered to the hot-spot could be varied for characterization studies. Methods to simulate these hot-spots included either an array of surface mount resistors or thin-film heaters.

3.2.1   Surface Mount Resistors

Surface mount (SMT) resistors are passive resistive devices that have package footprints as small as 1mm x 0.5mm. A densely-packed array of SMT resistors can be mounted on a PCB. This design allows for power lines to be routed to each resistor, allowing independent control for each element within the array. This array can then be interfaced with either the top or bottom plate of the digital microfluidic cooling device, as shown in Figure 3.10.

Top View

SMT Resistor

SMT Resistor Board

Electrical Contacts

Side View

SMT Resistor Board

Si Top Plate

Fluid Layer

Microfluidic Chip
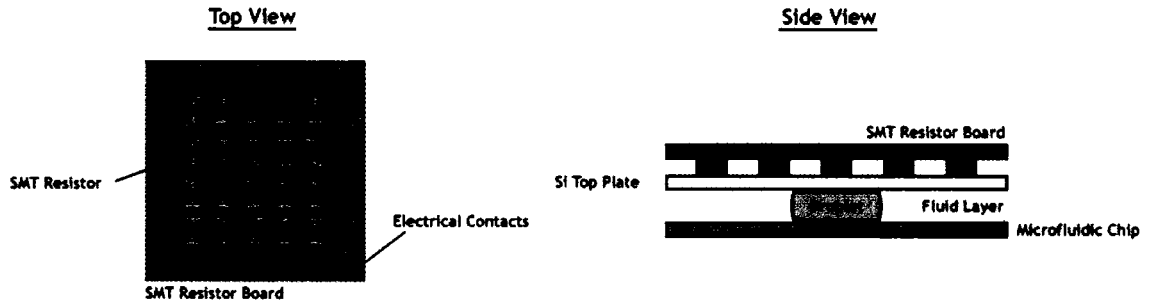
Figure 3.10: Surface mount resistor board used to simulate hot-spots. The top view shows the schematic of an array of SMT resistors mounted on a PCB board. The side view shows the assembly of the resistor array with the top plate of a digital microfluidic chip. Silicon would be an ideal top plate in this setup as its low thermal resistance would allow the transfer of heat between the simulated hot-spots and the droplet be maximal.

3.2.2 On-Chip Thin-Film Heaters

Thin-film heaters are resistive devices that generate heat when provided with currents by way of Ohm's power law. Using microfabrication techniques, these thin-film heaters can easily be made to dimensions on the order of hundreds of microns. For the purposes of our studies, we decided to limit the size of the hot-spot to the electrode size ($\sim$1mm x 1mm). The resistances of the heater should be kept relatively low ($<100\Omega$) in order to keep the operating voltages low, as large voltages can potentially interfere or compete with electrowetting processes. Due to the various hot-spot designs we have implemented over the course of our studies, the exact design and operating conditions used will be specified in the text.

Initial experiments using the heaters for microfluidic experiments revealed that the insulator used to cover the heaters would sometimes hinder droplet transport. Proper electrical insulation is necessary in order to prevent the water-based droplet from causing shorts in the RTD and heater devices. The insulator that was initially used was Parylene C, which was deposited at a thickness of 2μm.

An experiment was performed to test transport characterization when a droplet was

transported to and from a heater element. RTD-001 plates were silanized (to promote Parylene C adhesion) and coated with 2μm Parylene C, followed by a brush coating of 1% Teflon AF which was baked at 110°C for 15 minutes. The RTD-001 top plate was assembled with the PCB-R005 TM-01 microfluidic chip.

Top View
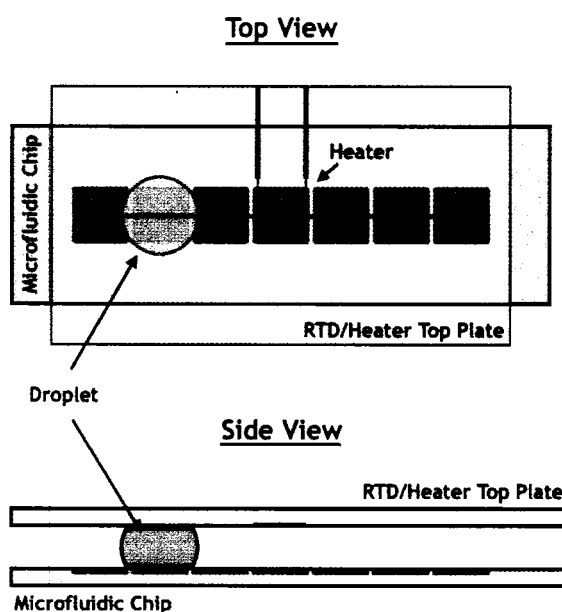
Figure 3.11: Image showing experimental setup

A droplet was dispensed and transported across an RTD/heater element at a switching frequency of 1 Hz. The current through the RTD was 1 mA, and the heater was applied to a temperature of 75°C. After repeated experiments, it was evident that droplet transport would eventually fail as it approached or was on the heater. It was initially believed that thermocapillary effects had prevented the droplet from being moved once it was heated. Further studies revealed that the area was instead acting hydrophilic through the remainder of the experiment. Disassembly, cleaning, and reassembly of the chip resulted in normal function of droplet transport until the heater was once again actuated.

Further investigation revealed that when potential to the droplet was inverted (i.e. the grounding electrode was raised to a high potential), the droplet would wet the lines leading

57

to the RTDs in the top plate. This behavior suggests that either the quality of the Parylene C coating or the thickness was insufficient, thus a thicker insulator was tested.

The experiment was repeated using 2 mil (50μm) thick Kapton tape. While droplet transport performed normally when the heater was turned off, the same behavior was observed when a potential was applied to the heater. The insulator was therefore changed again to a thin glass coverslip (170 μm). Droplet transport performed normally regardless of the state of the heater, and transport appeared unhindered across a thermal gradient of 25°C to 80°C, demonstrating that droplet transport was possible through thermal gradients.

3.3 Design, Fabrication, and Testing of Initial Flow-through Prototypes

Initial prototypes to investigate hot-spot cooling using the flow-through method were designed to embed the thin-film RTD and heaters within an electrode. The prototypes were fabricated on glass using standard microfabrication vacuum processes. Each chip consisted of a linear array of 1mm x 1mm electrodes with either embedded RTDs, heaters, or both. Due to the requirements of the RTD metal, 1000 Å of copper was used on top of a 200 Åchrome bonding layer. In order to maximize electrode area, the spacing between the heaters, RTD and electrodes were (3μm).

Initial testing of these chips was performed using 1μm thick parylene as the insulator layer. Teflon AF was spin-coated to serve as the hydrophobic layer. Transport of droplets up to 16 Hz was demonstrated at 50V while the heaters and RTDs were kept floating. Furthermore, the heaters and RTDs, which both operated around 5V, were shown to work as expected. However, the combination of operation of either the electrodes and RTDs, electrodes and heaters, or all three devices resulted in breakdown in the insulator and electrolysis at the metal lines. Figure 3.13 shows the typical result of the electrodes when this type of breakdown occurred.
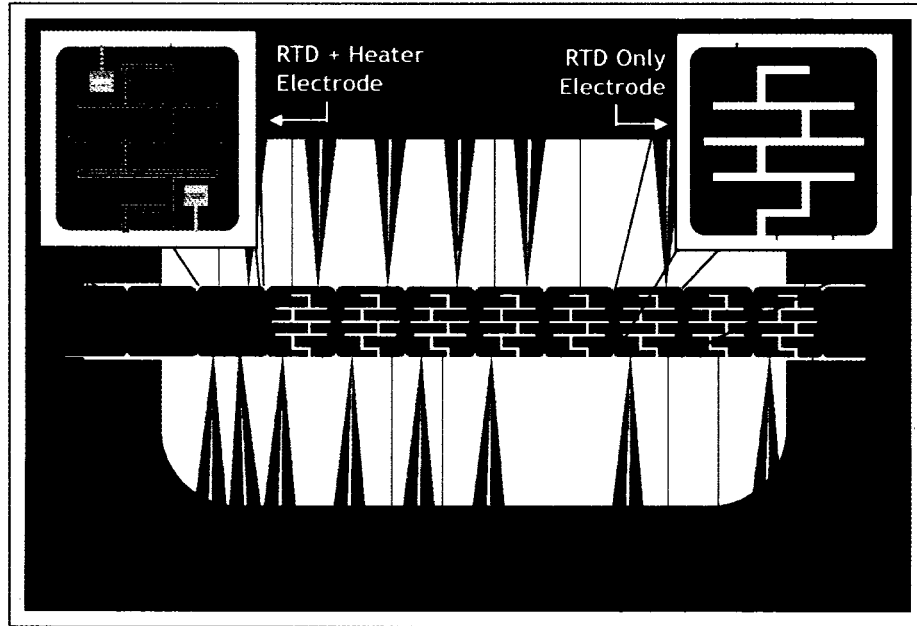
Figure 3.12: Top-view schematic of initial hot spot cooling prototype. Two reservoirs are connected by a linear array of 12 electrodes. Seven electrodes contain two RTD elements each, and one contains a heater used to simulate a hot spot.
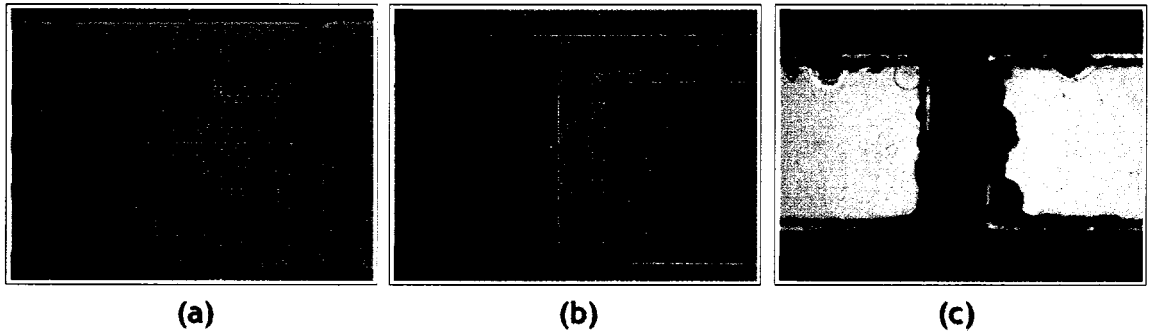
Figure 3.13: Breakdown of an electrode/heater/RTD system, producing fatal opens in the metal lines. When only the electrodes and RTDs were used (i.e. the heater was kept floating), electrolysis occurred near the areas between electrode and RTD (b). Operating the heater in addition to the electrodes and RTDs showed electrolysis near the RTD/heater junction as well (c).

59

The exact cause of this behavior is unknown and is still under investigation. It is suspected that there was either improper coverage of the parylene insulator layer, or that the electric fields produced between the much more thinly spaced (3μm) copper lines accelerated the breakdown of parylene. At this point, the cost of using these microfabrication techniques as a prototyping platform led us to explore alternative methods to characterize hot-spot cooling.

3.4 Digital Microfluidics on Printed Circuit Board (PCB)

Until recently, digital microfluidic chips have been fabricated using expensive microfabrication techniques, where electrodes have been patterned on a glass wafer using vacuum processes. A hybrid approach has been demonstrated where interconnects were formed on a multi-layer PCB, but the electrodes were still formed using vacuum microfabrication processes [32]. Furthermore, all electrowetting-based droplet manipulation systems demonstrated thus far require a top plate to provide continuous ground to the droplet, complicating the chip assembly requirements. This is particularly problematic when an infrared transparent material is required for the top plate to view the temperature variations in the fluid layer. As an alternative to glass-based vacuum processes, we have developed and demonstrated the fabrication of ready-to-use digital microfluidic chips through PCB processes without any additional post-processing steps [33]. Additionally, we eliminate the need for a conductive, or any, top plate by implementing grounding rails coplanar with the drive electrodes.

A schematic view of a conceptual PCB-based digital microfluidic chip is shown Figure 3.14. The chip consists of a PCB substrate upon which copper is patterned to define the electrodes. Via holes are drilled into each electrode to provide electrical contacts to the backside of the PCB substrate. Grounding rails are patterned alongside all the drive electrodes to provide a continuous ground connection to the droplets, and a liquid pho-
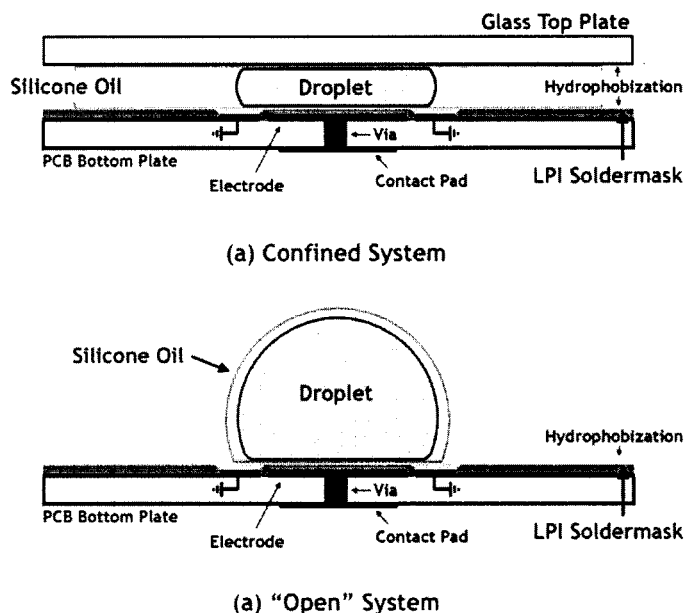
Figure 3.14: Side view schematic of a digital microfluidic chip on PCB in (a) a confined system and (b) an open system. Note: Droplet transport occurs in the plane of the page

toimageable (LPI) soldermask is patterned to act as an insulator. The LPI soldermask covers the entire chip, except areas where there are grounding rails. A layer of Teflon AF is brush-coated on the surface of the processed PCB chip to render the surface hydrophobic. A droplet sits on top of the electrode and is of sufficient size so that it is in continual contact with one or both of the grounding rails.

The first prototype of a PCB-based digital microfluidic chip was fabricated through a vendor capable of patterning 4-mil line width traces and 3-mil line spaces. The prototype consisted of a square loop of 1.5 mm pitched square electrodes that was nine electrodes long on each side. The fabrication steps for this run are outlined in Figure 3.15.

Transport and mixing of microliter-sized droplets are shown in Figure 3.16, with and without the presence of a top plate. When a top plate was used, the entire confined area was filled with 1 cSt silicone oil. At a gap height of $600\mu m$, the size of each droplet used was $2.5\mu l$. In the absence of a top plate, a droplet volume of $6\mu l$ was used, and a smaller
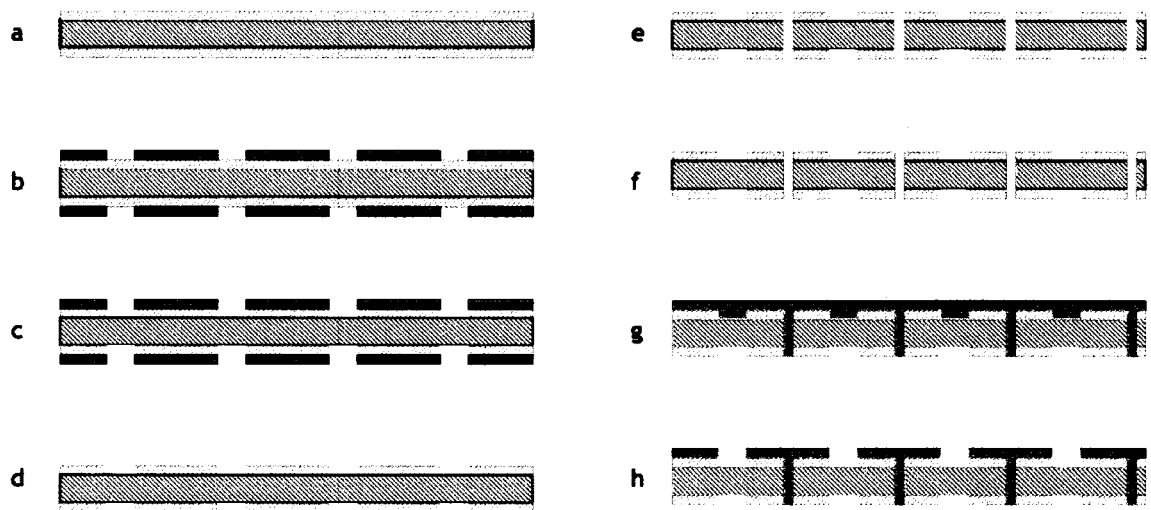
Figure 3.15: Buildup process of the initial PCB digital microfluidic chip prototype. A 32-mil thick PCB board with a 5-mil laminate of copper on both sides was used as the starting substrate (a). Both the top and bottom sides were patterned using a photomask (b, c), then etch-off processes (d), and via holes where electrical contacts were to be placed were mechanically drilled (e). The copper was then plated to build up the copper in the via hole (f). LPI soldermask was applied to the top side of the board (g), and patterned to expose the ground rails (h). The via holes were large enough such that LPI soldermask completely filled the holes, leaving the top surface planar. The final final thickness of the copper was $\sim 25 \mu m$. The spacing between each electrode was $\sim$3-4 mils. The thickness of the soldermask was $\sim 17 \mu m$, or 0.7 mils.

droplet (~2μl) of 1 cSt silicone oil was dispensed onto the droplet. This provided enough volume for the silicone oil to completely surround the droplet upon visual inspection from both the top and side views. Droplets which were transported at higher frequencies (>8 Hz) in this topless, open system resulted in a trail of smaller oil droplets left on the surface.
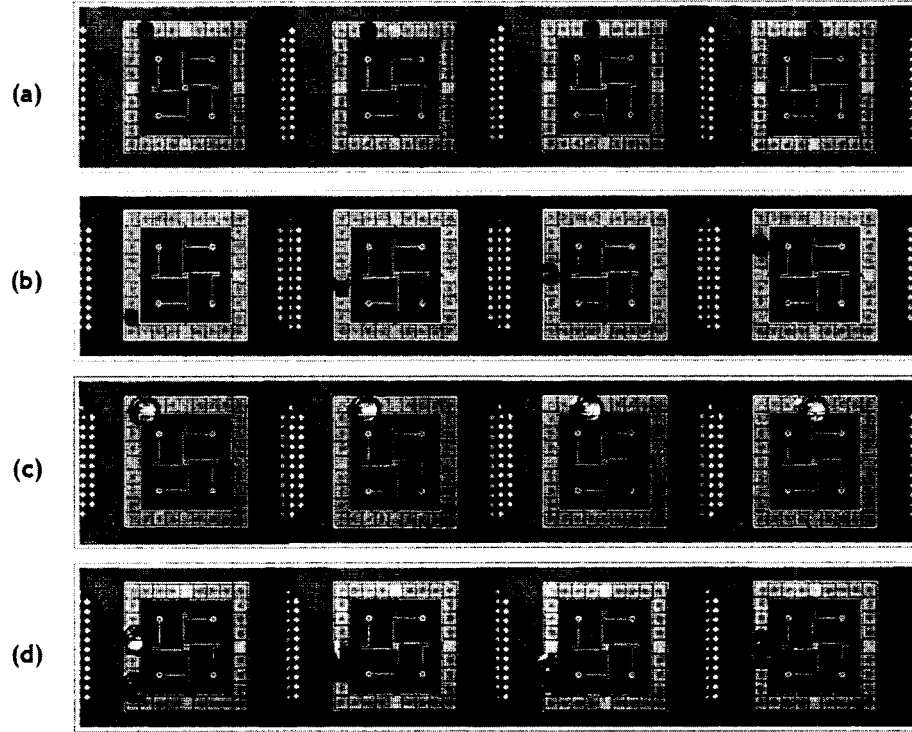
Figure 3.16: Top view of an image sequence demonstrating transport (a) and mixing (b) for droplets confined by a top plate (600μm), and transport (c) and mixing (d) for droplets in an open system. Mixing was performed at a switching frequency of 8 Hz and completed within 5s for two 2.5μl confined droplets, and within 1.8s for two 6μl droplets in an "open" system. Mixing in an "open" system is shown to perform faster than that studied in a confined system.

As shown in Figure 3.17, the operating voltages ranged from 140-260V and 125-220V, respectively, depending on the switching frequency of the droplets. This suggests that droplet actuation was facilitated by the absence of a confining top plate, possibly due to the reduced drag experienced by the unconfined droplet. Electrolysis of the droplets, typically due to improper coverage of the insulator as shown in Gong *et al.* [32], was not observed

using LPI soldermask as an insulator up to the maximum tested voltage of 350V. Insulator charging, however, was experienced beyond 300V.
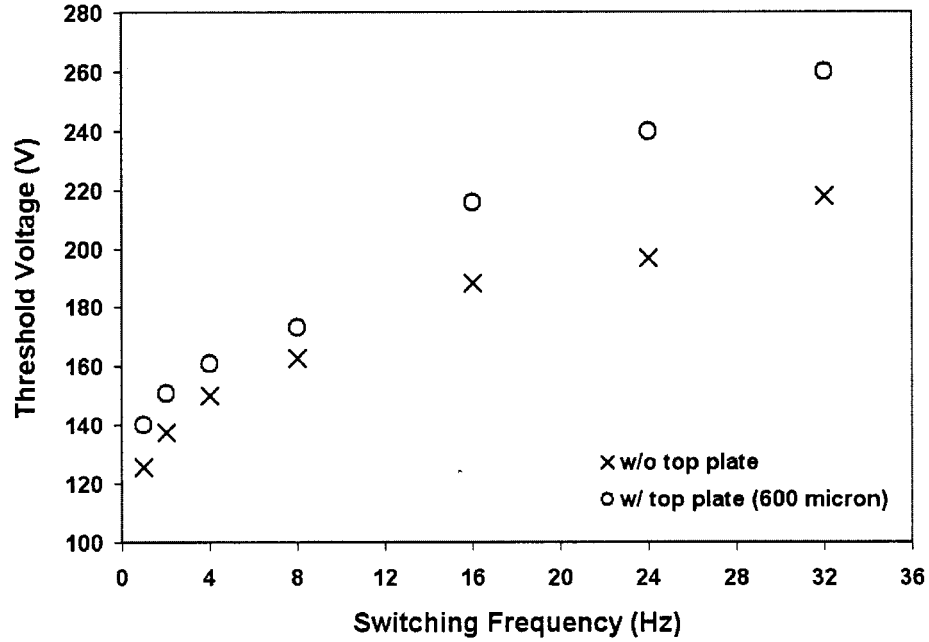
Figure 3.17: Minimum voltage requirements for droplet transport at a given switching frequency.

Later prototypes involved smaller traces and space requirements to accommodate electrode pitches of 750 μm. Furthermore, a dry-solder mask layer was added to serve as a gasket layer which would provide the proper spacing and define the reservoirs from which droplets could be dispensed. Several iterations of design changes and fabrication runs were tested before a final method, shown in Figure 3.18, was reached. The on-chip dispensing and transport nanoliter-sized droplets on the latest design described above are shown in Figure 3.19. At a gap height of 100 μm, the volume of each dispensed droplet was $\sim$50 nL. Droplets were dispensed at droplet generation rates of up to 2 Hz and transported at switching frequencies of up to 32 Hz. The actuation voltages were at most 240 V.
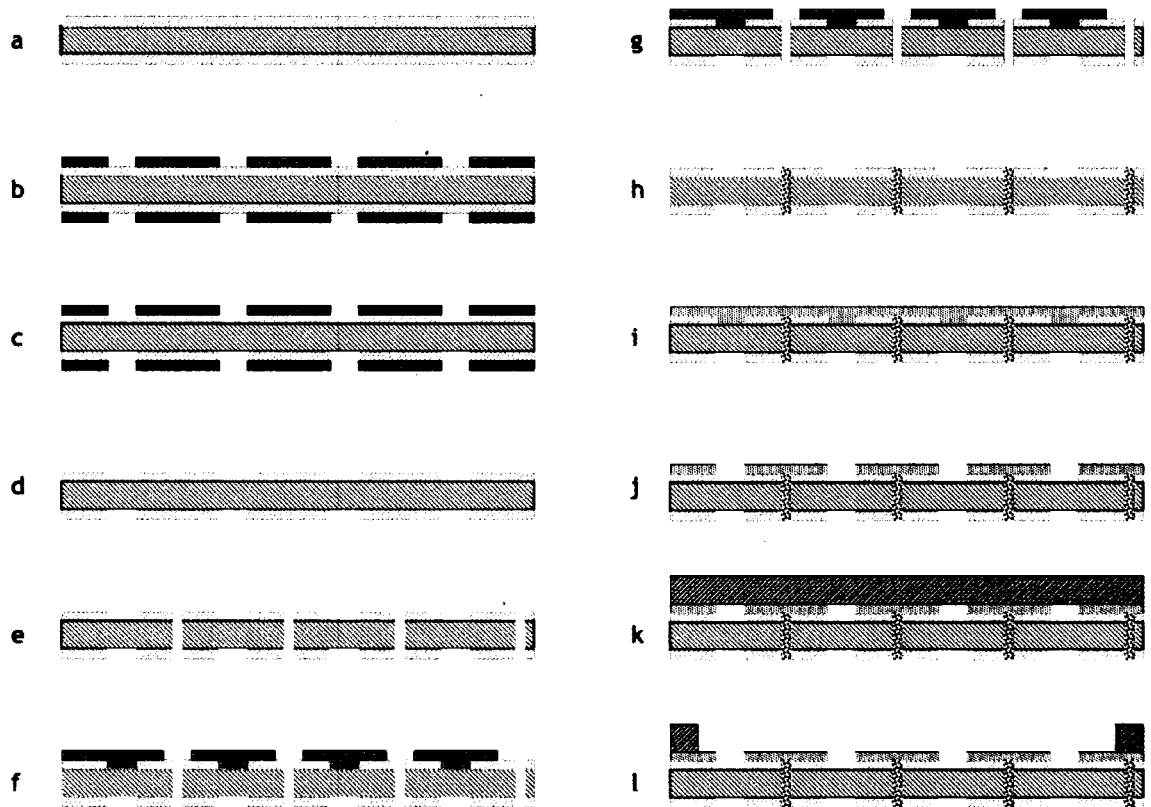
Figure 3.18: Buildup process of the initial PCB digital microfluidic chip prototype. A 32-mil thick PCB board with a 5-mil laminate of copper on both sides was used as the starting substrate (a). Both the top and bottom sides were patterned using a photomask (b, c), then etch-off processes (d), and via holes where electrical contacts were to be placed were mechanically drilled (e). A mask was made such that only the via holes were exposed (f). The copper was then plated to build up the copper in the via hole (g). This technique of only building up the copper surrounding the via is called button plating. The holes were then plugged with an insulator (h). LPI soldermask was applied next to the top side of the board (i), and patterned to expose the ground rails (j). A 4-mil thick layer of dry solder mask was laminated on (k) and subsequently patterned to reveal the gasket (l) defining both the spacing of the fluid layer and the reservoirs. The final final thickness of the copper was $\sim25\mu$m. The spacing between each electrode was $\sim$3-4 mils. The thickness of the soldermask was $\sim17\mu$m, or 0.7 mils.
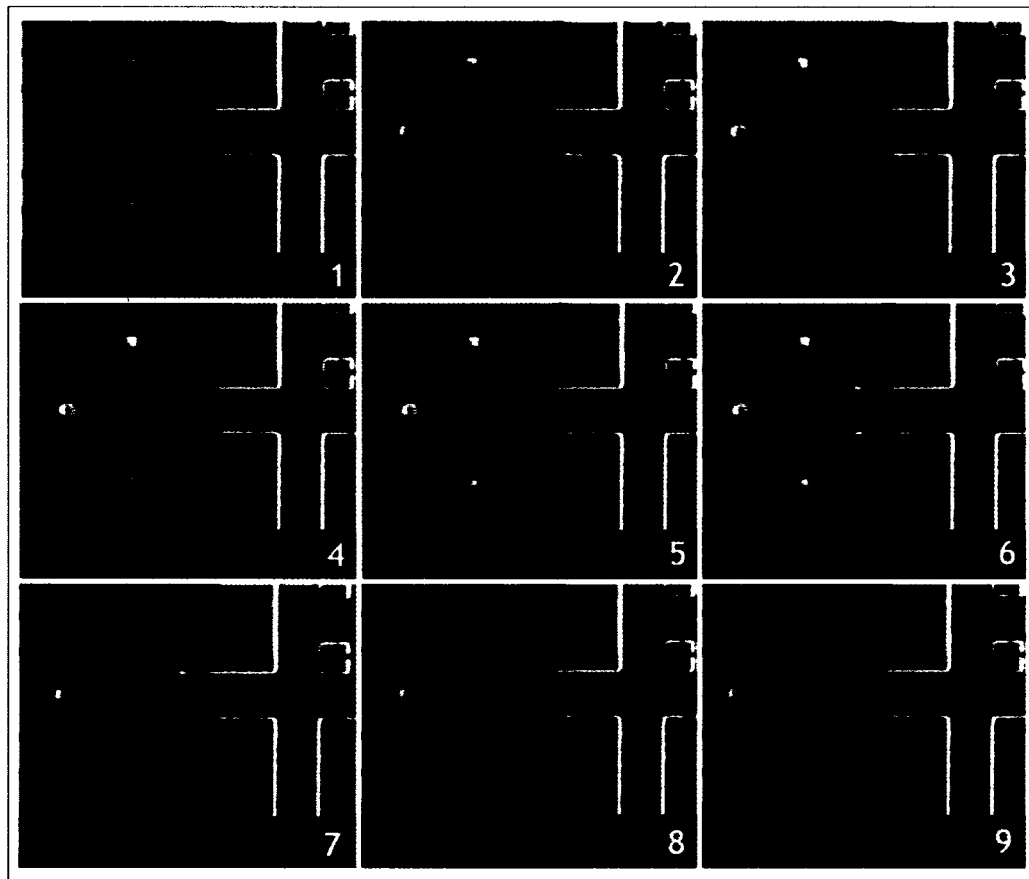
Figure 3.19: Time-lapsed images of on-chip dispensing and transport of 50 nL droplets on a PCB microfluidic chip.

3.5 Chapter Summary and Conclusions

Since much of the research performed in digital microfluidic has been targeted toward biological and chemical applications, it was necessary for us to develop several new strategies to enable our study of droplet-based hot-spot cooling in this platform. This included finding methods for temperature measurement, simulating hot-spots, and fabrication methods alternative to expensive vacuum processes. In the following chapters, we implement these strategies to obtain experimental results that establish the viability of digital microfluidics as an advanced cooling platform.

Chapter 4

Experimental Results - Thermal Effects on Droplet Transport

To characterize a droplet-based cooling architecture using digital microfluidics, we must first understand the mobility of droplets at elevated temperatures. In this chapter, we investigate the thermal effects on droplet transport by specifying minimum energies required to move a droplet at a given temperature, for droplets moving in both oil and in air. In order to understand these thermal effects affecting droplet transport in oil, we present the temperature-dependency of two system parameters, interfacial tension and oil viscosity. For droplets moving in air, we investigate the temperature-dependency of the contact angle between the liquid droplet and the solid electrowetting chip.

4.1   Experimental Methods

A number of parameters were varied to investigate the thermal effects on droplet transport. These parameters include system temperature, interfacial tension, oil viscosities, contact angles, and actuation voltages. For temperature-controlled experiments, heaters were provided off the chip using an ITO-coated glass slide affixed to the bottom of the chip, as shown in Figure 4.1. A thermocouple-based PID controller was used to ensure that the chip, droplet, and surrounding silicone oil (if used) were maintained at the desired temperatures.

A custom electronic controller was made to independently address and provide high voltage to each electrode. The controller consisted of a logic unit which decoded an input address to a bank of flip-flips which then drove a parallel bank of transistor switches. The transistors were rated for +/- 400V and 1.3A (AQW614EH, DigiKey). The controller was
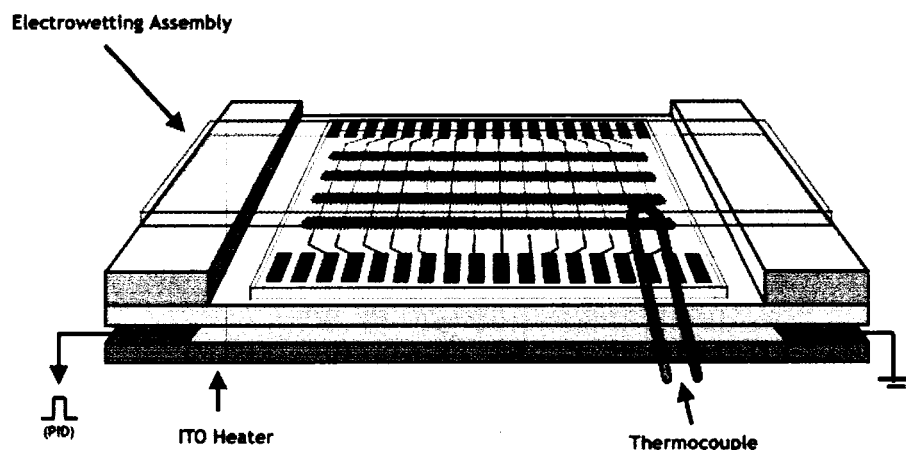
Figure 4.1: Experimental setup to raise the system-wide temperature for droplet transport studies.

connected to the parallel port of a PC and was operated using custom-written software to easily toggle each electrode using the keyboard. The software was also made programmable, so that a user can execute a pre-defined sequence of toggles, each at a specified length of time, making the mixing process completely automated.

4.1.1 Investigation of In-Oil Parameters

The surface tensions of the liquid droplets were modified using a non-ionic surfactant (Triton-X 100). Since silicone oil is used to surround the droplets, values were measured as the interfacial tension with silicone oil using a surface tensiometer (Fisher Tensiomat Model 21). Each measurement was made by resting a platinum-iridium ring between the interface of silicone oil and the desired liquid. The tensiometer was zeroed, and an upward force was slowly applied until the ring broke through the surface of the oil, at which point the surface tension value was obtained. Silicone oil with a viscosity of 1 cSt was used for all initial experiments. However, the viscosity temperature coefficient (v.t.c.) [1] of 0.37 suggested that viscosity changes with temperature were significant in the ranges studied

---

[1] v.t.c = 1 - (viscosity @ 99° C/viscosity @ 38° C)

(10°C to 100°C). Thus, additional viscosities of 0.65, 2, 5, and 10 cSt were obtained to study the effects of viscosity only on droplet transport. Experiments were visually observed using a CCD microscope and recorded digitally for further analysis.

4.1.2 Investigation of In-Air Parameters

The contact angle of the droplets at the liquid-solid interface for experiments performed in air were measured visually. A CCD microscope was used to obtain the profile of the droplet, and the contact angles were measured using the "Half-Angle" method (Tantec, Inc. IL). By drawing a line through the apex of the droplet from the interface point between the liquid/solid surfaces, the contact angle was measured with good repeatability (+/- 0.1 degrees).

4.2 Experimental Results for a System in Oil

4.2.1 Global Temperature Effects on V_{th} in Oil

Successful transport of a droplet in a digital microfluidic chip is contingent upon a number of parameters, including actuation voltage, droplet dimension, and in systems with a filler fluid present, the filler fluid viscosity and droplet-oil interfacial tension among others. While the impact of these parameters on droplet transport has been established in experiments performed at room temperature [13, 15, 34, 35, 36], their effects at higher temperatures have not yet been studied in detail. To determine the viability of our platform for chip-cooling, the effect of temperature on minimum actuation voltages, interfacial tension, and oil viscosities must be carefully studied.

Threshold voltages (V_{th}), defined as the minimum voltage required to oscillate a droplet among a set of electrodes at a specific switching frequency, were determined at various system-global temperatures. The off-chip heater was used to raise the temperature of the

entire system uniformly to 75°C, during which period droplets were oscillated among four electrodes using 4, 8, and 16 Hz switching frequencies.
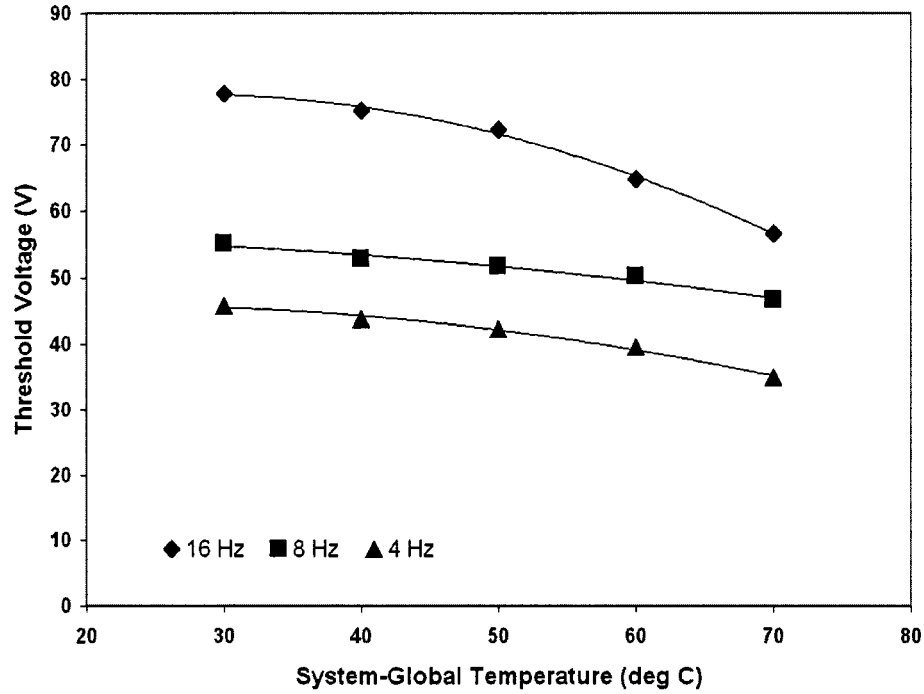
Figure 4.2: Temperature effects on threshold voltage, V_{th}. 1.5 mm square electrodes and a 600m gap was used. The volume of each droplet was 1.4 μl.

We observed up to a 30% decrease in V_{th} for a 50°C temperature increase, as shown in Figure 4.2. As much as a 17V reduction in actuation voltage was observed. Since linear droplet velocity increases with voltage, these results suggest that droplet velocity increases as temperature increases for a given voltage. This inherent increase of the droplet flow rate at higher temperatures makes this system an attractive approach for smart active cooling, since hotter regions on an IC would experience faster cooling rates.

In order to identify the mechanism by which droplet transport is facilitated at higher temperatures, two temperature-dependent parameters were investigated: interfacial tension and oil viscosity.

4.2.2 Interfacial Tension Effects on V_{th}

Since electrowetting is a phenomenon whereby the surface tension of the droplet with a surface is modulated, it is important to study the effects of temperature on this parameter. However, since there is evidence to suggest the presence of a thin oil film between the droplet and the solid surface in our system [37], a more relevant parameter to investigate is the interfacial tension of the droplet with the surrounding oil. Interfacial tension measurements between the droplet liquid and 1 cSt oil at various temperatures are shown in Figure 4.3.
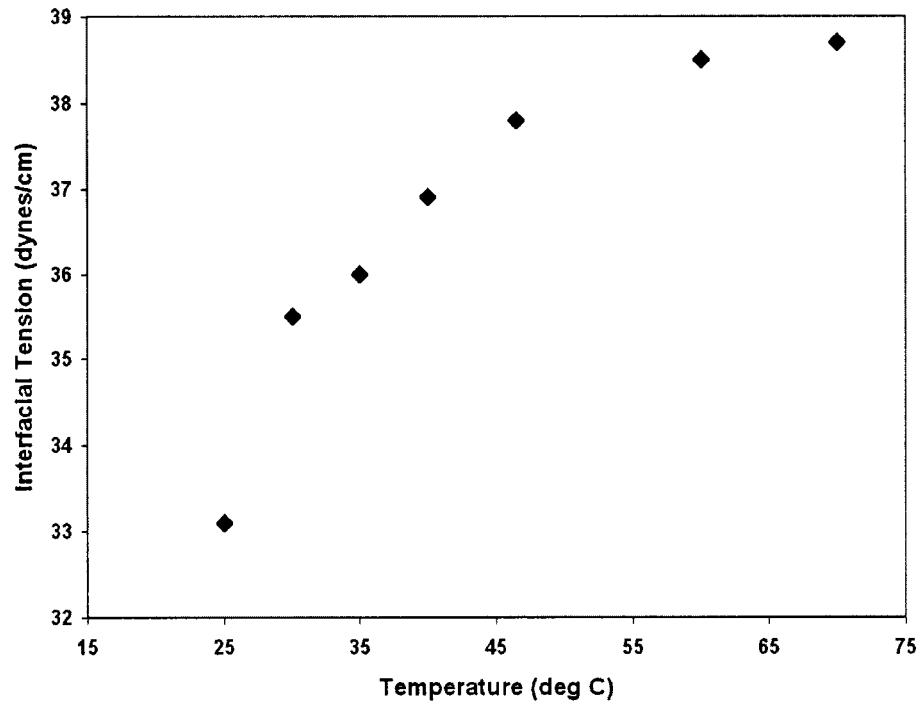
Figure 4.3: Variation in the oil-water interfacial tension for a 1 cSt silicone oil and de-ionized water at various temperatures.

Over a 50°C temperature range, we observed a 14% (5.7 dyne/cm) increase in interfacial tension, which appears to asymptote near 75°C. This behavior suggests that at higher temperatures, interfacial tension alone no longer has a significant impact on the threshold

72

voltage reductions shown in Figure 2, which exhibit a linear decrease past 60°C. We verified this behavior by exploring the threshold voltage dependency on interfacial tension in the absence of temperature variation, as shown in Figure 4.4.
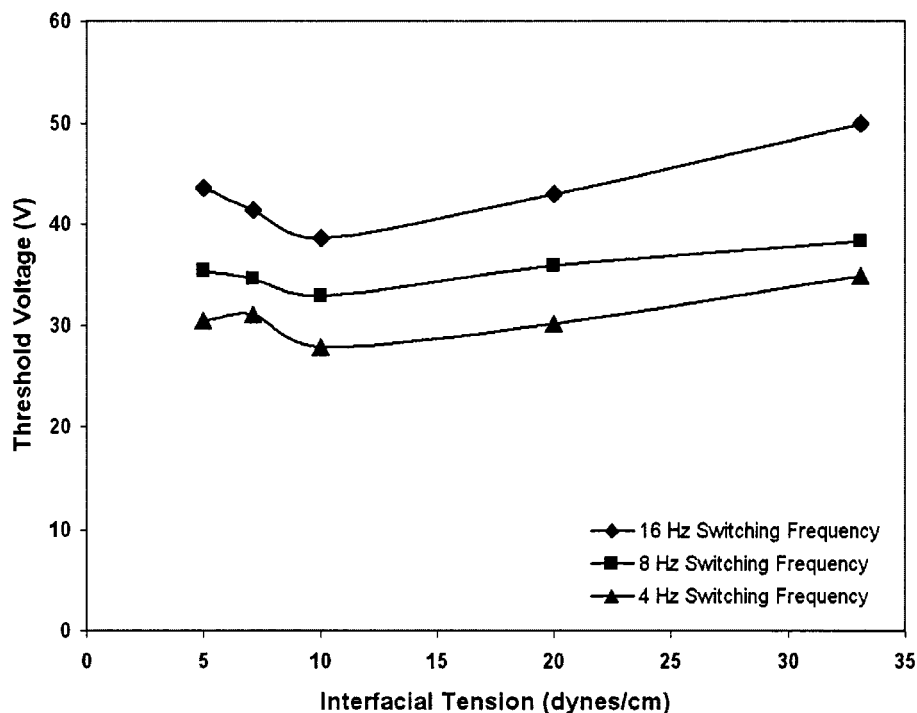
Figure 4.4: Threshold voltage (V_{th}) dependency on Interfacial tension @ 25C. Note: Because it is impossible to chemically increase the surface tension of de-ionized water, the interfacial tension values beyond 33.1 dynes/cm (0% Triton-X) were unobtainable. Data–fitting curves are included for visualization purposes only.

Various concentrations of Triton-X were added to water to reduce its interfacial tension, and V_{th} was obtained at each concentration for 4, 8 and 16 Hz switching frequencies. The results from Figure 4 suggest that there exists an optimal interfacial tension near 10 dynes/cm for transport. Below this value, the droplet deforms due to lower surface tension such that the leading edge of the droplet responds faster in moving towards to an activated electrode compared to the lagging edge. Therefore, these droplets need larger threshold voltages to transport. Typically, we observe a discrete motion of a droplet at higher surface tensions. Above 10 dynes/cm, however, the threshold voltage response is nearly linear,

with, at most, a slope of +0.5V per every dyne/cm. This suggests that, over the interfacial tension ranges observed in Figure 4, the temperature-induced interfacial tension effect on V_{th} accounts for only a 2.85V increase. Thus, while interfacial tension may partially reduce the speed of droplet at higher temperatures, other mechanisms are at play, which we investigate next.

4.2.3 Oil Viscosity Effects on V_{th}

The viscosity of the surrounding silicone oil plays a significant role in droplet transport. It has been previously reported that V_{th} increases with increasing viscosities of the oil and the droplet [17]. The viscosity temperature coefficient (v.t.c.) of 0.37 for 1 cSt silicone oil suggests that there exist significant reductions in oil viscosity at elevated temperatures. Assuming linearity, the calculated viscosity of nominally 1 cSt silicone oil is 0.71 cSt at 70°C.

Threshold voltages were obtained for 4, 8, and 16 Hz switching frequencies for 0.65 cSt silicone oil at 25°C, and compared to values obtained using 1 cSt oil at both 25°C and 70°C. Values were normalized to 1 cSt oil at room temperature, as shown in Figure 4.5.

We observe that the threshold voltage reductions for both 1.0 cSt at 70°C and 0.65 cSt at room temperature are similar. The largest voltage drop was observed for droplets oscillating at 16 Hz in 0.65 cSt oil, with a value of 17.6V. This is consistent with the 17V drop shown in Figure 4.2, suggesting that oil viscosity is the primary mechanism in facilitating droplet transport at higher temperatures.

4.3 Experimental Results for a System in Air

We have thus far observed that the reduction of viscosity in the silicone oil surrounding a droplet accounts for its reduction in threshold voltage at higher temperatures. In order to verify this assumption, we must now look into the thermal effects of droplets transported
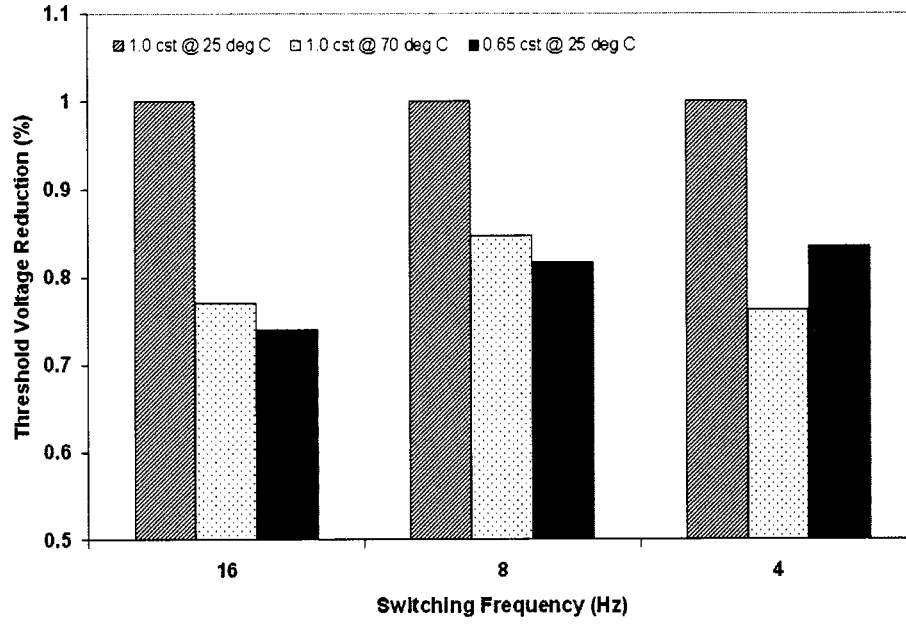
Figure 4.5: Percent reductions in threshold voltages (V_{th}) for droplet transport in 0.65 cSt oil at 25°C and 1.0 cSt oil at 75°C, as compared to values obtained in 1.0 cSt oil at 25°C.

in air.

4.3.1 System-Global Effects

The effect of temperature on minimum actuation voltages of droplets transported in air were studied. The off-chip heater was used to raise the temperature of the entire system uniformly to 45°C, during which period droplets were oscillated among four electrodes at 16 Hz switching frequencies. Experiments were limited to a maximum temperature 45°C due to the accelerated evaporation of the droplets at higher temperatures.

As shown in Figure 4.6, the required actuation voltages for droplets in air were much higher for a droplet transported at 16 Hz. We observe up to a 28% increase in V_{th} for a 20°C temperature increase, or a 19V increase in actuation voltage. This trend is opposite to that shown in Figure 4.3, suggesting that the presence of oil is the sole mechanism for which droplet transport is improved for an in-oil system. We thus examine the temperature
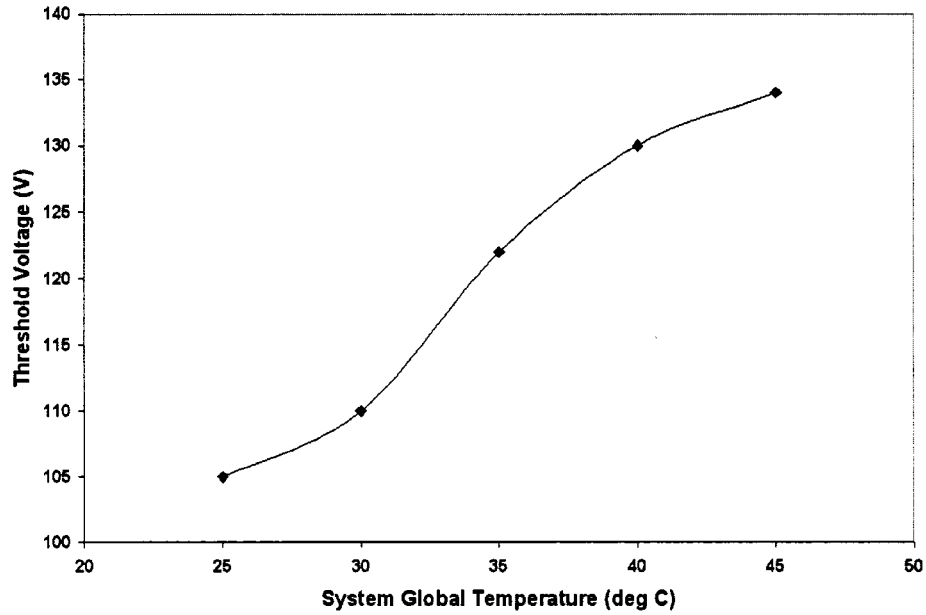
Figure 4.6: Temperature effects on threshold voltage, V_{th}. 1.5 mm square electrodes and a 600m gap was used. The volume of each droplet was 1.4 μL, and the switching frequency was 16 Hz.

effects of the contact angle between a water droplet and the teflon surface.

4.3.2 Contact-Angle Temperature Dependence

The transport of droplets is achieved by modulating the contact angle of the receding and advancing ends of the droplet. By increasing the voltage of the actuating electrode, we increase the electric fields, which induces a reduction in contact angle, thus creating a gradient within droplet. This gradient propels the droplet toward its advancing line, until it disappears when the droplet is centered onto the actuating electrode. The velocity of the droplet is proportional to this gradient, and thus is proportional to the voltage applied to the electrode.

At room temperature, the contact angle of a droplet on a teflon surface is 110°. The effects of temperature on this value were unknown and thus studied. Using the off-chip heater and directly imaging the profile of the droplet, we were able to obtain the temper-

76

ature dependence of the water-teflon contact angle. A secondary droplet was positioned nearby and used as a temperature reference by placing a thermocouple inside of it. The results are shown in Figure 4.7.
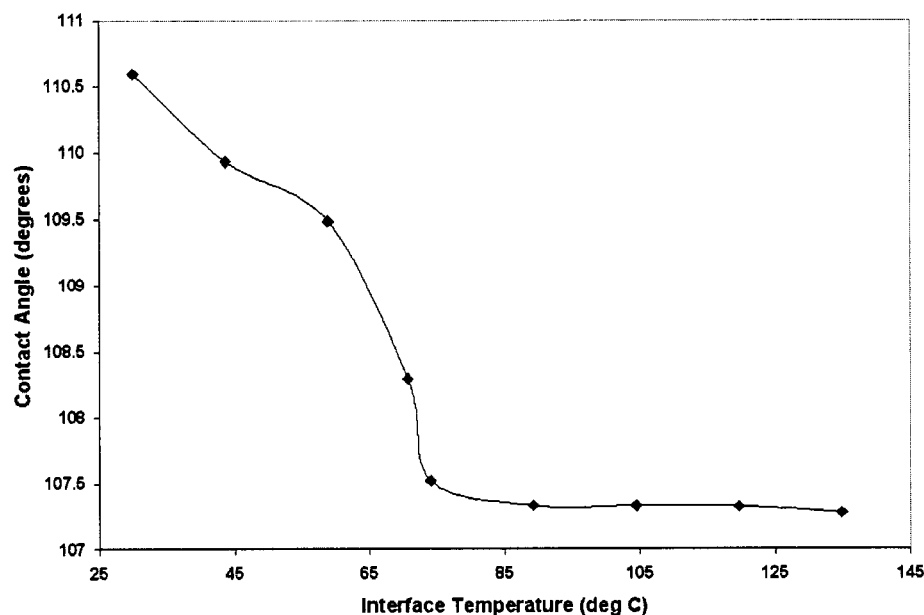
Figure 4.7: Temperature dependence of the contact angle between water and teflon.

We observe a steady decrease in contact angle as temperature is increased up to 75°C. The change abruptly plateaus beyond this temperature, at which point the droplet approaches its maximum boiling point temperature of 100°C. It is unclear whether this transition point is indeed at 75°C as the actual temperature of the droplet-surface interface could not be obtained with a thermocouple. The results shown in Figure 4.7 suggest that the decrease in nominal contact angle with increasing temperature diminishes the gradient that drives the droplet's motion, as the contact angle of the receding line is now reduced. One may also interpret these results to say that the surface has effectively become more hydrophilic as a result of the higher surface temperature, thus rendering transport of droplets more difficult.

We can hence draw a relationship between the threshold voltage and the droplet's nom-
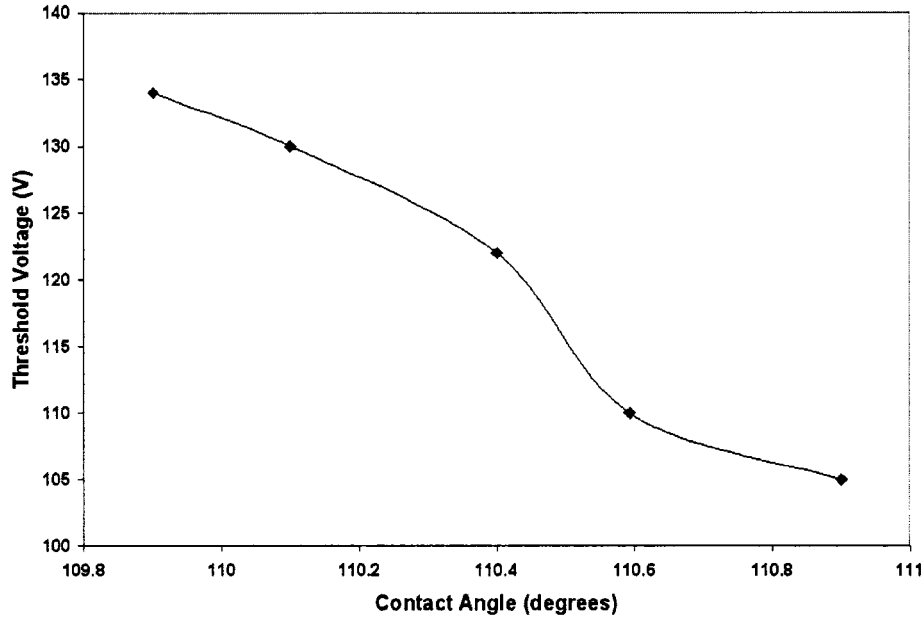
Figure 4.8: Temperature dependence of the contact angle between water and teflon.

inal contact angle. As shown in Figure 4.8, we observe a fairly linear decrease in threshold voltage as the droplet's nominal contact angle is increased. This is consistent with our observations that droplets transported on surfaces of less hydrophobicity (hence lower nominal contact angles) require higher threshold voltage, thus contributing to the trend seen in Figure 4.6. These effects are transparent for a droplet in oil, as the notion of a contact angle does not exist since it has been suggested that a thin layer of oil separates the droplet from the surface [38]. Thus, these negative thermal effects on droplet transport are not felt for an in-oil system.

4.4 Chapter Summary and Conclusions

In this chapter, we studied the thermal effects on droplet transport in a digital microfluidic platform. A significant drop in minimum threshold voltages (V_{th}) required for the oscillation of microdroplets was observed at elevated temperatures, which, given a constant

actuation voltage, is synonymous to increased droplet velocities. This increased flow at higher temperature makes this platform ideal for active and smart chip-cooling applications. Interfacial tension and oil viscosities were investigated as possible mechanisms for this behavior. The reduction of interfacial tension alone with elevated temperatures plays a minor role in the reduction of V_{th}, while the lowered viscosity of the surrounding oil accounts for nearly all the changes observed. Hence, the surrounding temperature-dependent silicone oil plays a significant role in enabling the "adaptive" aspect of chip cooling without the need for external sensors.

Chapter 5

Experimental Results: Flow-through Based Adaptive Cooling

In this chapter, we design, fabricate and test a PCB-based digital microfluidic cooling architecture that enables droplets to be dispensed, transported, and recycled in a closed-loop fashion in order to cool a heated substrate. We also demonstrate for the first time the ability to program droplets to cool hot spots in both an open (a droplet unconfined by a top plate) and closed (a droplet confined by a top plate) system using the coplanar electrowetting method described in Chapter 3. Parameters such as droplet aspect ratios, heat densities, droplet liquid media and filler fluid media within these systems are studied for their heat transfer characteristics.

5.1 Experimental Methods

5.1.1 Digital Microfluidic Platform Development

While the initial prototype of PCB-based digital microfluidic chips demonstrated the feasibility of using rapid-prototype fabrication process for droplet transport, a number of design iterations were necessary to reach a stable platform that would enable the repeated dispensing, transport, and recycling of droplets required for a flow-through adaptive cooling device. Many of the successful changes relied heavily on fabrication parameters such as starting substrates, via hole filling and plating methods, and surface finishing. Many of the parameters on the design side were kept close to a baseline design that proven to work on glass-based digital microfluidic chips. The following sections describe and discuss the importance of each of these parameters.

80

PCB Substrate Starting Material (Fabrication Parameter)

The starting material used in PCB processes has a large influence over the final characteristics of the board. For example, the thickness of the initial copper laminate dictates the resolution of the smallest features sizes since patterning of the copper is a subtractive process (hence a thicker laminate would require more etching resulting in larger minimum spacings). The minimum thickness available to us was 5 μm, however thinner laminates could be theoretically be deposited.

Another variable is the substrate thickness. Initial prototypes were built on 16 mil thick boards, thin enough for the boards to be flexible. Thicker boards provide greater stability, however some fabrication steps, such as the filling of via holes using LPI soldermask, would have to be modified to account for the larger volume in each via that must be filled.

Via Hole Filling and Plating (Fabrication Parameter)

The resulting via holes necessary to create electrical contact between the the top and bottom metal layers of the PCB can hinder droplet transport if they are not filled. Droplets which would transport over these empty vias would get pinned to the holes as capillary forces would draw liquid into the holes. Hence, initial prototypes used the LPI soldermask as a method for filling the via holes. The thickness of the boards (16 mils) was of sufficient thinness for the holes to be completely filled shut. Alternative methods to filling the hole include the use of an insulating or conductive epoxy that is squeegeed onto the board. Once cast, the board must be sanded down to re-expose the copper, yet leaving the via holes plugged. This method imposes additional limitations on the minimum line widths and spaces as thinner lines have a tendency to be opened during the sanding process. This restriction can be avoided if button plating of the vias is performed.

Various hole plating and filling methods are shown in Figure 5.1. Plating of the via holes is necessary in order to make electrical contact between the top and bottom metal

layer of the PCB board. It is traditionally accomplished by electroplating the entire board once the via holes have been drilled. This causes all features on the board to increase in all three dimensions, thus extremely small spaces between copper traces run a risk being shorted together. The result is a restriction placed on the minimum spaces at the time of design.
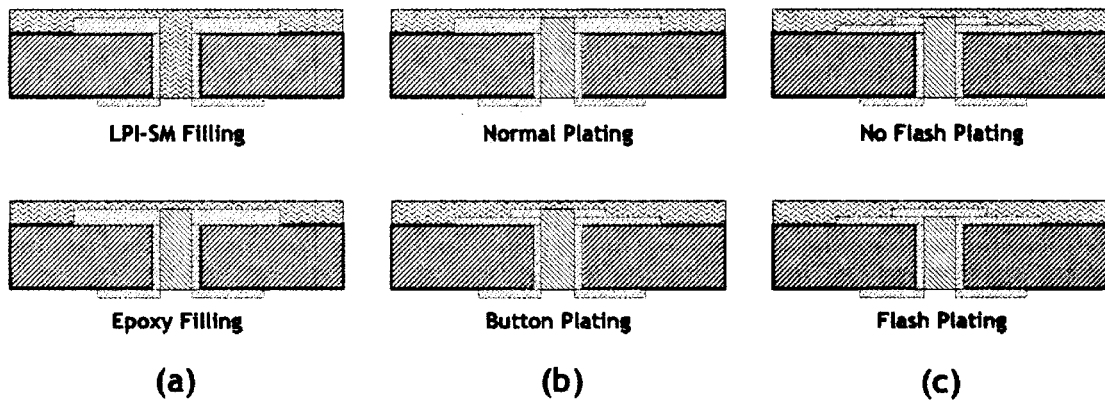
Figure 5.1: Various methods of filling and plating of via holes: (a) Filling using epoxy versus LPI soldermask, (b) button plating versus normal plating, and (c) flash plating versus no flash plating.

An alternative plating process, called button plating, eliminates this restriction as only the immediate area surrounding the via is plated by the addition of a mask. Epoxy filling of the holes is also selectively limited to the via hole and not the entire board, allowing the sanding process to be restricted only to the via area. An additional step, called flash plating, allows the epoxy-filled area of the via hole to be plated with copper. This increases the electrode area, resulting in improved electrowetting.

Surface Finishing (Fabrication Parameter)

While copper is used as the base metal for patterning, a surface finish of a different metal can be electroplated on top. Typical surface finishes include silver, nickel and gold. Surface finishing is recommended in conditions where oxidation of the surface metal must be

minimized.

Transport Electrodes (Design Parameter)

In a coplanar electrowetting system, electrode design must be extended to also consider the placement of grounding contacts, which can be take on a number of forms, such as rails or pads. A droplet should ideally be in continual contact with a ground contact.

Baseline designs include two grounding rails that run parallel to the electrode array. Variables to the grounding rails include the rail widths and the spacing between the electrode and the grounding rail. Initial prototypes employed 1.5 mm pitched square electrodes with grounding rails that were 2 to 4 mils wide which were spaced 2 to 4 mils away from the electrode. Later designs used 750 μm square electrodes with 3 mil grounding rails spaced 2 mils away from the electrode.

Electrode shapes were also modified to allow for grounding rails to protrude into the footprint of the droplet. The protrusion allowed for increased overlap of the droplet with the grounding rails.

On-Chip Reservoir (Design Parameter)

A patternable dry soldermask layer allowed for the placement of liquid reservoirs from which droplets could be dispensed on-chip. While the reservoir shape itself was kept constant throughout all designs, the ground contacts were varied between grounding lines and spots.

5.1.2 Transport of Various Cooling Liquids

Three cooling liquids were explored for the flow-through based adaptive cooling scheme - water, dimethyl sulfoxide (DMSO), and ethylene glycol. Dispensability and transportability was tested by loading each liquid into a reservoir where a droplet is dispensed and

	Water	Ethylene Glycol	DMSO
Chemical Formula	$HOCH_2CH_2OH$	H_20	C_2H_6OS
Melting Point (°C)	-12.9	0	18.5
Boiling Point (°C)	197.3	100	189
Density (g/m^3)	1113	1000	1100
Viscosity (cP)	16	0.89	1.996
Specific Heat (J/kG-K)	3497	4180	1884
Thermal Conductivity (W/m-K)	0.38	0.58	0.2

Table 5.1: Properties of cooling liquids (@ 25°C where applicable).

transported at various switching frequencies. Relevant characteristic properties of each liquid is shown in Table 5.2.1.

5.1.3 Heat Transfer Characterization

Hot-Spot Cooling in an Open System

The first prototype for a PCB-based digital microfluidic chip (PCB-R001) was designed to characterize the cooling efficiency of hot spots using droplets in an open system. As shown in Figure 5.2, the chip consists of linear arrays of nine electrodes. A 1.5 x 1.5 mm^2 thin-film heater, patterned on the backside of the PCB, was aligned with the center electrode. By applying a specified voltage to the heater, a hot-spot on the top side of the PCB was simulated.

The input power to the heater was varied using a constant power supply. A single droplet was oscillated across all nine electrodes at various switching frequencies. The switching frequency denotes the rate at which droplets are transferred across two electrodes, thus it is a measure of effective flow rates. The actuation voltage was fixed at 240V.

Using the infrared camera (JTL1 Infrared Imager, Edmund Optics, Barrington, NJ, USA) discussed in Chapter 3, a thermal profile of both the droplet and the chip was captured. The video was recorded digitally and image-processed using a custom-written MATLAB program (see Appendix A), whereby the temperature of the hot spot was obtained for
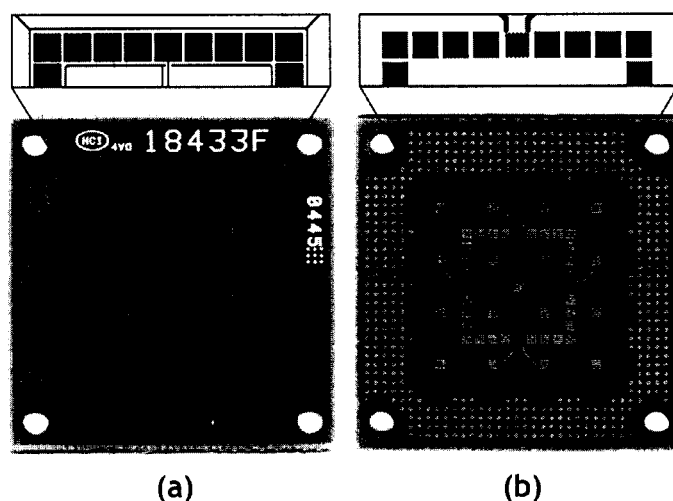
Figure 5.2: Photographs of the PCB chip viewed from the top-side (a) and bottom-side (b). The schematic shows the region where hot spot characterization was performed.

each frame.

Hot-Spot Cooling in a Closed System

Subsequent PCB-based digital microfluidic designs were used to investigate the cooling efficiency of hot-spots using droplets in a closed system. As shown in Figure 5.3, the chip (PCB-R005 TM-01) consists of an array of electrodes. A glass plate consisting of RTDs and heaters complimenting the electrode array was used as the top plate. By applying a voltage to the heater, a hot-spot on the top plate was simulated.

The input power to the heater was varied using a constant current source (CALEX 930 High Power Programmable Current Source, CALEX Mfg. Co., Concord, CA). A 50 nL droplet was dispensed on-chip, then transported across the hot-spot. The cooling liquid used was water, and the surrounding filler fluid was 1.5 cSt silicone oil.

A similar experiment was performed that allowed us to obtain a thermal map of a mock IC chip with a constant power (heat) density. Any heat that was drawn away by moving droplets from this background heat flux could be imaged using the infrared camera. As

Top View   Side View
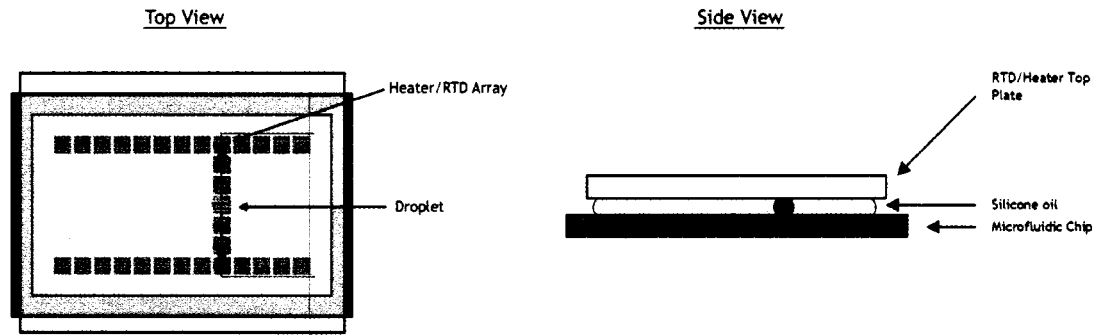
Figure 5.3: Experimental setup for the cooling of a single hot-spot.

shown in Figure 5.4, the microfluidic chip (PCB-R005 TM-01) was assembled with a thin glass top plate (170μm). The reduced thermal resistance of this thin glass plate allowed for heat transfer across this region to be quick, and minimized the spread of heat in the lateral direction, allowing an accurate "footprint" of the thermal profile of the top plate to be obtained.

Top View   Side View
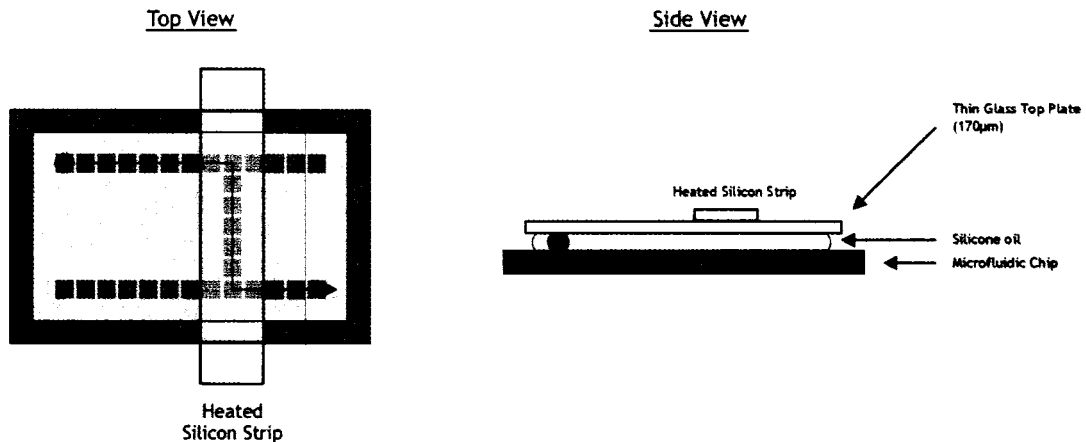
Figure 5.4: Experimental setup for the cooling of a constant background heat density.

A silicon strip heater was created by dicing a silicon wafer and affixing standard 1/4 watt resistors attached to both ends of the strip. The high thermal conductivity of the silicon material allowed for a uniform heat flux to be dissipated.

86

An infrared video was obtained by looking at the top view of the system. Since silicon is transparent in the IR range, we were able to observe any heat transfer on the underlying glass top plate that was taking place. The cooling liquid used was water, and the surrounding filler fluid was 1.5 cSt silicone oil. The droplet was transported across the path as shown from the top view.

Static Heat Transfer Characterization

Static heat transfer experiments were performed to obtain time constants for the cooling of hot-spots using droplets. Two RTD/heater plates were aligned with each other in order create a top and bottom plate, as shown in Figure 5.5. Each plate was insulated with 2 μm Parylene C, and brush coated with 1% Teflon AF.
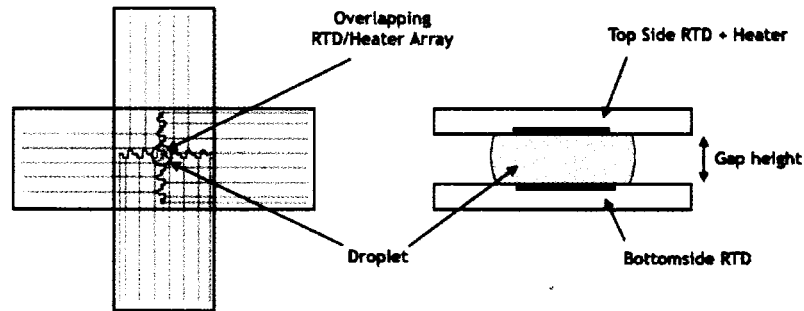
Figure 5.5: Experimental setup for static heat transfer characterization.

A droplet was placed between the two plates and aligned such that a pair of RTDs was in contact with the top and bottom sides of the droplet. The gap was filled with 1.5 cSt silicone oil, and the temperature of both RTDs were recorded as a heater from one side was turned on at a fixed power.

Specification	Units	Requested	Measured
Board Thickness	mil	16	16
Initial Copper Thickness	μm	5	-
Final Copper Thickness	μm	25	37
LPI Soldermask Thickness	mil	0.5	0.7
Dry Film Soldermask Thickness	mil	-	-
Electrode Pitch	mm	1.5	1.5
Electrode Spacing	mil	2 to 3	3 to 4.5
Via Filling	-	LPI	LPI
Flash Plating?	-	No	No
Button Plating?	-	No	No
Surface Finish	-	None	None

Table 5.2: Requested and measured specifications from the fabrication of the initial PCB-based digital microfluidic chip prototype.

5.2 Digital Microfluidic PCB Platform Development

5.2.1 Fabrication Parameters

The initial prototype for a PCB-based digital microfluidic chip was based on a 2 mil process (minimum line spacing) as described in Chapter 3. Table 5.2.1 shows a list of fabrication specifications and actual measured specs from this initial prototype run.

(a)   (b)
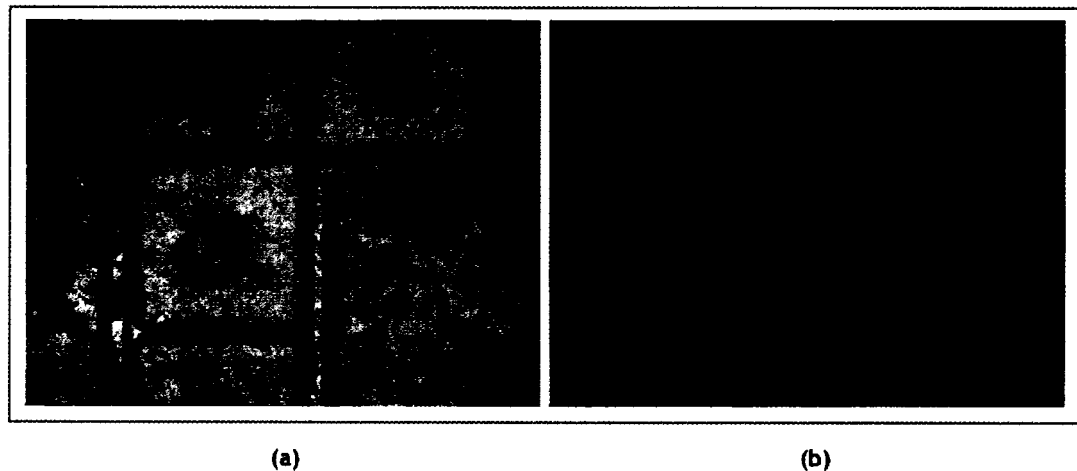
Figure 5.6: Breakdown caused by insufficient insulator coverage as viewed (a) normally and (b) through fluorescence microscopy.

Despite the larger electrode spacings, droplet transport at these scales still worked. However, problems were encountered due to insulator breakdown which typically occurred at the edges of electrodes. Since the squeegee process of LPI soldermask is not a conformal coating, the step heights due to the large copper thickness may have caused improper coverage of the electrodes. Breakdown at these locations were typically noticed upon initial use of a chip (see Figure 5.6).

The second iteration of PCB-based digital microfluidic chips was similar to the first, except that the application of LPI soldermask failed to fill the via holes within the electrode. As a result, the via would act as a capillary into which the droplets would get stuck, as seen in Figure 5.7.

<div align="center">(a)   (b)</div>
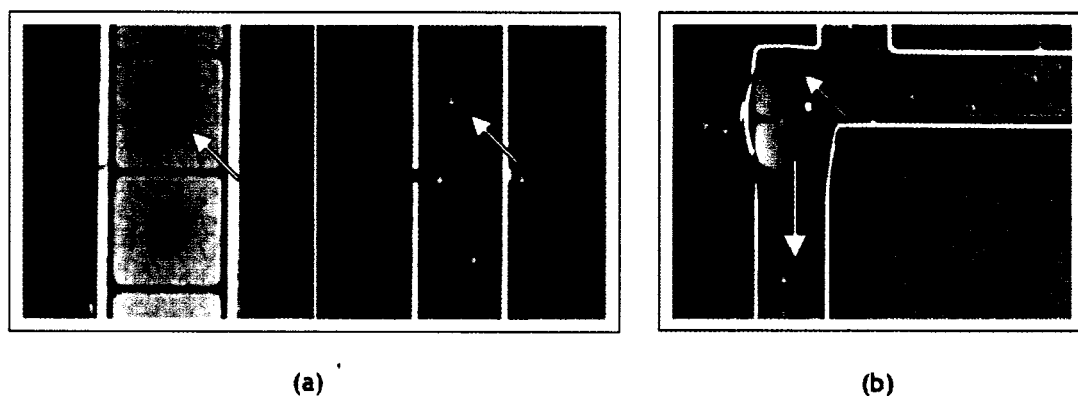
Figure 5.7: (a) Images of digital microfluidic chips with LPI soldermask-filled (left) and unfilled (right) vias. (b) The pinning of a droplet attempting to transport down the electrode array.

The third iteration of PCB-based digital microfluidic chips had a number of design changes from the initial designs. As shown in Table 5.2.1, the PCB substrate thickness was increased to add rigidity to the chips, the via holes were epoxy filled and button plated, and a dry soldermask layer was added to serve as the gasket.

Since there was no surface finish added in this iteration, the exposed copper from the electrical contacts and the ground lines were heavily oxidized upon receipt, causing in-

Specification	Units	Requested	Measured
Board Thickness	mil	64	64
Initial Copper Thickness	μm	5	-
Final Copper Thickness	μm	25	25
LPI Soldermask Thickness	mil	0.5	1.0
Dry Film Soldermask Thickness	mil	4	4
Electrode Pitch	mm	0.75	0.75
Electrode Spacing	mil	2	3 to 3.5
Via Filling	-	Epoxy	Epoxy
Flash Plating?	-	No	No
Button Plating?	-	Yes	Yes
Surface Finish	-	None	None

Table 5.3: Requested and measured specifications from the fabrication of the third PCB-based digital microfluidic chip prototype.

sufficient contact with the control pads and improper grounding to the droplet. The oxide therefore had to be stripped using a weak acid before use. The use of dry soldermask as a gasket layer served well in defining the reservoirs. On-chip dispensing was successfully demonstrated for the first on PCB using this design.

A stable working platform was reached with the fifth iteration of PCB-based digital microfluidic chips. In addition to the changes made in the third iteration, a surface finish was added to mitigate the oxidation effects of the ground lines and control pads, and the via holes were flash plated over, thus increasing the electrode area. These changes are listed in Table 5.2.1.

5.2.2 Design Parameters

Many of the design parameters were kept constant throughout the various iterations of the PCB-based digital microfluidic prototypes. For example, transport of droplets over electrodes typically worked as long as the ground rails running along side either side of the droplet were designed close to the electrode and was free of any oxidation. Thus, this ground rail scheme, implemented since the initial prototype, has remained virtually unchanged.

Specification	Units	Requested	Measured
Board Thickness	mil	64	64
Initial Copper Thickness	μm	5	-
Final Copper Thickness	μm	25	25
LPI Soldermask Thickness	mil	0.5	1.0
Dry Film Soldermask Thickness	mil	4	4
Electrode Pitch	mm	0.75	0.75
Electrode Spacing	mil	2	3 to 3.5
Via Filling	-	Epoxy	Epoxy
Flash Plating?	-	Yes	Yes
Button Plating?	-	Yes	Yes
Surface Finish	-	Gold	Gold

Table 5.4: Requested and measured specifications from the fabrication of the fifth PCB-based digital microfluidic chip prototype.

Several changes were made, however, to the on-chip dispenser and associated reservoir design. While the shape of the reservoir has remained unchanged, several grounding schemes were designed and tested, shown in Figure 5.8. Due to the large thickness of the LPI soldermask insulator (which was ~20% of the droplet height), exposing any ground contacts resulted in the loss of planarity within the reservoir. Areas where copper was exposed for grounding purposes had a tendency to create pits which disrupted the electrowetting behavior of droplets.
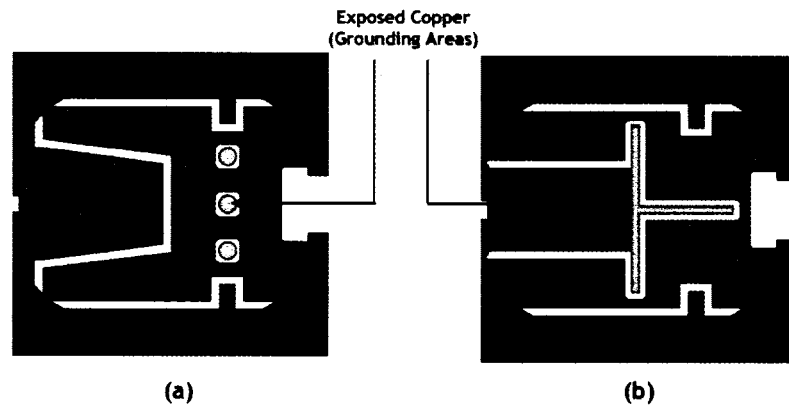
Figure 5.8: Variations on reservoir design using either grounding spots (a) or grounding rails (b).

In the case of cross-shaped grounding rails, liquid in the reservoir would have difficulty coming into contact with the exposed copper due to the resulting trench. The problem was addressed by replacing the cross-shaped ground rail with grounding spots strategically placed such that liquid in the reservoir would always be in contact with at least one of them.

Another key design change resulted from the testing of on-chip co-planar dispensing and transport of droplets. The size of droplets that were formed on-chip was determined by the size of the dispensing electrode. In a bi-planar configuration, this poses no problem as the droplet would adequately cover adjacent electrodes and ground potential would be provided through the top plate. In a co-planar arrangement, however, droplets would require a footprint that was sufficient in size to cover the adjacent grounding rails as well (see Figure 5.9). Since the dispensing electrode was equal in size to the transport electrodes, this requirement was not met.

(a)   **(b)**
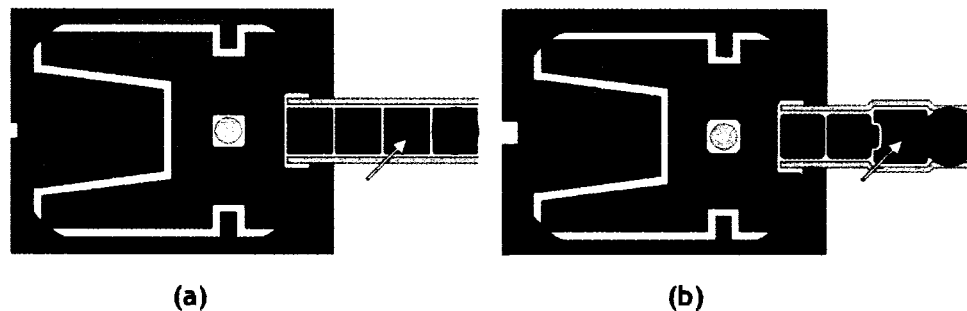
Figure 5.9: Two dispensing designs with (a) a dispensing electrode (shown by the arrow) similar to the transport electrodes and (b) a dispensing electrode slightly larger than the transport electrodes. Only the dispensed droplet in (b) is of sufficient size to overlap the grounding rails on the transport electrode.

Two design changes were made to address this issue. First, the dispensing electrode was made slightly larger than the transport electrode. Second, the electrode shape was changed from a square design to a octagonal or circular design, as shown in Figure 5.10. The resulting inter-electrode spacing would provide more area closer to the center line of

the electrode array, allowing the grounding rails to protrude slightly inward to the array. Hence, dispensed droplets would therefore result in footprints large enough to maintain continual ground contact.
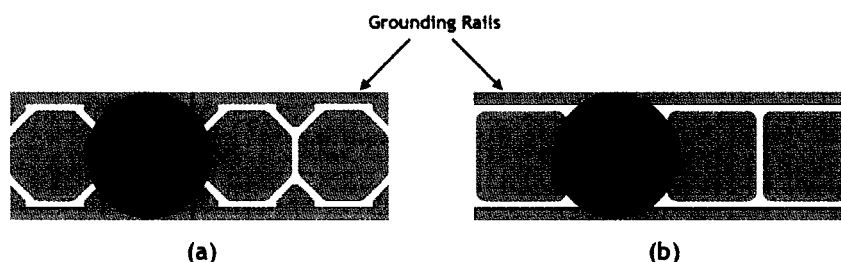
Figure 5.10: Variation on transport electrode shapes: (a) octagonal electrode design versus (b) square electrode design. Note the protrusion of the ground lines into the linear array and its increased overlap with the droplet.

5.2.3 Closed-Loop Dispensing, Transport, and Recycling of Droplets

The successful development a stable PCB-based digital microfluidic platform enabled us to design a system where by droplets could be simultaneously dispensed and transported in a continuous closed-loop fashion, as shown in Figure 5.11). Using a two-dimensional array of electrodes connected to eight reservoirs, up to eight droplets could be simultaneously generated and transported in flow paths such that the net volume of each reservoir was maintained constant.

A number of closed-loop programs are possible for a 7 × 7 array of electrodes (see Appendix D). For maximum heat transfer at a given hot-spot, the largest number of droplets should be delivered to that location. In the case of an eight reservoir design, eight droplets can be dispensed and transported toward the hot-spot.

Figure 5.12 is a time-lapsed sequence of images demonstrating the simultaneous dispensing of four droplets into the 7 × 7 array. The total number of steps for each cycle is 18, during which each reservoir dispenses one droplet and receives one droplet, resulting
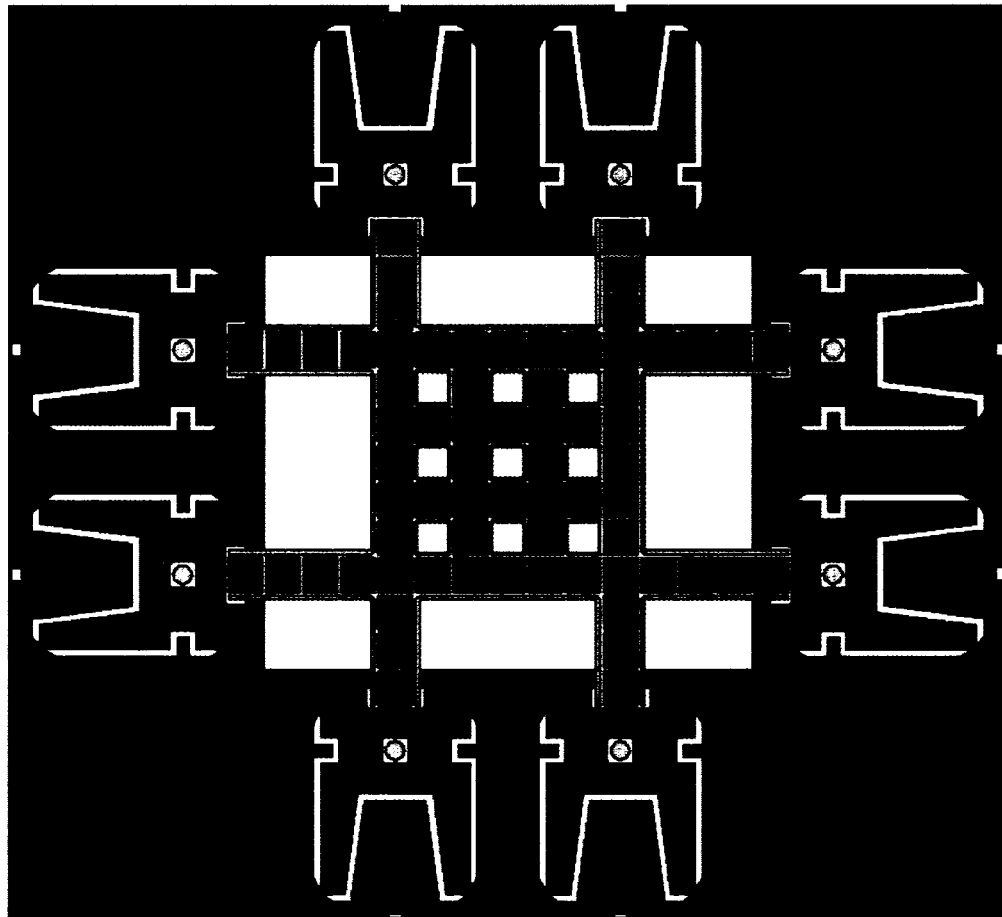
Figure 5.11: Final design of the PCB-based digital microfluidic chip used to demonstrated closed-loop dispensing, transport, and recycling of droplets.
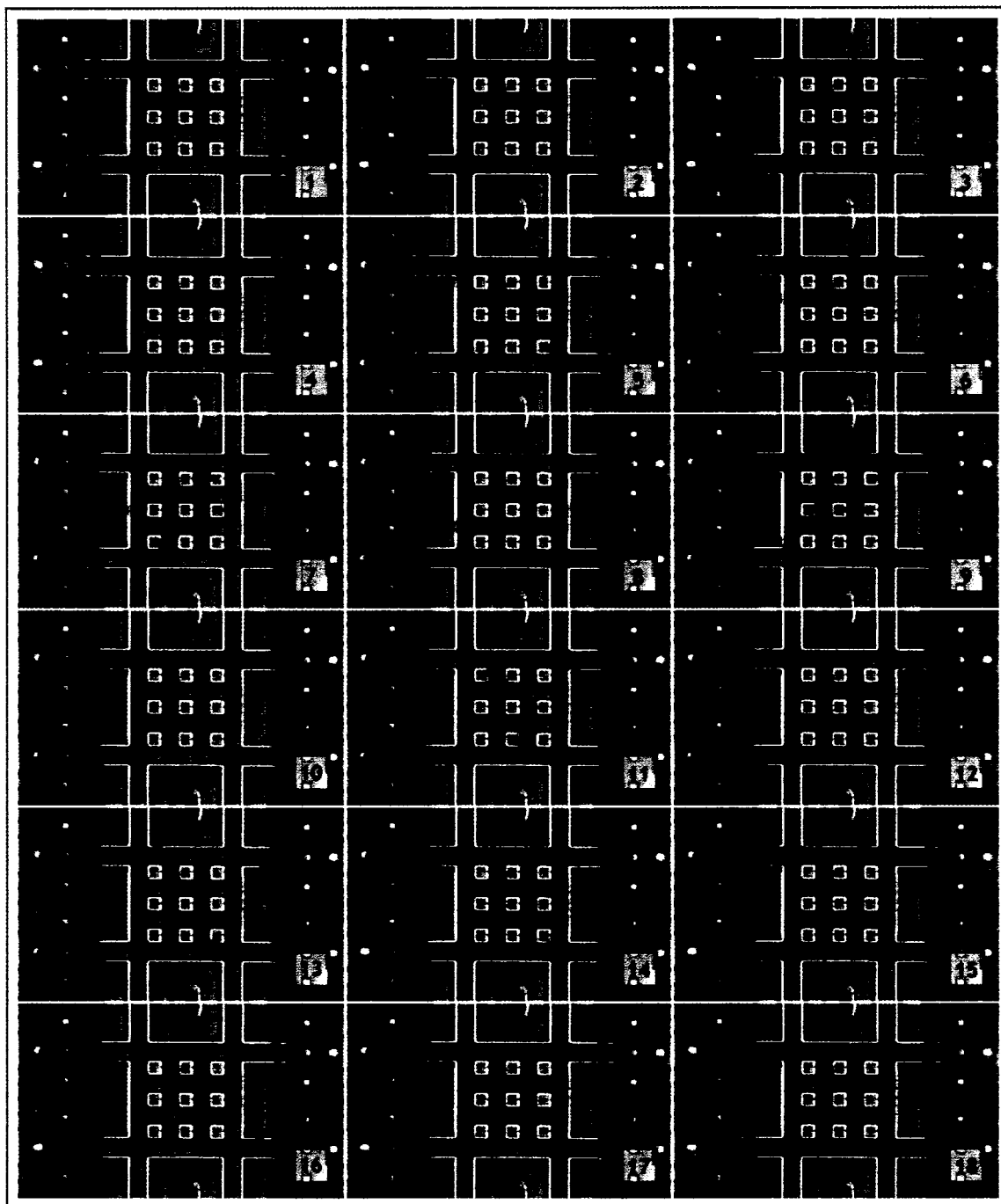
Figure 5.12: Time-lapsed sequence of images demonstrating the simultaneous dispensing and transport of four droplets in a closed loop.

in a zero net loss of liquid. No changes in the total volume of liquid in each reservoir was observed after 32 cycles.

5.3 Transport of Various Cooling Liquids

5.4 Hot-Spot Cooling in an Open System

The feasibility of the droplets to cool hot spots in an open system was tested by applying 660mW to the thin-film heater (equivalent to a heat flux of 30 W/cm^2), upon which a single droplet was transported across the nine-electrode linear array. The switching frequency of the electrodes was varied from 18 to 32 Hz which translates to droplet residence times on each electrode from 55ms to 31ms. The droplet was shuttled back and forth on the 9-electrode linear array for 10s at 32 Hz switching frequency and held away from the hot spot stationarily on an electrode for 5s. The shuttling of the droplets again resumed for 10s at the next frequency and held stationary for 5s and this process continued through all the switching frequencies. Storing the droplets away from the heat source for 5s allowed any heat stored in the droplet to dissipate before being transported at the next switching frequency. Figure 3 shows a sequence of time-lapsed images of the droplet cooling the hot spot, in both the infrared and visible spectrum, as it traverses across the linear array. At $t = 0$s in Figure 5.13, the temperature at the hot spot is 70°C and from image processing yielded a temperature decrease of 23°C at the hot spot after a quarter of a second of shuttling the droplet at a 32 Hz switching frequency.

5.4.1 Effects of Switching Frequency

The temperature of the hot spot as a function of time at different switching frequencies is shown in Figure 5.14 for the duration of the experiment.

The data shown was captured every 1/30th seconds. At each switching frequency, the

96
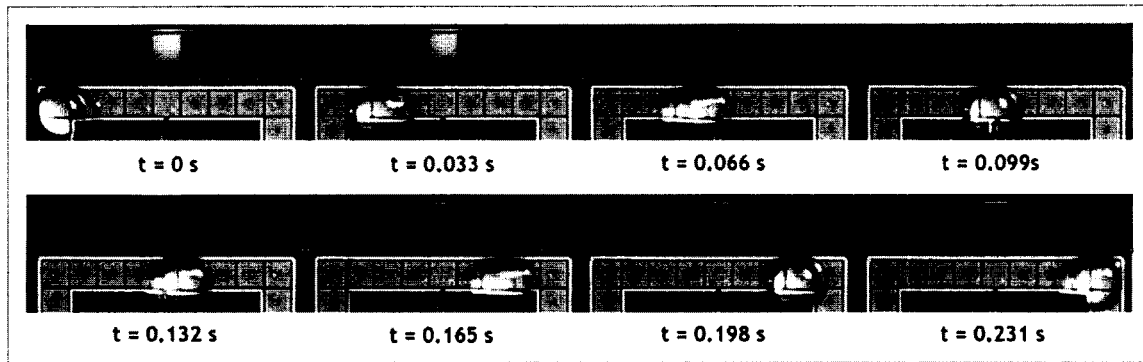
Figure 5.13: Top view of droplet transport as viewed from an infrared camera (top image in each frame, white = hot) and regular camera (bottom image). A droplet volume of volume 6?l is transported across the hot spot (65°C) at a switching frequency of 32 Hz. The hot spot is cooled by 20°C at t = 0.231s.

g

temperature of the hot spot varied between low and high temperature values. The lower value corresponds to the temperature of the droplet as it passes over the hot spot, and the higher value is the maximum temperature of the hot spot when the droplet is at either of the far ends of the linear array. It should be noted that the temperature of the hot spots is lower at higher switching frequencies. This is an expected result since a droplet shuttling at higher speeds corresponds to higher flow rates and therefore it removes heat faster. The time-averaged temperature of the droplet increased at a rate of approximately 0.22°C/s, while the average cooling rate of the hot spot was found to be 5.5°C/s at 32 Hz.

Due to the interference of the droplet during infrared imaging, the lowest temperature of the hot spot could not be obtained as the water droplet does not transmit IR. Therefore, the "coolability" (i.e. temperature drop) due to the shuttling droplet is calculated as the difference between the higher values at each frequency and the steady-state value of the hot spot obtained at the end of the experiment. It is important to note that this represents a worst-case scenario, as it is likely that the hot spot is actually cooled to a much lower temperature.
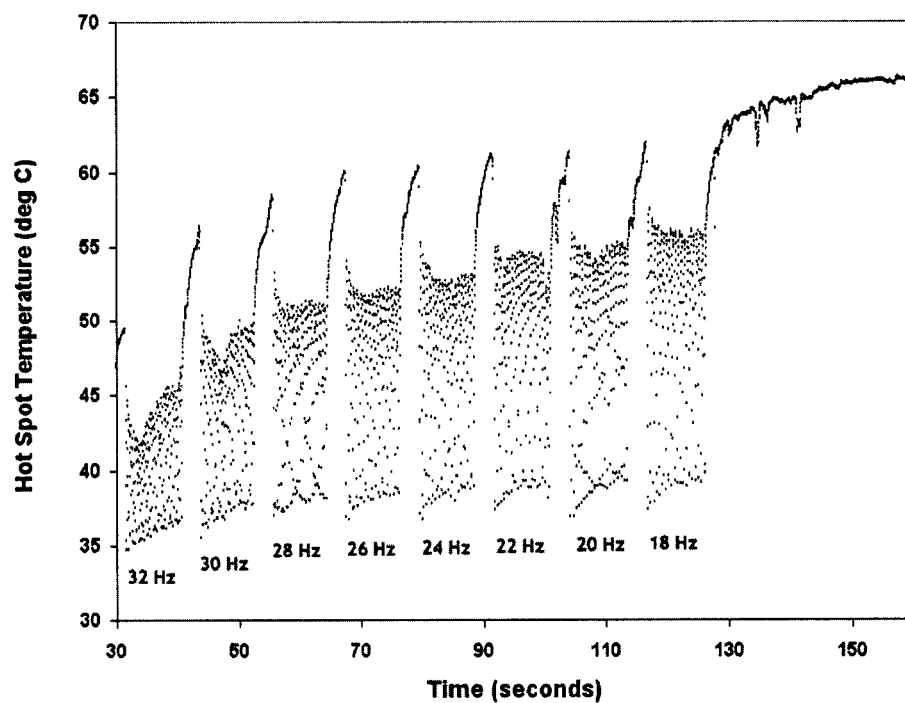
Figure 5.14: Variation in the temperature of the hot spot with the droplet shuttling at various frequencies. At each frequency, the droplet was shuttled back and forth the linear array for 10s, and stationarily held away from the hot spot for 5s to allow any heat stored in the droplet to dissipate. At the end of the experiment, the hot spot was allowed to reach a steady-state temperature.

5.4.2 Effects of Hot-Spot Heat Flux Density

The coolability of the droplets with switching frequencies from 18 to 32 Hz was obtained for heater input power ranging from 360mW to 660mW. As shown in Figure 5.15, the effectiveness of cooling by the droplets improves as the input power to the hot spot increases at higher frequencies. For example, at a switching frequency of 32 Hz, there is a 150% increase in the temperature drop for an 83% increase in heater power from 360mW to 660 mW. This suggests that cooling performance is greatly improved as the power densities in the hot spot are increased. It should be noted that below the switching frequency of 22 Hz, the temperature drop for input power of 560mW and 660mW is the same but the temperature drop increases at higher switching frequencies for 660mW of input power densities. This suggests that the heat removal of the droplets saturates at a particular switching frequency and any increase in input power would not change the heat removal while decrease in input power would lead to a smaller temperature drop. Due to the power limitations of the thin-film heater, the upper limit of this trend could not be obtained. The copper traces of the heaters would open at input power beyond 660mW so experiments were not performed at higher input power. Another limitation of this method is that water droplets evaporate at 100°C and therefore liquids with higher boiling points, such as DMSO, must be used to cool higher temperatures.

Figure 5.16 shows the relative heat transfer coefficients, defined by Newton's law of cooling, as calculated from the data obtained in Figure 5.15. Since the heat input from the hot spot to the droplet, dQ/dt, was difficult to obtain experimentally, the heat transfer coefficients were normalized to the best-case scenario (heater power = 660mW, switching frequency = 32 Hz) and it was also assumed that the power delivered to the hot spot in contact with the droplet was linearly proportional to the input power delivered to the heater on the back-side of the PCB.

At low frequencies, the change in heat transfer coefficients of the droplets was observed
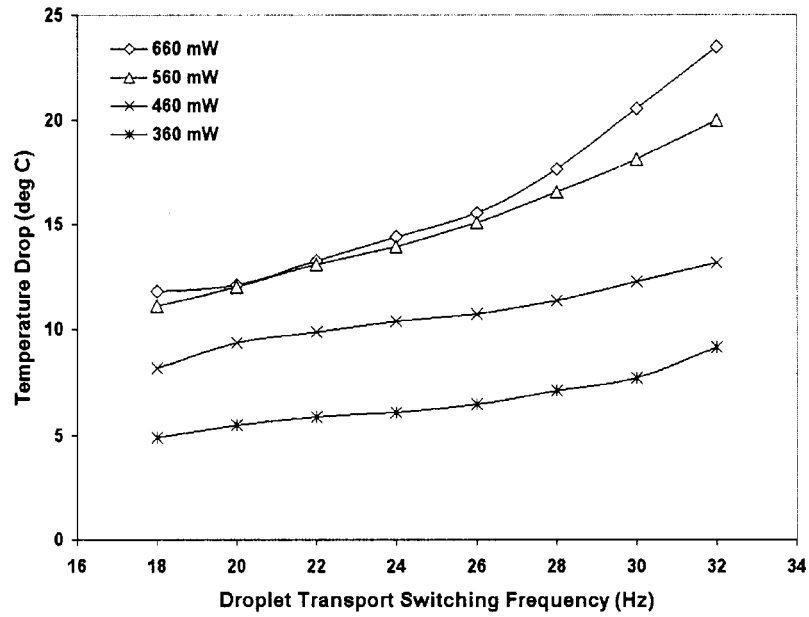
Figure 5.15: Temperature drop at the hot spot with respect to switching frequency of a shuttling droplet as a function of input power.
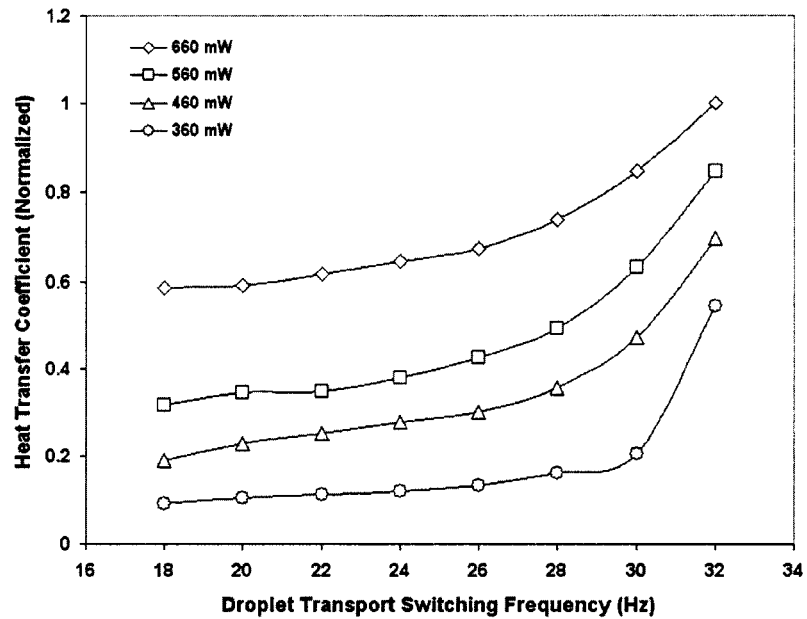
Figure 5.16: Heat transfer coefficients between the droplet and hot spot at various heater powers (360 to 660 mW) and droplet transport frequencies (18 to 32 Hz).

100

to be almost linear, while at higher frequencies the increase in heat transfer coefficient is more rapid. Cooling is therefore significantly enhanced at higher effective flow rates of the droplet. Although only a single droplet was studied here, up to four additional droplets could be simultaneously transported across the 9-electrode linear array, thus increasing the effective flow rate by 5x given the same switching frequency (i.e., the flow rate of five droplets transported at 32 Hz across the linear array has the same effective flow rate as a single droplet transported at 160 Hz). The feasibility of simultaneously transporting multiple droplets has been demonstrated by us earlier [10].

5.5 Hot-Spot Cooling in a Closed System

The ability of droplets to cool a hot-spot within a closed system was investigated using an array of RTDs to measure temperature and a thin-film heater to simulate the hot-spot. The power applied to the heater was 187.5 mW, resulting in a heat flux density of 33.3 W/cm^2, upon which a single droplet was transported across a five-electrode linear array. The volume of each droplet was 1.8 μl, the electrode pitch was 1.5 mm, and the droplet height was 600μm. The switching frequency was varied from 4 to 16 Hz, which resulted in 1 to 4 Hz frequencies in which the droplet encounters the hot-spot. The temperature was recorded at a rate of 10 samples/sec, and the steady state temperature of the hot-spot in both oil and air were also obtained.

5.5.1 Effect of Switching Frequency

Figure 5.17 shows the temperature profile of the hot-spot as the droplet was oscillated across its surface. The steady state temperature of the heater was 90°C in air and 78°C in oil. As the droplet resides on top of the hot-spot, the temperature quickly reduces to ~60°C, despite the switching frequency. As the droplet moves away from the hot-spot, its temperature begins to rise but quickly reduces again as the droplet returns to the hot-spot.

The value of this upper limit is dependent on the rate at which the droplet returns to the hot-spot, i.e. the switching frequency. If the switching frequency is increased, the upper limit becomes smaller.
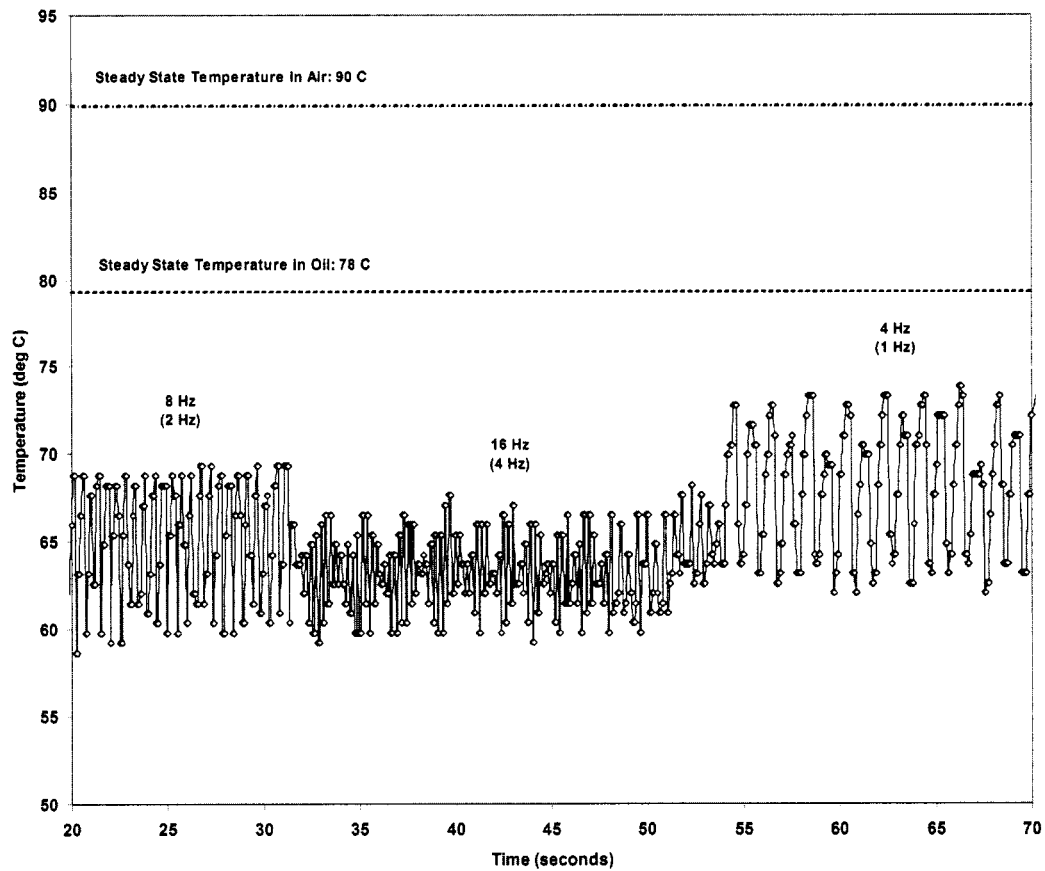
Figure 5.17: Temperature profile of a hot-spot as a droplet is oscillated across its surface in a closed system.

The relationship between this upper limit and the frequency at which the droplet meets the hot-spot is shown in Table 5.5.1. We predict that as the the switching frequency of the droplet continues to increase, the temperature asymptotes to the lower limit of 60°C.

Residence Frequency (Hz)	Temperature (°C)
1	73.24
2	68.76
4	66.51

Table 5.5: Upper limit of temperature from Figure 5.17 vs. residence frequency.

5.5.2 Effect of Droplet Volume

To study the effects of absolute scaling (i.e., the scaling of the system in all three dimensions), a similar set of experiments as described above was performed, but with 50 nL droplets on 750μm pitched square electrodes and a 100μm height. The power to the heater was such that the steady state temperature in oil was 80°C. Figure 5.18 compares the temperature drop observed for both the 1.8μl and 50nl droplets.

For a 1.8μl droplet, the temperature drops observed ranged from 4.76°C to 11.5°C as the droplet speed increases, however, the effects are less noticeable for the scaled system. Temperature drops of less than 1.5°C was observed for a 50nL droplet, suggesting that heat transfer characteristics are worsened as the absolute dimensions of the system are scaled down.

This trend is consistent with the specific heat equation, which tells us that heat transfer is proportional on the mass flow rate of the cooling liquid. The mass flow rate, defined as

$$\dot{m} = \frac{dm}{dt} = \rho A v \tag{5.1}$$

where ρ is the liquid density, A is the cross sectional area, and v is the droplet speed, suggests that in order to achieve the same heat transfer in the larger droplet, the smaller droplet (which is 1/36th the mass of the larger droplet) must travel 36 times the speed of the larger droplet. Hence, for the the larger droplet residing on the hot-spot at a frequency of 1 Hz, the smaller droplet must have a residence frequency of 36 Hz. This requires the 50 nL droplet to travel with a switching frequency of 144 Hz, well above the capability of
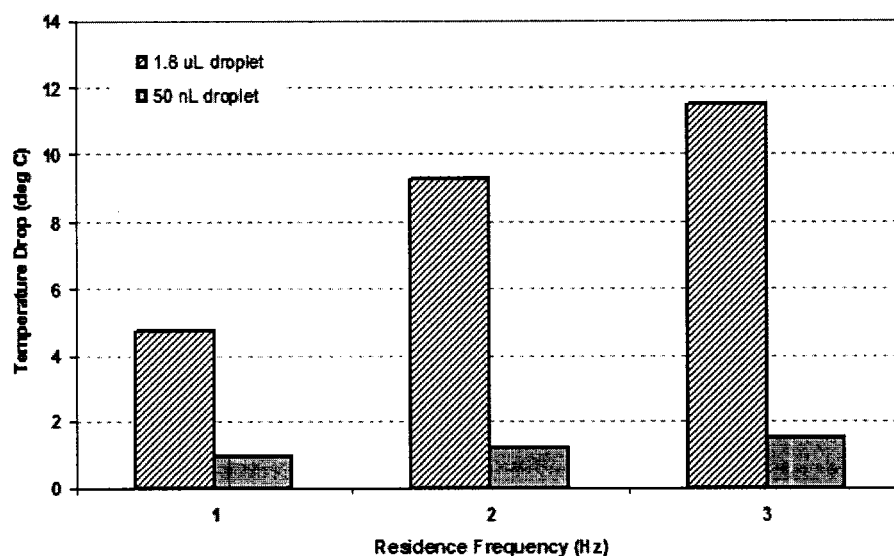
Figure 5.18: Temperature drop of a hot-spot during the oscillation of 1.8μl and 50 nL droplets.

our current system.

(As a first approximation, we can assume a linear trend in the 50 nL droplet for the data shown in Figure 5.18, and thus calculate the temperature drop for the 50 nL droplet to be 7°C at a residence frequency of 36 Hz, and 13°C at a residence frequency of 72 Hz. These values are within the range of temperature drops we see for the 1.8μl droplet with a residence time of 1 and 2Hz, respectively.)

5.5.3 Effect of Background Heating

The experiments performed thus far neglect the effect of background heating from the target substrate to be cooled. While the results shown thus far demonstrate the ability for droplets to cool hot-spots given a sufficient mass flow rate, they were based on the assumption that the flow paths leading to and away from the hot-spot were at ambient room temperature. An actual implementation of a flow-through based adaptive cooler would have to address not only the presence of hot-spots, but a high level of background heating

as well.

An experiment was performed in which a 50 nL droplet was dispensed and transported across a heat flux boundary. A silicon strip heater was used to simulate a background heat flux of $\sim 30W/cm^2$, which reached a steady state temperature of 80°C. The droplet, dispensed at room temperature, would then be transported through silicone oil into and out of the boundary while the temperature profile of the entire chip was being imaged using an infrared camera. The infrared video was then recorded and processed in MATLAB.
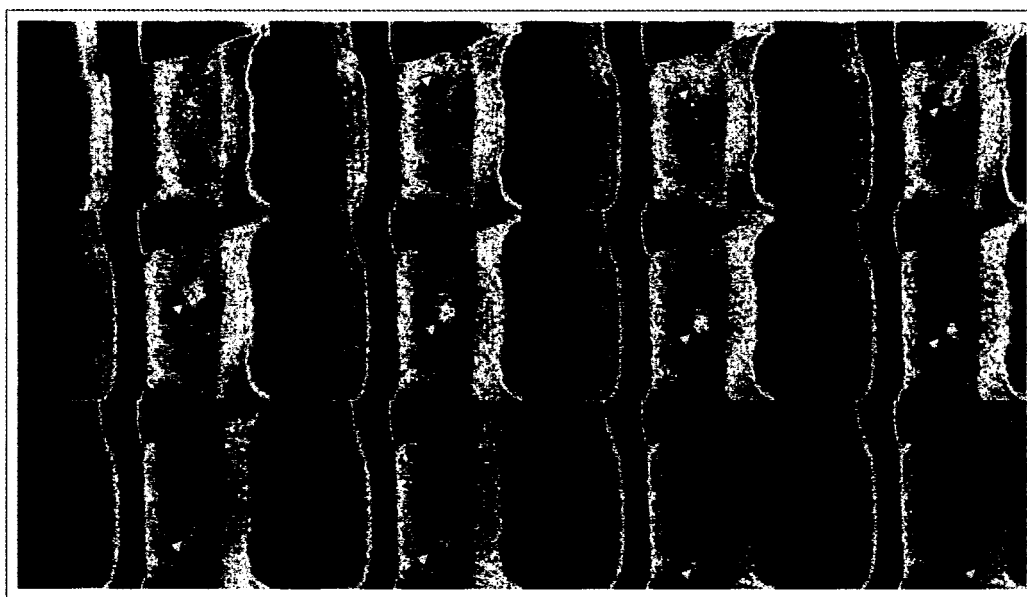
Figure 5.19: Time-lapsed sequence of infrared video of a droplet transport through a heat flux boundary. The arrow indicates the position of the droplet.

A sequence of images, after image enhancement and false color mapping, reveals the footprint of the droplet as it travels across the chip. Shown in Figure 5.19, the footprint of the droplet is not visible as it approached the silicon heater (boxed in black), since both the oil and the droplet are at room temperature. Only when the droplet crosses the heat flux boundary is its footprint noticeable. The temperature of the droplet's footprint as it travels down the heat flux boundary was calculated and is shown Figure 5.20. The maximum temperature drop of the silicon heater is less than 0.6°C, indicating poor localized

heat transfer. A steady increase in temperature is observed as the droplet continued to be subjected to background heating.
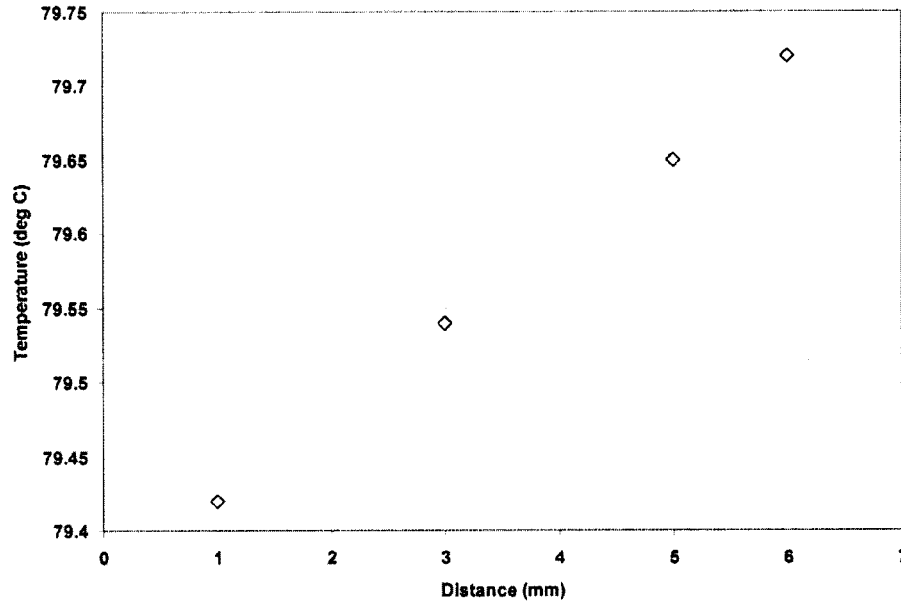
Figure 5.20: Temperature of the silicon heater at various location as a droplet travels across its surface.

As the droplet exits the heat flux boundary, the footprint becomes lost, suggesting that the droplet, which had been heated to 79.5°C in the heat flux boundary, was already cooled to the ambient temperature of the oil. Due to the small thermal mass of the 50 nL droplet, the temperature of the droplet may have reached thermal equilibraium with the surrounding oil faster than the rate of transport.

Since direct measurement of the nanoliter-sized water droplet and the silicone oil was not possible to verify this hypothesis, the system was simulated in ANSYS. A two-dimension model of the droplet was programmed such that a 750μm diameter water droplet was surrounded in oil, fixed at a temperature of 100°C. The droplet was given an initial condition of 25°C, and a transient analysis was performed.

As shown in Figure 5.21, we predict that the droplet in this two-dimensional model

106
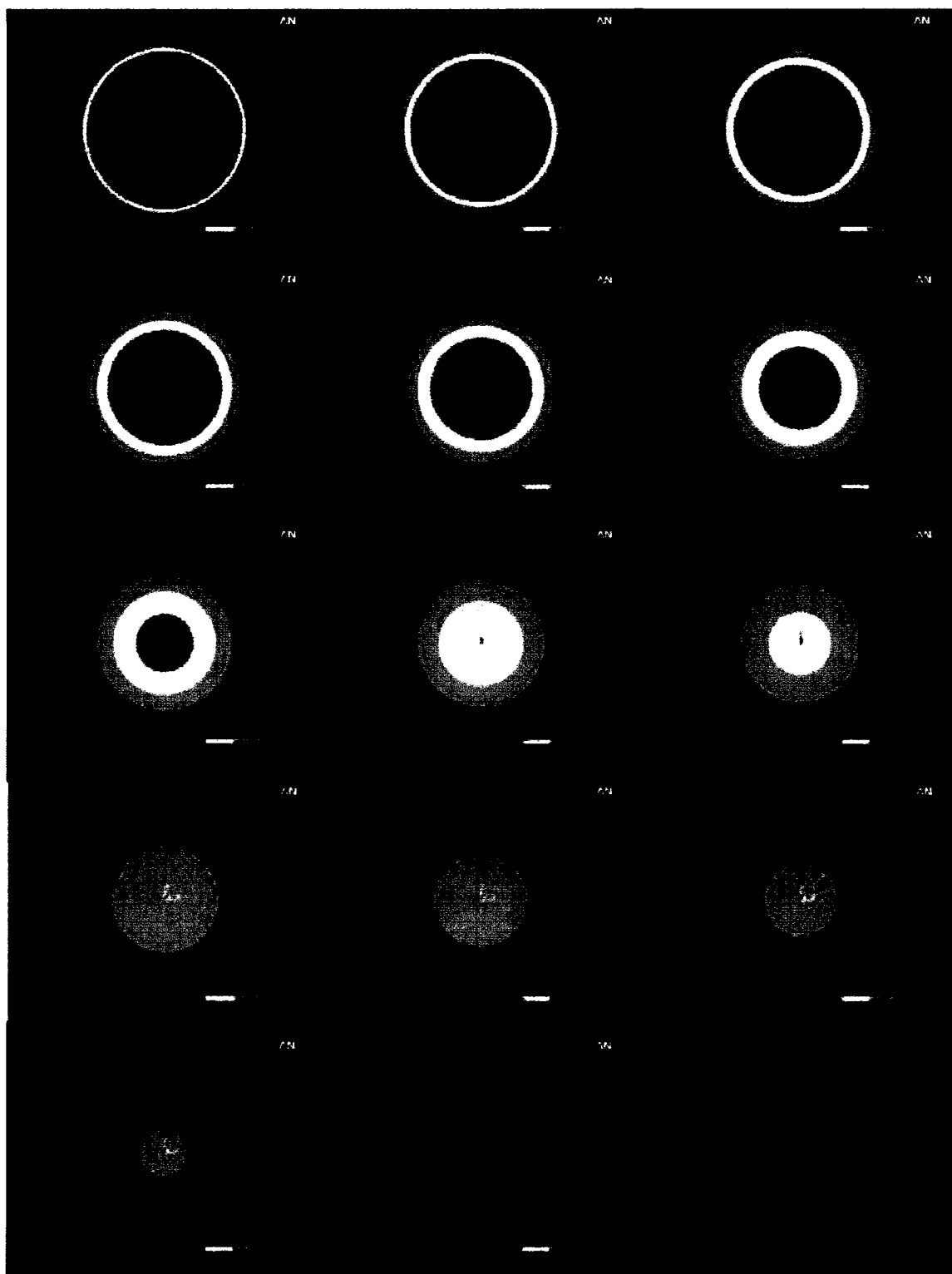
Figure 5.21: Transient ANSYS simulations of a 750μm diameter droplet as it equilibrates with a boundary condition of $100°$C. The time between each image is 10μs.

reaches the steady state temperature of 100°C within 150μs. We can extend this model to a three-dimensional droplet with a diameter of 750μm and a height of 100μm. The result, shown in Figure 5.22, reveals that steady state in the three-dimensional droplet is reached within 200μs.
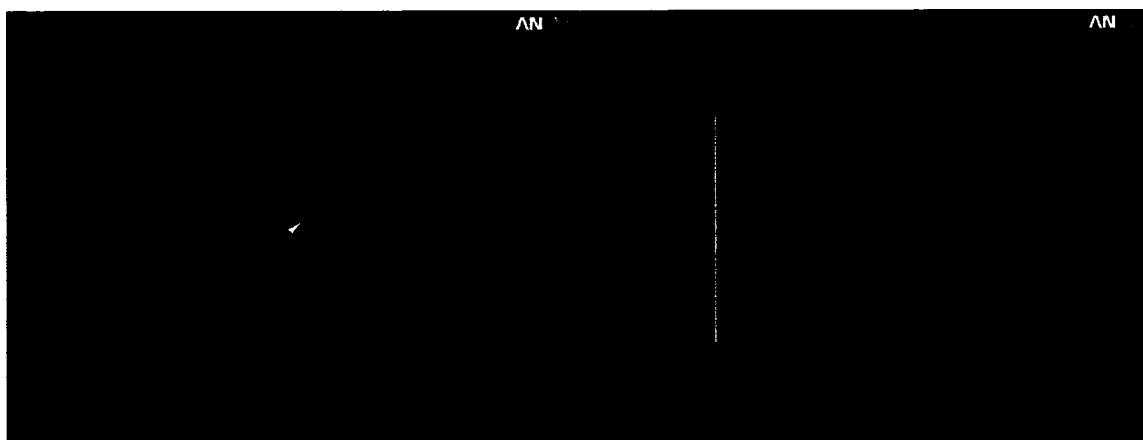
Figure 5.22: Model of a 750μm diameter, 100μm tall droplet in ANSYS (left). Transient analysis of the center of the droplet as it equilibrates with a boundary condition of 100°C.

These simulations suggest that the temperature of the droplet is indeed equilibrating with the surrounding oil at a rate much greater than the droplet's transport speed. This is partly attributed to similarity of thermal characteristics (specific heat capacity and thermal conductivity) of both silicone oil and water, promoting heat transfer between the two liquids. Furthermore, since there should be little difference between the thermal resistance between the two liquids, the fluid layer, as seen from the silicon heater, has a relatively constant thermal resistance, and thus cannot experience localized cooling at the flow rates demonstrated here.

5.6 Static Heat Transfer Characterization

Static heat transfer experiments were performed to study the rate of heat transfer of droplets under various conditions. For a fixed diameter of $\sim$1.25μm, droplet volumes of 0.4 to 1.4

μl with respective heights of 170 to 600 μm were studied. Hot-spot power densities ranged from 3.6 to 25.3 W/cm^2.

Figure 5.23 is example data for a 600 μm tall droplet 1 μl in volume with a hot-spot heat flux density of 14.2W/cm^2. The graph shows two curves, where the upper curve is the temperature of the top side of the droplet where the hot-spot is applied, and the lower curve is temperature of the bottom side of the droplet. When the hot-spot is applied at $t = 0$s, the temperatures of both sides of the droplet rise and reach a steady state value. The time constants for each curve is calculated by noting the time at which 63% of the steady state value is reached.
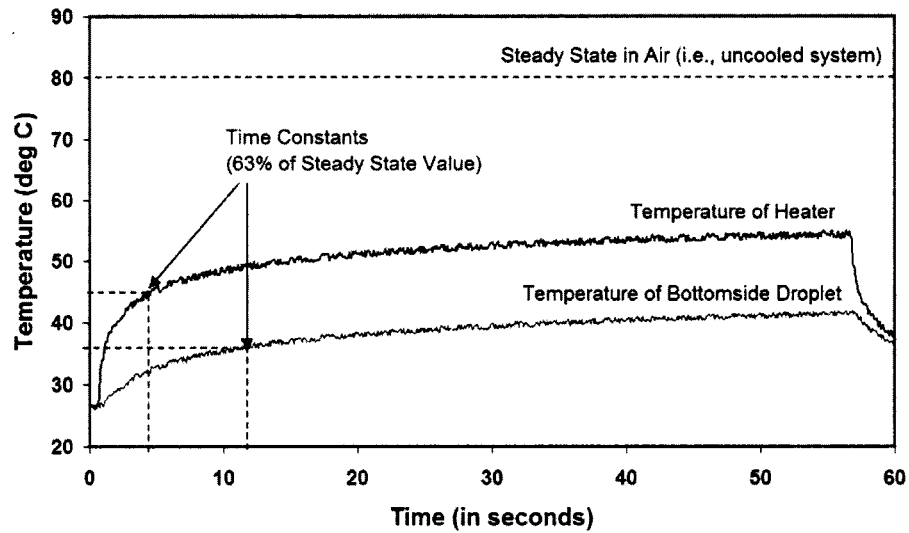
Figure 5.23: Time-varying temperature of the top and bottom side of a droplet as it is heated from the top side.

5.6.1   Effect of Heat Flux Density

A relationship between the hot-spot heat flux density and heating time constant for a 400 μm tall droplet is shown in Figure 5.24. The volume of the droplet in this experiment was 1 μl. An effective time constant is calculated by taking the difference between the time

109

constant from the top and bottom of the droplet. As the heat flux density increases, the time constant decreases, with the fastest effective time constant being 2.4s at 25.3 W/cm^2. The data here supports the idea that droplets should be transported at very high rates for two reasons. First, at high power densities, the droplet should be moved away before it equilibrates with a high surface temperature and exceeds its heat capacity. Second, at low power densities, the heat flux from the hot-spot to the droplet is low, requiring longer residence time to reach thermal equilibrium. Thus, it would be advantageous to transport droplets at a high rate such that each new droplet would provide the required temperature differential to result in larger heat fluxes in the hot-spot.
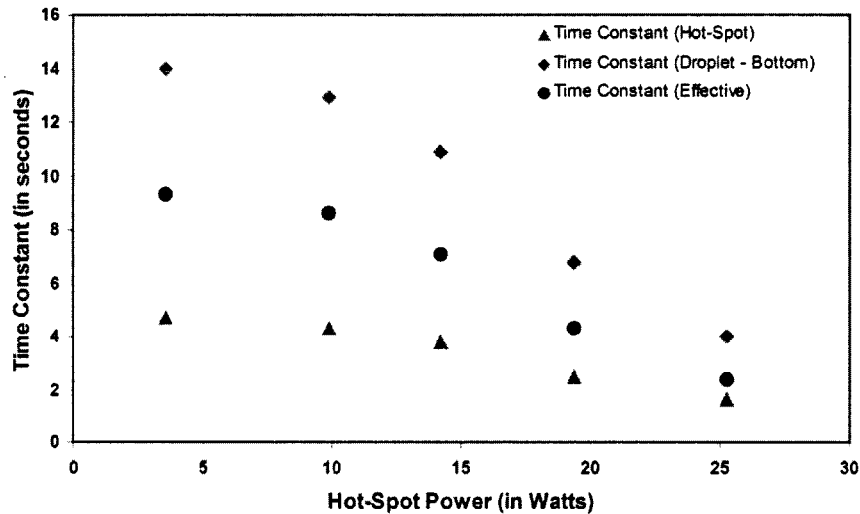
Figure 5.24: Time constants versus hot-spot heat flux density for a $1\mu l$ droplet that was $400\mu m$ in height.

5.6.2 Effect of Droplet Aspect Ratio

A relationship between the droplet aspect ratio and heating time constant given a 14.2 W/cm^2 hot-spot heat flux density is shown in Figure 5.25. As aspect ratio increases (i.e. the droplets become thinner), the effective time constants decreases, with the fastest time constant being 1.2s for a $170\mu m$ tall droplet.

110

From this data and from the heat flux density trends in Figure 5.24, we can predict that the time constant for a 400 nL droplet which is $170\mu m$ tall would have a time constant of 400 ms given a heat flux density of $25W/cm^2$. This suggests that the maximum time during which a droplet can reside in the active area in order not to exceed its heat capacities is less than 1s. This droplet must thus move at a transport frequency of at least 12 Hz to cross a 1.5cm $\times$ 1.5cm active area. At the projected hot-spot power densities of $600W/cm^2$ and droplet volumes/heights of 50 nL and $100\mu m$ in an actual system, the minimum transport frequencies need to be orders of magnitude higher. Such transport frequencies can be achieved by using higher-k dielectrics and/or thinner insulator thicknesses, and should thus be investigated.
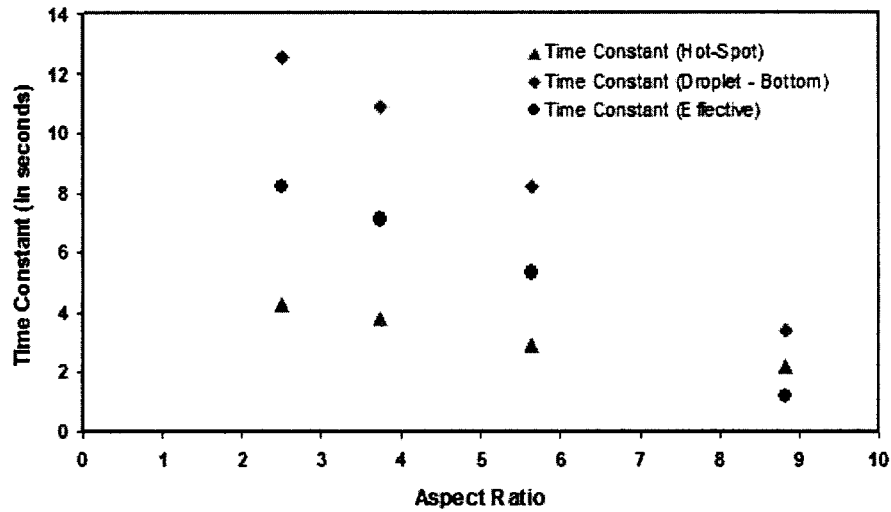
Figure 5.25: Time constants versus aspect ratio for a heater power density of 14.2 W/cm^2.

5.7 Chapter Summary and Conclusions

The design, fabrication, and testing of a PCB-based digital microfluidic cooling prototype was studied. A number of design changes were made until a reliable architecture was obtained. The resulting two-layer coplanar PCB prototype allowed for repeatable dispensing,

transport, and recycling of droplets in a closed-loop system. Using these prototypes, we have demonstrated for the first time the ability to program droplets to cool hot-spots in both an open and closed system, and investigated parameters affecting heat-transfer such as droplet aspect ratio, absolute volumes, hot-spot power densities, and the presence of a filler fluid. In general, parameters that increased the mass flow rate, such as the absolute size of the droplet and transport speeds, exhibited significantly higher heat transfer characteristics. Hence, larger droplets with higher residence frequencies were able to cool hot-spots better than smaller droplets with lower residence frequencies. Cooling was also found to increase as the power densities of the hot-spots increased, which is the result of the increased temperature differential between the droplet and the hot-spot.

The ability for droplets to cool hot-spots became less pronounced in the presence of a background heat flux. Since both oil and water have similar thermal properties, the temperature of the droplet appeared to rapidly equilibrate with the temperature of the surrounding oil. Given an insufficient transport speed, the droplet would already have experienced its maximum heat capacity by the time it reached the hot-spot.

While the ability for droplets to cool hot-spots have been demonstrated in this chapter, the parameters studied here suggest that for the nanoliter volumes and power densities to be implemented in real systems, droplets must be transported at speeds well above the limits of our current prototype. However, transport speeds can be greatly improved by investigating alternative dielectrics used to insulate the electrodes from the droplet. The LPI soldermask used in these studies exhibit contact angle saturation, charging, and dielectric breakdown when larger driving voltages are used to increase the droplet transport speeds. However, a wide range of dielectrics have not yet been tested which could significantly increase the maximum attainable droplet speed, thus satisfying the requirements for flow-through based droplet cooling in current and future IC devices.

Chapter 6

Experimental Results: Programmable Thermal Switch Method

The flow-through based cooling method studied in Chapter 5 exploited electrowetting-based actuation to move droplets in reconfigurable flow paths and flow rates. In this chapter, we explore the possibility of using electrowetting to create a programmable thermal switch, whereby a liquid-metal based droplet can be manipulated such that an area in the cooling device can be selectively switched from a low thermal conductivity mode to a high thermal conductivity mode. This allows for a programmable thermal conductivity layer which can reconfigure itself in response to the non-uniform heat-flux in the target IC substrate. The result is a continually uniform temperature profile, despite the thermal load from the IC. In this chapter, we investigate the feasibility of using mercury as a candidate for the thermal switch. We demonstrate the ability to move mercury droplets using electrowetting, and study both its steady state and transient heat transfer characteristics. Parameters such as mercury droplet size, heat densities, and the presence of copper vias are investigated for their effects on heat transfer in this system.

6.1   Experimental Methods

6.1.1   Mercury Droplet Transport

Mercury is a metal which is liquid at room temperature. It has a melting point of -38.87°C and a boiling point of 356.7°C. It is a dense material, 13.55 g/cm^3, making it the densest liquid metal known.

Mercury is considered a toxic substance and thus has limits set by the Occupational

Safety and Health Administration. However, due to the extremely small volumes that are used in our systems, the levels are well below these limits. As a comparison, high power 1000W mercury vapor lamps contain ~250 mg of mercury, which is equivalent to 18 μl of mercury. In the prototypical digital microfluidic systems discussed in this paper, the total volume required for 400 mercury droplets (750μm in size) to cover an active area of 1.5 cm × 1.5 cm is 16 μl. As the system is scaled down, the volume will subsequently decrease as well. More information about the health hazards and concentration limits of mercury can be found in Appendix D.

Mercury has a surface tension much larger than that of water (480 dynes/cm versus 72 dynes/cm). Its nominal contact angle with glass is near 180 degrees, making it appear super-hydrophobic with the surface. The ability to electrowet mercury has been demonstrated; a 74° contact angle (141° to 67°) was observed [8] (see Figure 6.1). It is therefore feasible to transport mercury droplets at rates similar to those observed with water.

(a)   (b)
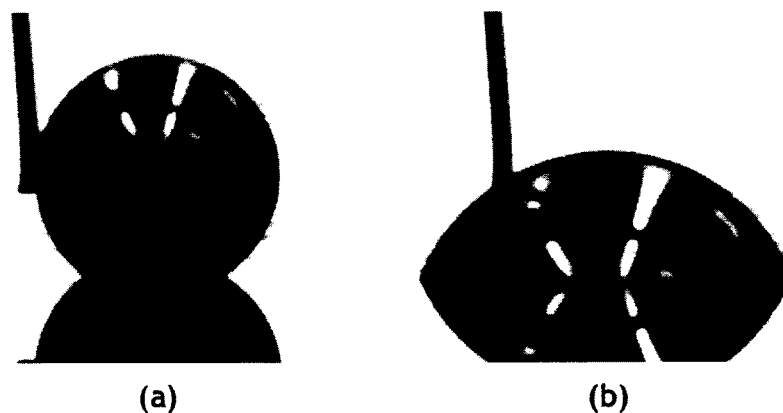
Figure 6.1: Electrowetting of a mercury droplet on a 0.6 m thick parylene surface as demonstrated by Zeng et al. [8]. (a) An initial contact angle of 141° and (b) the final contact angle of 67° with an applied potential of 180V.

The transportability of mercury was tested in both an open and a closed system using PCB-based digital microfluidic chips, with and without the presence of 1.5 cSt silicone oil. Droplets were dispensed using a micropippettor and oscillated across three 750 μm

pitched square electrodes. For an open system, droplets were imaged from the side to observe contact angle changes.

6.1.2 Steady State Heat Transfer of Mercury

The typical behavior of a microprocessor is to operate with some nominal level of background heat, and to produce localized hot-spot when a functional unit is turned on (e.g., an FPU). These functional units are typically used for a given period of time, resulting in the absence of the hot-spot when the functional unit is no longer running. Thus, it is important to study the steady-state effects of heat transfer when a mercury droplet is conducting heat away from a hot-spot, as the turn-on time for a functional unit can vary depending on the CPU's workload.

Top View　　　　　　　　　　　　**Side View**

Thin-Film Heater

Copper Via
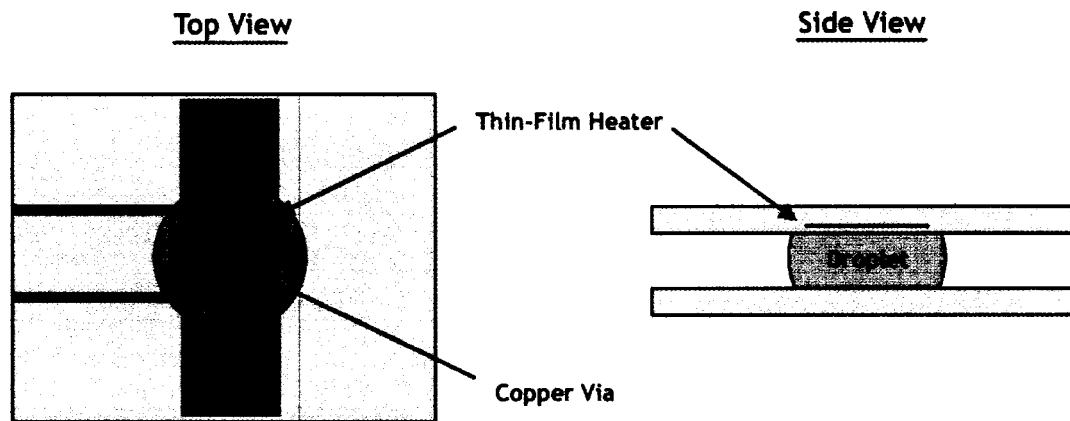
Figure 6.2: Experimental setup for the steady state heat conduction of a mercury droplet.

In the set of experiments illustrated in Figure 6.2, a mercury droplet is placed between a hot-spot and a via in a PCB microfluidic chip. The remaining chip was filled with silicone oil. The hot-spot was turned on at a specified power density, and the temperature of the hot-spot was measured as a function of time. This experiment was performed for hot-spot power densities of 100, 333, 500, and 750 W/cm^2. For comparison, the steady state temperature of the hot-spot in oil and in air was obtained. An on-chip RTD, intertwined

with the heater, was used to record the temperature of the droplet at a sampling rate of 100 ms.

6.1.3 Transient Heat Transfer of Mercury

To demonstrate the feasibility of a liquid-metal switch to selectively control the conduction of heat away from a hot-spot, we performed an experiment whereby a mercury droplet in oil, initially removed from a hot-spot, was delivered for some period of time, then again removed from the hot-spot. The experimental setup is illustrated in Figure 6.3. As a control, we observe a similar system in which droplets consist of water rather than mercury.
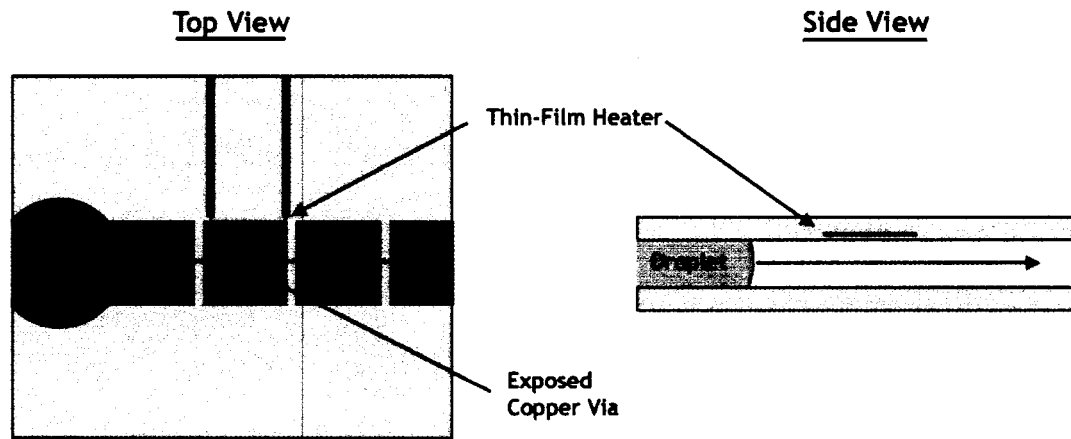
Figure 6.3: Experimental setup for the transient heat conduction of a mercury droplet.

As an additional variable, we observed the conduction of heat when a via was both present and absent beneath the mercury droplet to determine the effect of cooling due to the presence of the via in the microfluidic chip. An on-chip RTD, intertwined with the heater, was used to record the temperature of the droplet at a sampling rate of 100 ms.

116

6.2 Mercury Droplet Transport

Microliter-sized droplets of mercury were transported on PCB-based digital microfluidic chips. Successful transport was shown for mercury with and without a top plate, and for both in oil and in air. Maximum transport switching frequencies were higher in oil than in air, and the motion of droplets was more repeatable in the absence of a top plate. The observable contact angle change, while not measured, appeared much smaller compared to the value obtained by [8], even at the maximum voltage of 270V. Due to limitations in the controller circuit driving the electrodes, higher voltages were not tested.

In an open system, up to 32 Hz switching frequencies were observed at 270V. The minimum actuation voltages for droplet motion at 8 Hz fell below the minimum voltage of 80V allowable by our controllers. The transport of mercury may therefore require significantly lower actuation voltages than for water, which may be attributed to its super-hydrophobicity with the surface.

Figures 6.4 and 6.5 show a time-lapsed sequence of images of transport of mercury in both an open and closed system, and for both the presence and absence of silicone oil.
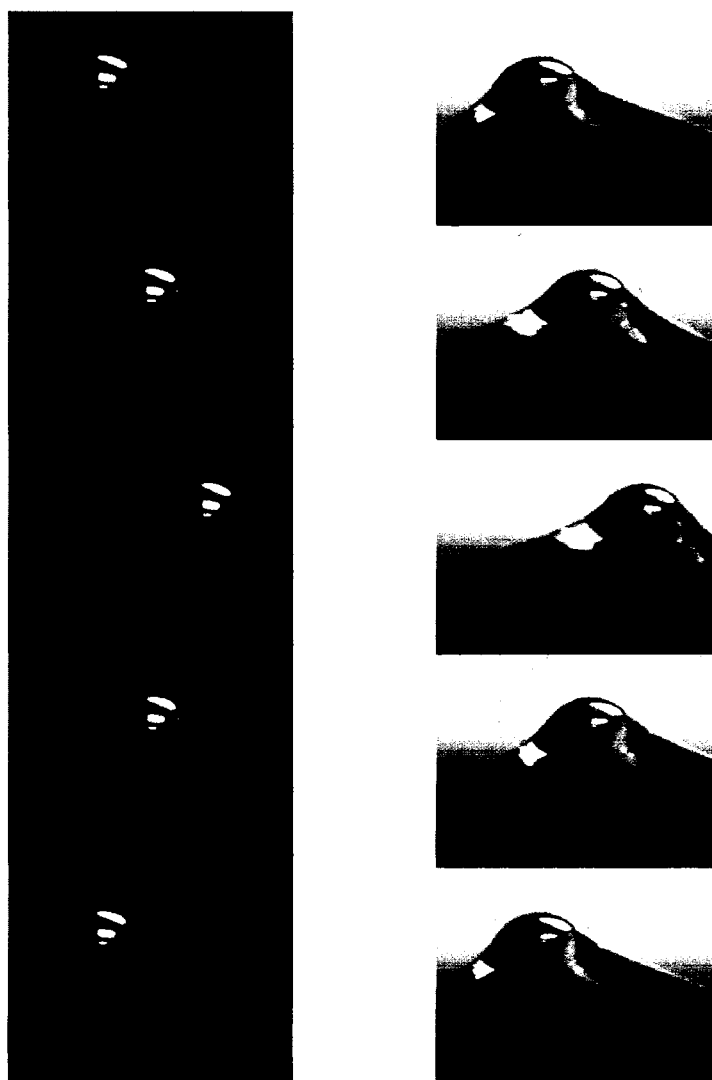
Figure 6.4: Side view of transport of a ~1 μl mercury droplet across three electrodes in an open system without silicone oil (left column) and with silicone oil (right column).
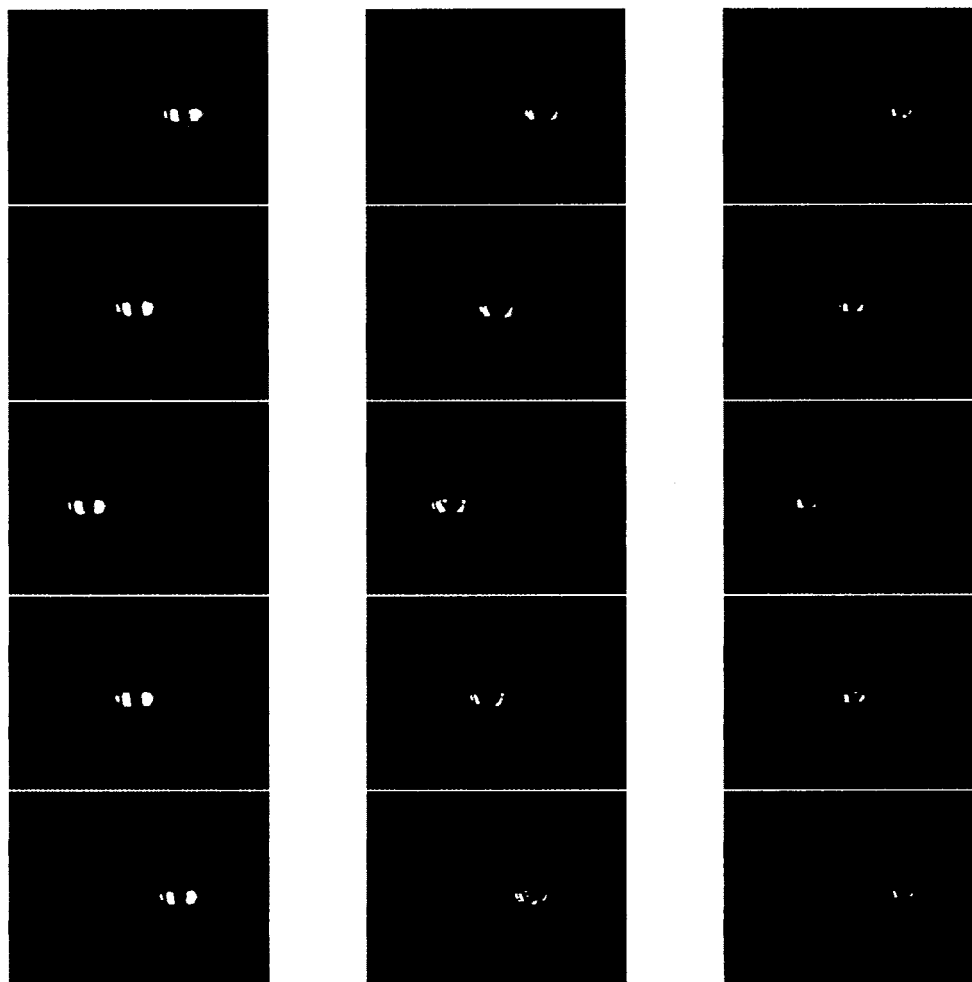
Figure 6.5: Top view of transport of a $\sim 1\mu l$ mercury droplet across three electrodes for an open system (left column), a closed system with a gap height of 1 mm without silicone oil (center column) and with silicone oil (right column).

6.3 Steady State Heat Transfer of Hot-Spots using Mercury

The steady state heat transfer characteristics of mercury were investigated for a 1 mm diameter droplet with a gap height of 100 μm. The hot-spot power densities were varied from 100 to 750 W/cm^2 and steady state temperatures were obtained for the hot-spot in air, in oil, and with the presence of a mercury droplet. The results are shown in Figures 6.6, 6.7, 6.8, and 6.9.
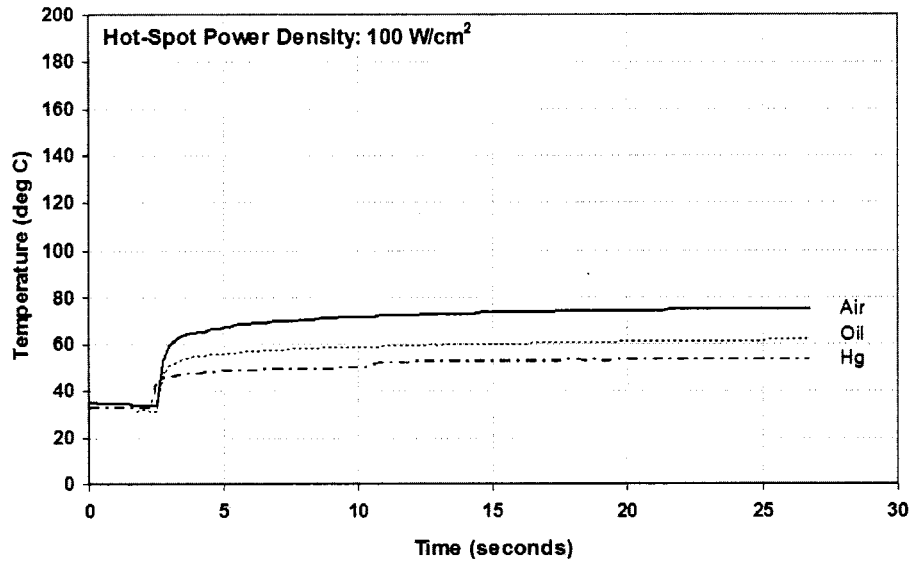
Figure 6.6: Temperature profiles of a hot-spot with a power density of 100 W/cm^2 in a PCB-based digital microfluidic filled with air, oil, or a mercury droplet in the presence of oil.

We observed that for each hot-spot power density, the steady state temperature for a system filled with oil is much lower than one filled with air. Further cooling was observed when a mercury droplet was placed underneath the hot-spot. In these systems, the addition of oil and mercury have reduced the thermal resistance between the hot-spot and the bottom microfluidic chip which, due to its large thermal mass, acts as a heat sink.

We also observe that as the hot-spot power density increases, the steady state tempera-
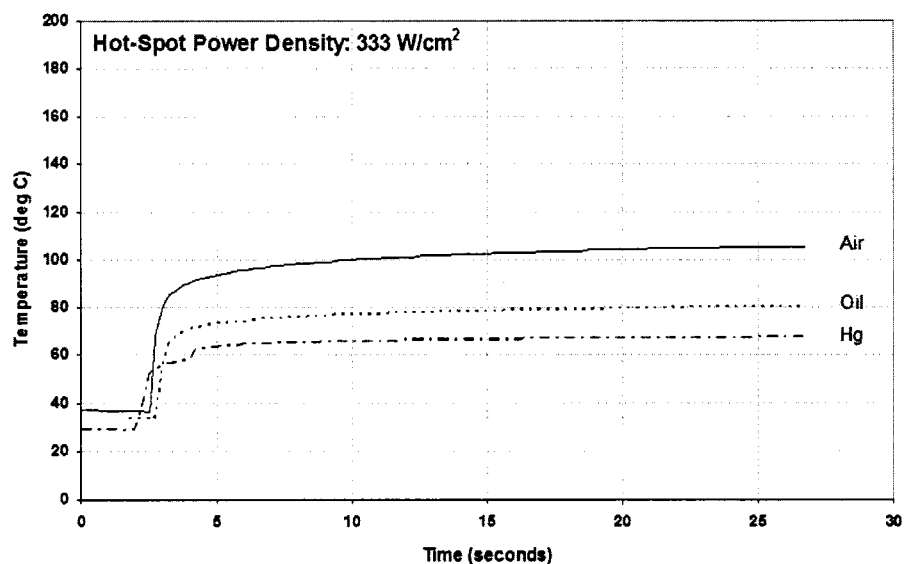
Figure 6.7: Temperature profiles of a hot-spot with a power density of 333 W/cm^2 in a PCB-based digital microfluidic filled with air, oil, or a mercury droplet in the presence of oil.
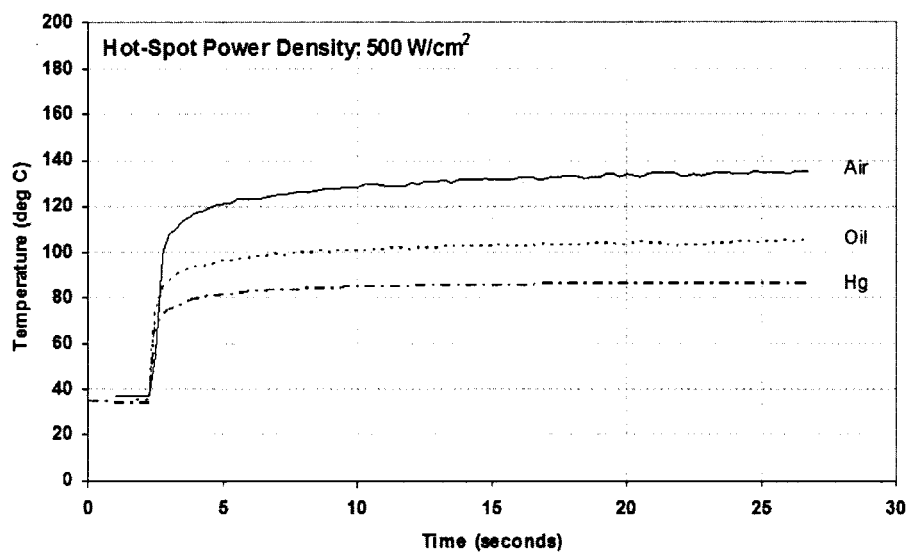
Figure 6.8: Temperature profiles of a hot-spot with a power density of 500 W/cm^2 in a PCB-based digital microfluidic filled with air, oil, or a mercury droplet in the presence of oil.

121
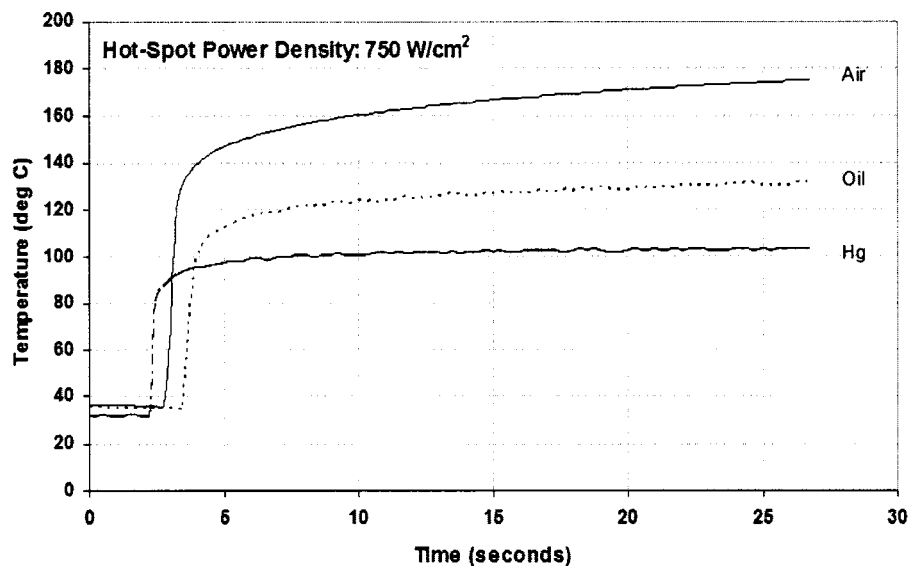
Figure 6.9: Temperature profiles of a hot-spot with a power density of 750 W/cm² in a PCB-based digital microfluidic filled with air, oil, or a mercury droplet in the presence of oil.
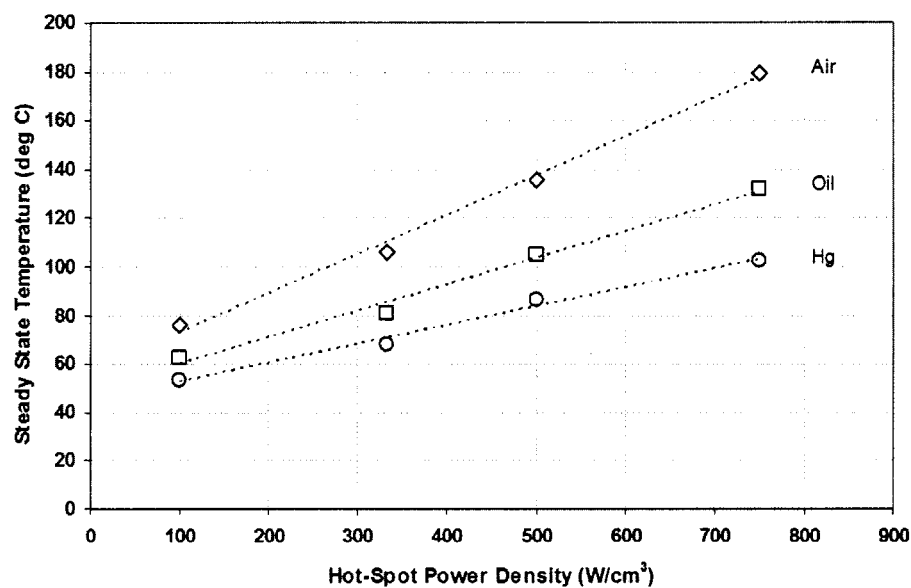
Figure 6.10: Steady state temperature of a hot-spot in air, oil, and in the presence of a mercury droplet with respect to the hot-spot heat-flux density.

122

ture of each system increases, as shown in Figure 6.10. However, in air and in oil, the rate of increase is higher than mercury, suggesting that the system does not perform any worse (and will most likely perform better) if this trend is continued for higher power densities.

It should be noted that in these experiments, while the hot-spot has a very high heat flux density, much of the heat is being distributed into the glass substrate on which the hot-spot was fabricated. Thus, it is not appropriate to compare these numbers directly with existing cooling systems until we know what percentage of power is being directed through the mercury droplet.

6.4 Transient Heat Transfer of Hot-Spots using Mercury

6.4.1 Effect of Copper Via on Heat Transfer

Figure 6.11 is temperature data obtained at a hot-spot when a mercury droplet was delivered for 20s, then removed. The hot-spot had a heat flux density of 500W/cm^2. We observe that the hot-spot had an initial steady state temperature of 89°C, which dropped by 9°C when the mercury droplet was delivered it. The hot-spot returned to its initial steady state value when the mercury droplet was moved away.

We repeated this experiment for both a mercury and a water droplet, with and without a via underneath the droplet. The results are shown in Figure 6.12. We observe a significant increase in the temperature drop using the mercury droplet over the water droplet. The presence of the via also promoted cooling. Due to its higher thermal conductivity, mercury is more effective in cooling the hot-spot than water, and the presence of the via allows for greater heat conduction through the PCB, thus greater cooling. While the via used in this system was epoxy-filled and copper-plated, a thermally conductive filled via is commercially available and would significantly improve cooling.
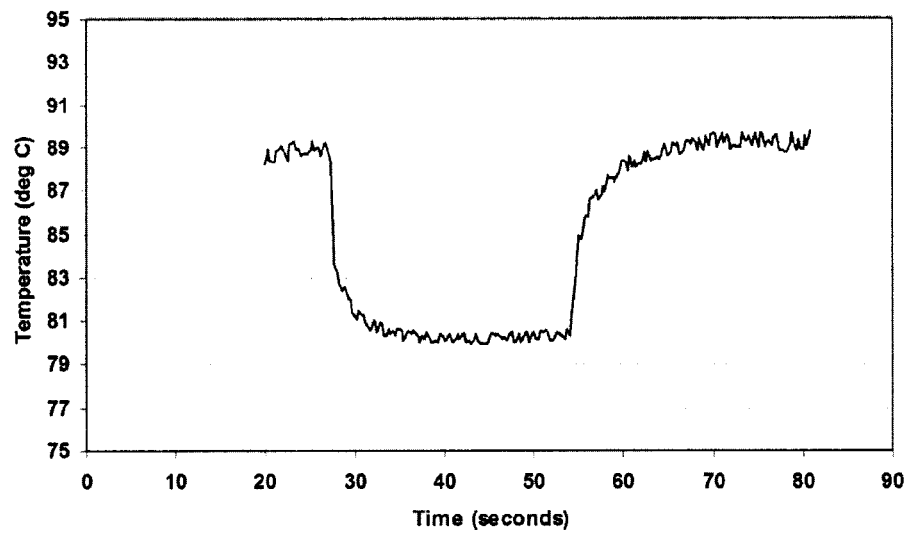
Figure 6.11: Temperature profile of a hot-spot as a mercury droplet is passed over it.
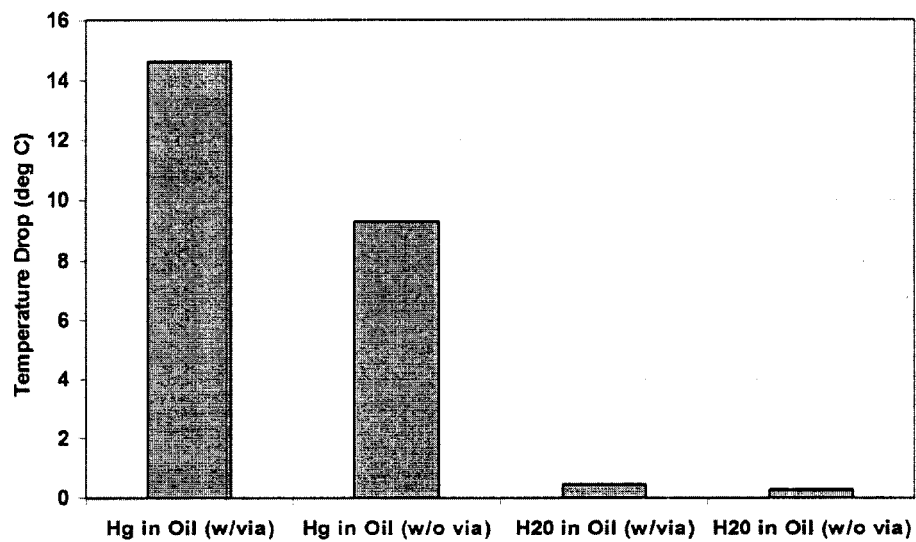
Figure 6.12: Temperature drop of a hot-spot when a mercury or water droplet is passed over it.

6.4.2 Effect of heat flux density on Heat Transfer

Figure 6.13 shows the relationship between the heat transfer of the mercury droplet and heat flux density of the hot-spot. Power densities as high as 500 W/cm^2 were applied to a thin-film heater 500μm x 500μm in size. The resulting steady-state temperatures of the hot-spot ranged from 110 to 557°C in air, 76.5 to 466°C in oil, and 72.7 to 373°C for a mercury droplet $\sim$1 mm^2 in area. At 500 W/cm^2, the hot-spot temperature drop from the uncooled system (in-air) to the system cooled by the mercury droplet (Hg in oil) was as large as 184°C, twice as large as the temperature drop observed for the hot-spot cooled by oil only. This is a significant improvement over the 11% increase in temperature drop observed for the hot-spot with a heat flux density of 133 W/cm^2.
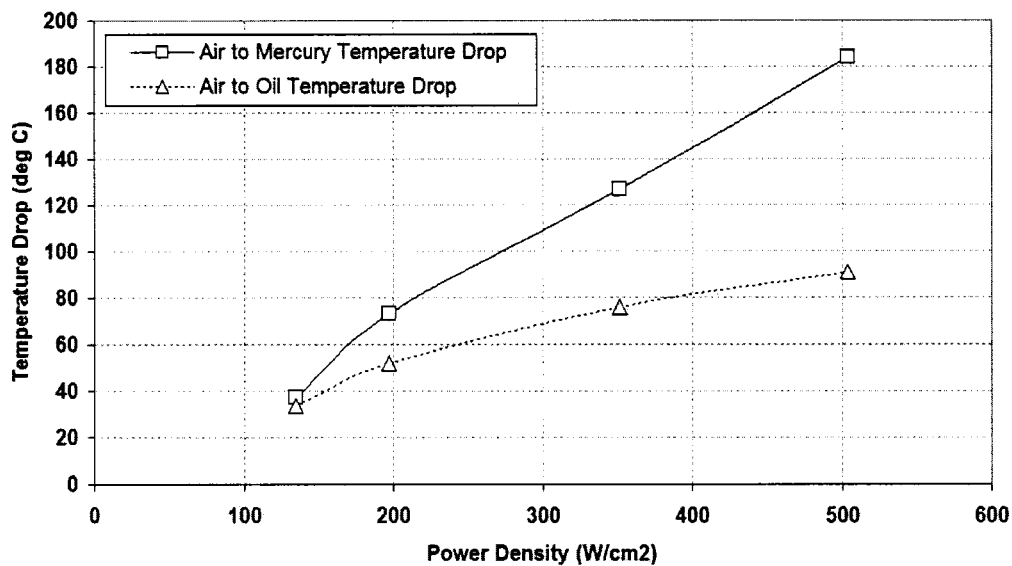
Figure 6.13: Temperature drop for the hot-spot (air-to-oil and air-to-mercury) versus heat flux density.

Figure 6.14 shows the relative heat transfer coefficients, defined by Newton's law of cooling, as calculated from the data obtained in Figure 6.13. A linear increase in heat transfer coefficient was observed for increasing hot-spot power densities. This suggests

125

that the addition of mercury droplets in oil results in improved heat transfer, which only further improves as the hot-spots becomes more intense.
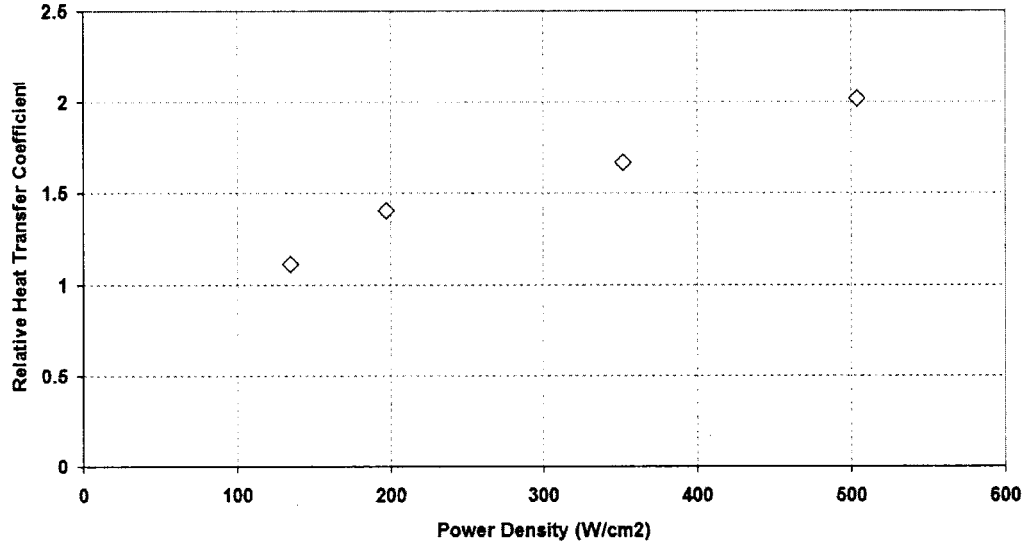
Figure 6.14: Relative heat transfer coefficient versus heat flux density.

6.4.3 Effect of Cooling Area on Heat Transfer

In the programmable thermal switch-based cooling architecture proposed in this chapter, the mechanism by which hot-spots of variable power densities are handled is the variable number of mercury droplets that are in contact with the hot-spot. A larger number of droplets would result in a larger area through which heat is transferred into the liquid metal toward a metal via which is directly connected to a heat sink. In order to characterize this correlation, we observe the temperature drop of a single hot-spot when a mercury droplet of varying sizes is applied.

A heat flux density of 133 W/cm^2 was applied to a 500μm $\times$ 500μm thin-film heater, resulting in a steady state temperature of $\sim$110°C in air and $\sim$80°C in silicone oil. The resulting hot-spot was imaged using an IR camera in order to obtain a thermal profile (see

126
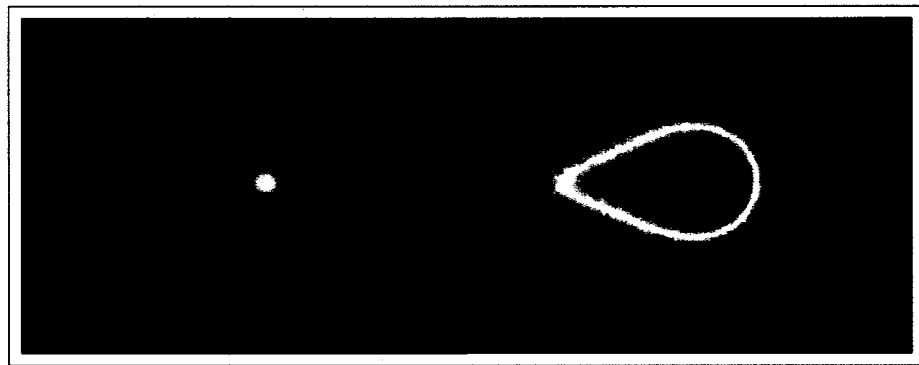
Figure 6.15).

Figure 6.15: Grayscale (left) and false-color (right) infrared image of the 500μm × 500μm hot-spot.

Using MATLAB, a one-dimensional temperature profile of the hot-spot (represented by the line drawn in Figure 6.15) was calculated. As shown in Figure 6.16, the maximum temperature of the hot-spot reached was ~85°C at the center of the hot-spot, and quickly falling off toward a steady state value of ~25°C away from the hot-spot.
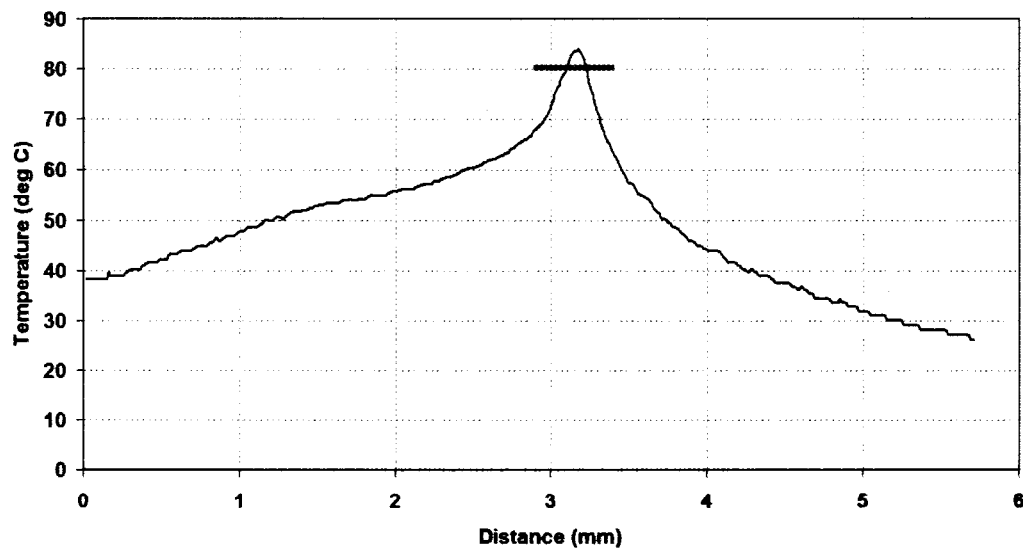
Figure 6.16: Temperature profile of the 500μm × 500μm hot-spot.

Mercury droplets of various sizes were delivered to a hot-spot with a heat flux density of 133 W/cm^2. The temperature drop of the hot-spot cooled by mercury droplets (0.5 to 4.3 mm^2 in area) was recorded and is shown in Figure 6.17.
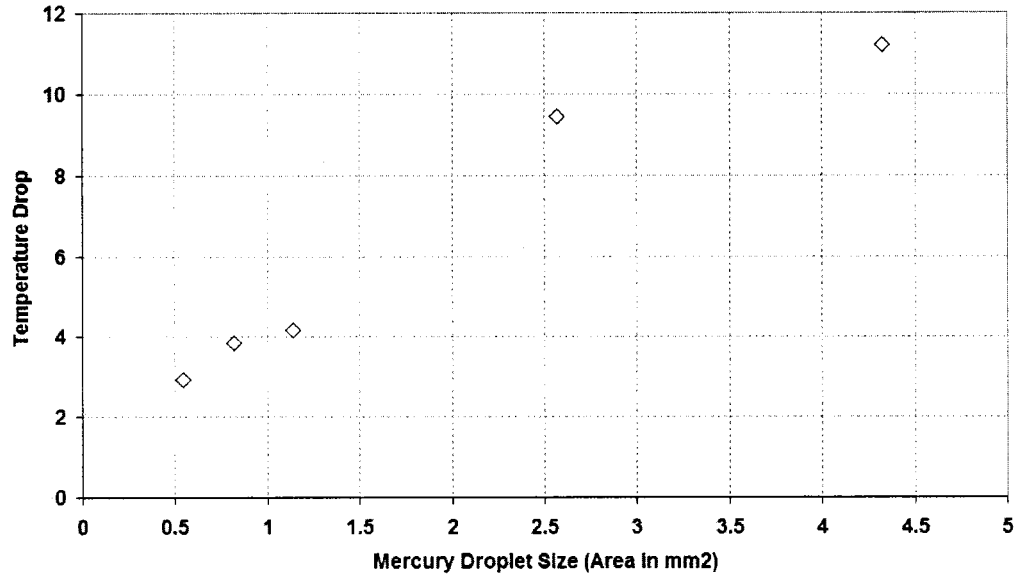
Figure 6.17: Temperature drop of the hot-spot due to the mercury droplet with respect to droplet size.

A linear increase in the temperature drop was observed for an increasing area through which the hot-spot was cooled by mercury. For example, the temperature drop increased four-fold over nearly the same increase in area. Hence, there is a strong correlation between the area cooled by the droplet and the heat transfer away from the hot-spot. This correlation can thus be used to calculate the area needed to provide the required heat transfer from a hot-spot to maintain a uniform thermal profile.

In the case of the programmable thermal switch, the required area can be provided by simply specifying the number of cells to be activated for cooling. The resolution of the area, and thus the degree of programmability, is dictated by the density of cells within the hot-spot; for example, twenty-five cells within a square millimeter allow for control over 40 μm^2, whereas four-cells within a square millimeter would allow for control over only

250 μm^2. The larger cell-size in the latter scenario might result in insufficient granularity needed to achieve a uniform thermal profile.

6.5 Chapter Summary and Conclusions

The ability to use liquid-metal droplets in a programmable thermal switch-based cooling method was studied in this chapter. Mercury was chosen as a liquid-metal candidate due to its attractive thermal and liquid properties. The actuation and transport of mercury was successfully performed using PCB-based digital microfluidic chips, and transport switching frequencies of up to 32 Hz was demonstrated. Steady-state heat transfer experiments were performed revealing large temperature differences when a mercury droplet was introduced. These temperature differences increased with the heat flux density of the hot-spot. Transient heat transfer experiments revealed that mercury droplets, regardless of size, was able to cool a hot-spot to a steady state value in less than 500ms. Cooling was enhanced in cases where the mercury droplet covered a larger footprint of the hot-spot. The presence of an underlying via also enhanced cooling, and the ability for mercury to conduct heat through the oil layer increased with higher heat-flux density. A maximum temperature drop of 80°C was observed when a 1mm diameter mercury droplet was introduced to the hot-spot.

Chapter 7

Conclusions and Future Work

7.1 Thesis Contributions

Two reconfigurable hot-spot cooling architectures based on digital microfluidic principles were designed, developed, and tested in this thesis. The first architecture relied on convective heat transfer by dispensing, transport, and recycling aqueous droplets in reconfigurable flow paths and flow rates. The second architecture relied on conductive heat transfer by the actuation of liquid metals. Due to the easy integration and compact nature of the digital microfluidic platform, the two techniques developed here enables a closed-loop IC-level cooling device that is able to detect and respond to thermal variations in the IC substrate.

7.1.1 Digital Microfluidics on PCB

One of the major contributions of this thesis lies in the development of digital microfluidic devices on printed circuit board rather than glass. The widely available PCB manufacturing process enabled rapid prototyping at a lower cost than traditional metal-on-glass vacuum processes. Furthermore, patternable insulator layers allowed us to develop a novel co-planar electrowetting scheme.

A number of design changes were made until a stable architecture was reached. These changes included the design of bare-copper grounding schemes, the filling and plating of via holes, the design of transport electrodes, and the inclusion of a surface finish. The final two-layer coplanar PCB prototype had a board thickness of 62 mils, a copper thickness of 15μm, and a patternable LPI soldermask insulator thickness of anywhere between 17 to 35 μm. Switching frequencies of up to 50 Hz was demonstrated, as well as the repeated dispensing and recycling of droplets in a closed-loop system. Actuation voltages ranged

from 125 to 300V, which was largely influenced by the LPI soldermask thickness.

The relocation of the ground contact from the top plate to the electrode plane eliminated the need for a conductive, or any, top plate. This enabled the actuation of droplets in an "open" microfluidic substrate where droplets were unconfined by a top plate. The transport and rapid mixing of droplets were successfully demonstrated, where transport speeds up to 50Hz and mixing times of 1.8s for two 6μl droplets were achieved. The flexibility in design afforded by this coplanar and open structure could facilitate novel applications not just in chip cooling, but in areas of clinical diagnostics and lab-on-a-chip.

7.1.2 Thermal Effects on Droplet Transport

The temperature effects on transport of droplets in both oil and air in a digital microfluidic system were studied. In cases where the entire system was heated, a significant drop in minimum actuation voltages (V_{th}) required for the oscillation of microliter-sized droplets in oil was observed, which, given a constant actuation voltage, is synonymous to increased droplet velocities. This increased flow rate at higher temperature makes this platform amenable for chip cooling applications where temperatures above 25°C are required.

Interfacial tension and oil viscosities were investigated as possible mechanisms for this behavior. The reduction of interfacial tension alone with elevated temperatures plays a negligible role in the reduction of V_{th}, while the lowered viscosity of the surrounding oil accounts for nearly all the changes observed. For droplets actuated in air, where filler fluid viscosity changes are no longer present, a significant increase in V_{th} was observed. It is believed that a decrease in contact angle at elevated temperature causes a reduction in the contact-angle gradient which drives the motion of the droplet, requiring larger voltages to actuate them.

7.1.3 Flow-through Based Cooling

The ability to program the flow of droplets to cool hot-spots in both an open and closed system was demonstrated for the first time, and parameters affecting heat-transfer such as droplet aspect ratio, absolute volumes, hot-spot power densities, and the presence of a filler fluid were investigated. It was found that, in general, parameters that increased the mass flow rate, such as the absolute size of the droplet and transport speeds, exhibited significantly higher heat transfer characteristics. Larger droplets with higher residence frequencies were thus able to cool hot-spots better than smaller droplets with lower residence frequencies. The highest cooling was observed in a system where 6 μl droplets were transported in an open system. The worst cooling was observed in a system where a 50 nL droplet was transported in a closed system with a droplet height of 100 μm. Cooling was found to increase as the power densities of the hot-spots increased, which is the result of the increased temperature differential between the droplet and the hot-spot. Droplet motion did not appear to be impeded by the thermal gradients generated by the hot-spot.

In the presence of a background heat flux, the ability for droplets to cool hot-spots was worsened. The temperature of the droplet appeared to rapidly equilibrate with the temperature of the surrounding oil. This suggests that, given an insufficient transport speed, the droplet would already have experienced its maximum heat capacity by the time it reached the hot-spot. Hence, droplets must be transported at very high speeds to avoid overheating.

7.1.4 Programmable Thermal Switch Based Cooling

We explored the possibility of using electrowetting to create a programmable thermal switch, whereby a liquid-metal based droplet can be manipulated such that an area in the cooling device can be selectively switched from a low thermal conductivity mode to a high thermal conductivity mode. The is different from the flow-through based cooling method studied in Chapter 5 which exploited the ability for droplets to move in reconfigurable flow

paths and flow rates using electrowetting-based actuation.

Mercury was chosen as a liquid-metal candidate due to its attractive thermal and liquid properties. The actuation and transport of mercury was successfully performed using PCB-based digital microfluidic chips, and transport switching frequencies of up to 32 Hz was demonstrated. Steady state heat transfer experiments were performed revealing large temperature differences when a mercury droplet was introduced. These temperature differences increased with the heat flux density of the hot-spot. Transient heat transfer experiments revealed that mercury droplets, regardless of size, was able to cool a hot-spot to a steady state value in less than 500ms. Cooling was enhanced in cases where the mercury droplet covered a larger footprint of the hot-spot. The presence of an underlying via also enhanced cooling, and the ability for mercury to conduct heat through the oil layer increased with higher heat-flux density. A maximum temperature drop of 80°C was observed when a 1mm diameter mercury droplet was introduced to the hot-spot.

7.2 Future Work

For both the flow-through and thermal-switch-based cooling strategies presented in this thesis, there are a number of issues that need to be addressed in order to realize adaptive hot-spot cooling in a real system.

7.2.1 Flow-Through Based Cooling

While the ability for droplets to cool hot-spots has been successfully demonstrated, the heat transfer parameters studied in Chapter 5 suggest that, for actual systems with nanoliter volumes and high heat-flux densities, droplets must be transported at speeds well above the limits of our current prototype. Transport speeds can be greatly improved by investigating alternative dielectrics used to insulate the electrodes from the droplet. The LPI soldermask used in these studies exhibit contact angle saturation, charging, and dielectric breakdown

Dielectric	Chemical Formula	Dielectric Constant (k)
Halfnium Oxide	HfO_2	25
Halfnium Silicate	$HfSiO_4$	15-18
Tantalum Pentoixde	HfO_2	25
Titanium Oxide	TiO_3	20-85
Zirconium Oxide	ZrO_2	20-25
Zirconium Silicate	$ZrSiO_4$	15

Table 7.1: Dielectric constants of high-k materials.

when larger driving voltages are used to increase the droplet transport speeds. However, a wide range of dielectrics have not yet been tested which could significantly increase the maximum attainable droplet speed, thus satisfying the requirements for flow-through based droplet cooling in current and future IC devices.

An ideal dielectric to be used as the insulator material would have to have a high dielectric strength, be easily deposited pin-hole free, and would be resistent to charging effects. Parylene C, which is typically used for glass-based digital microfluidic chips, has a dielectric constant of $k = 3.15$. Silicon Dioxide (SiO_2), which has also been used for digital microfluidic devices, has a similar dielectric constant of $k = 3.9$. The operating voltages for these devices are typically in the 10's of volts range.

Much higher k dielectric materials include Tantalum Pentoxide (Ta_2O_5), Halfnium Oxide (HfO_2), and Titanium Oxide (TiO_3). Table 7.2.1 shows a complete list of high k dielectrics that should be tested as an insulator in digital microfluidic devices. The operating voltages for these devices should be equivalent to <10V range for a droplet transport frequency of 50 Hz. Larger voltages can drive the droplet transport frequencies into the 100's of Hz range, achieving the flow rates necessary for sufficient cooling of current IC substrates.

To increase the thermal conductivity of the system, digital microfluidic chips could be manufactured on silicon substrates, or possibly integrated with the IC design. The use of silicon, due to its very high thermal conductivity, would allow for the most efficient

heat transfer into the cooling droplets and surrounding oil, resulting in much higher heat transfer. The use of this method would thus be similar to those used in continuous-flow cooling devices, yet still allow for the reconfigurability of flow necessary for adaptive hot-spot cooling.

7.2.2 Programmable Thermal Switch-Based Cooling

While the feasibility of using liquid metals as a programmable thermal switch was demonstrated in this thesis, a prototype chip needs to be developed which will allow programmability of liquid metal droplets to act as a reconfigurable thermal conductance layer. Thus far, only mercury has been tested a possible candidate for the liquid metal material, but other metals such as Gallium alloys should be tested as well. Since the properties, such as viscosity, of these liquid metals vary with temperature, it is important to keep in mind that operating temperatures in cooling applications may be well above room temperature. Thus, testing of these alloys should be performed at various ambient temperatures.

Expanded View   **Assembled View**

Silicon Top Plate
with integrated heaters

Digital Microfluidic Chip
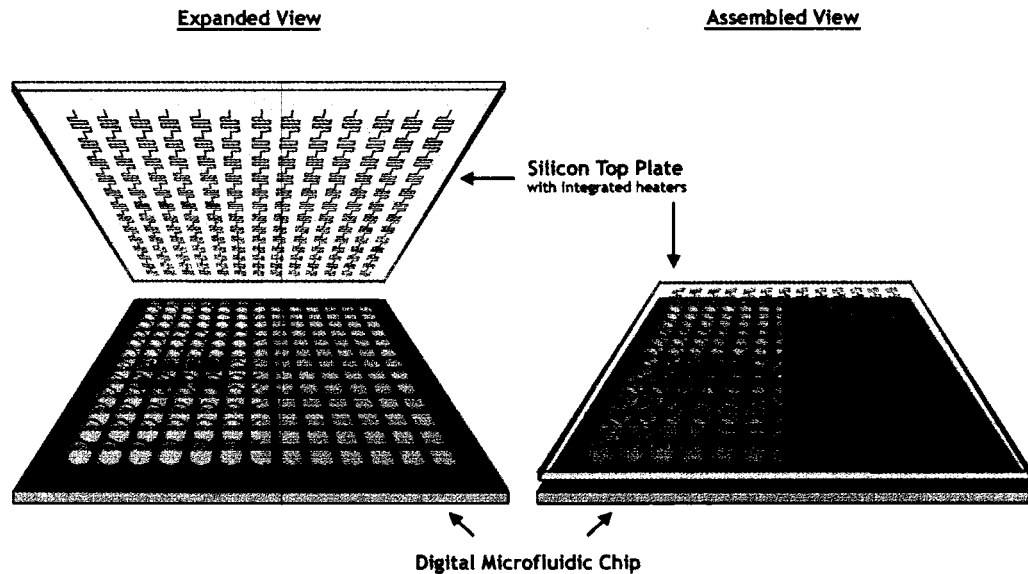
Figure 7.1: Conceptual schematic of a adaptive hot-spot cooling prototype designed for programmable thermal switch-based cooling.

For mercury, large driving voltages are needed for the necessary contact angle changes required to cause the mercury droplet to attach and detach from the target IC substrate. Thus, alternative dielectrics must be explored as well. Several candidates for high-k dielectric materials is shown in Table 7.2.1.

For PCB-based digital microfluidic chips, the vias through which electrical contacts to the electrodes should be filled with a thermal conductive material. Conductive epoxies or thicker plating of the vias would allow for an increased thermal conductivity between the liquid-metal droplet and the attached heat sink.

A prototype of a possible adaptive hot-spot cooling design is shown in Figure 7.1. The digital microfluidic chip consists of an m × n array of electrodes upon which a liquid-metal droplet sits. Since a densely packed array of electrodes is required in this thermal switch-based system, a four-layer PCB process must be used in order route the electrical connections to each electrode. Affixed to the bottom of the digital microfluidic chip is a heat-sink (e.g. peltier cooler or a heat-sink-fan). This provides the chip with a constant heat flux out of the system.

A corresponding silicon top plate (either the actual IC chip or a thermal test chip) is aligned with the chip such that an array of RTDs covers each liquid-metal droplet. Depending on the thermal profile of the silicon top plate (as read from the RTDs or viewed from an IR camera), the liquid-metal droplets are actuated such that the hottest area of the top plate is in contact with the liquid-metal droplets (droplets are not actuated), and the cooler areas of the top plate are are not in contact with the droplets (droplets are actuated). Parameters such as aspect ratio, droplet volume, array density, and surrounding filler fluid should be investigated to optimize the uniformity in the resulting temperature profile of the top plate.

7.2.3 IC Level Implementation

The prototypes discussed in this thesis were designed on PCB processes not suitable for IC level implementation. The concepts discussed here will eventually be integrated with the IC process whereby electrodes, reservoirs, and insulator are to be fabricated either on the IC substrate itself, or on a separate silicon substrate which is subsequently wafer bonded with the target IC. While the micro-fabrication of digital microfluidic devices has been shown successfully using chrome-on-glass, the transition into metal-on-silicon should be explored. Once a process has been establish, a method for integrating RTDs on the IC should be explored. Successful demonstration of these IC-level processing steps would thus result in a truly integrated adaptive hot-spot cooling platform.

Appendix A

Image Analysis Software

A MATLAB program was written in order to facilitate measuring the temperatures from collected video files. It allows one to read a video file, presumably captured from an infrared camera, and peruse through each frame within that video file. One can then select the range of frames to video process. The program is shown in Figure A.1.
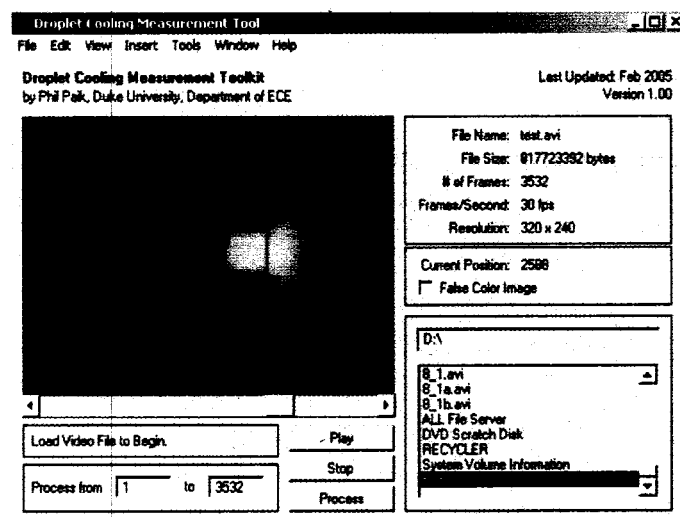
Figure A.1: Screen capture of the Droplet Cooling Measurement Tool showing the thermal profile of an array of electrodes (whitehot).

False color can be enabled to more easily see temperature gradients. Figure A.2 is the same image, only with false color.

Video processing allows you to select an arbitrary region within the video window, and calculate the average temperature within that region. It processes every frame, and outputs the results to a file. At the end of the program, it plots the data in a figure. An example is shown in Figure A.3.

138
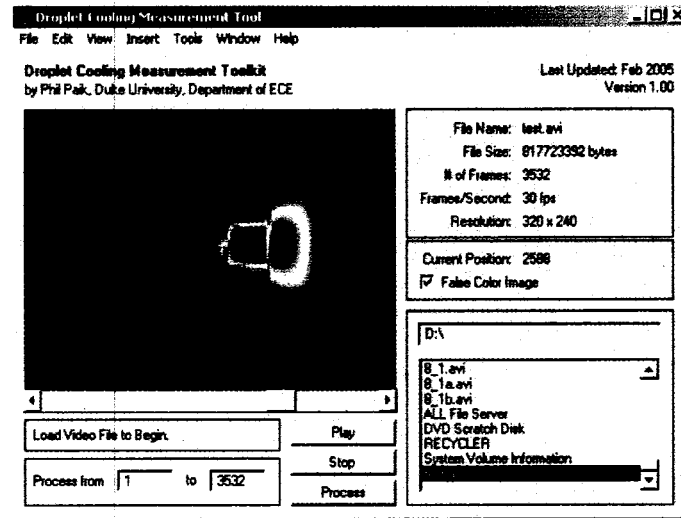
Figure A.2: Screen capture of the Droplet Cooling Measurement Tool showing the thermal profile of an array of electrodes (false color).
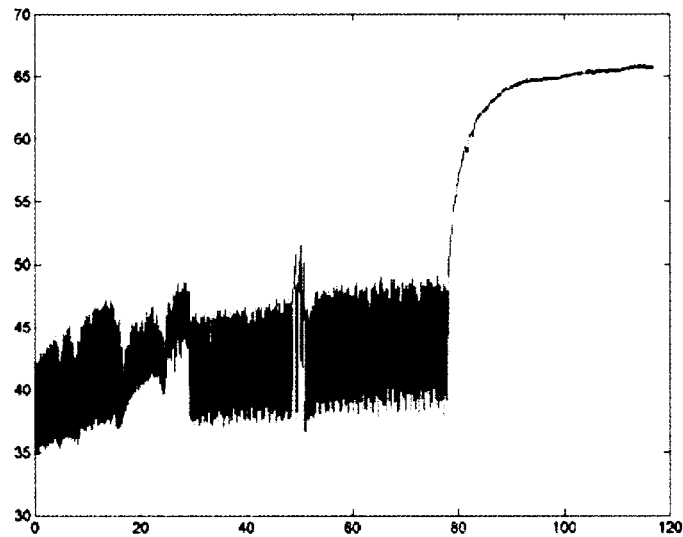
Figure A.3: Screen capture of the Droplet Cooling Measurement Tool showing the thermal profile of an array of electrodes (false color).

The area selected in this example is the center electrode, which oscillates between 35 and 45°C when a droplet is passed over it (where the droplet is moving at a switching frequency of 34 Hz). Because of interference of the droplet as it passes over the target electrode, we cannot say that the heater actually reaches 35°C. Instead, we must say that at worst, the heater reaches 45°C. This is still a good improvement over the temperature of the target electrode in the absence of an oscillating droplet, which is about 65°C.

Appendix B

Microfluidic Chip Reference

B.1   PCB-R000A Chip Design
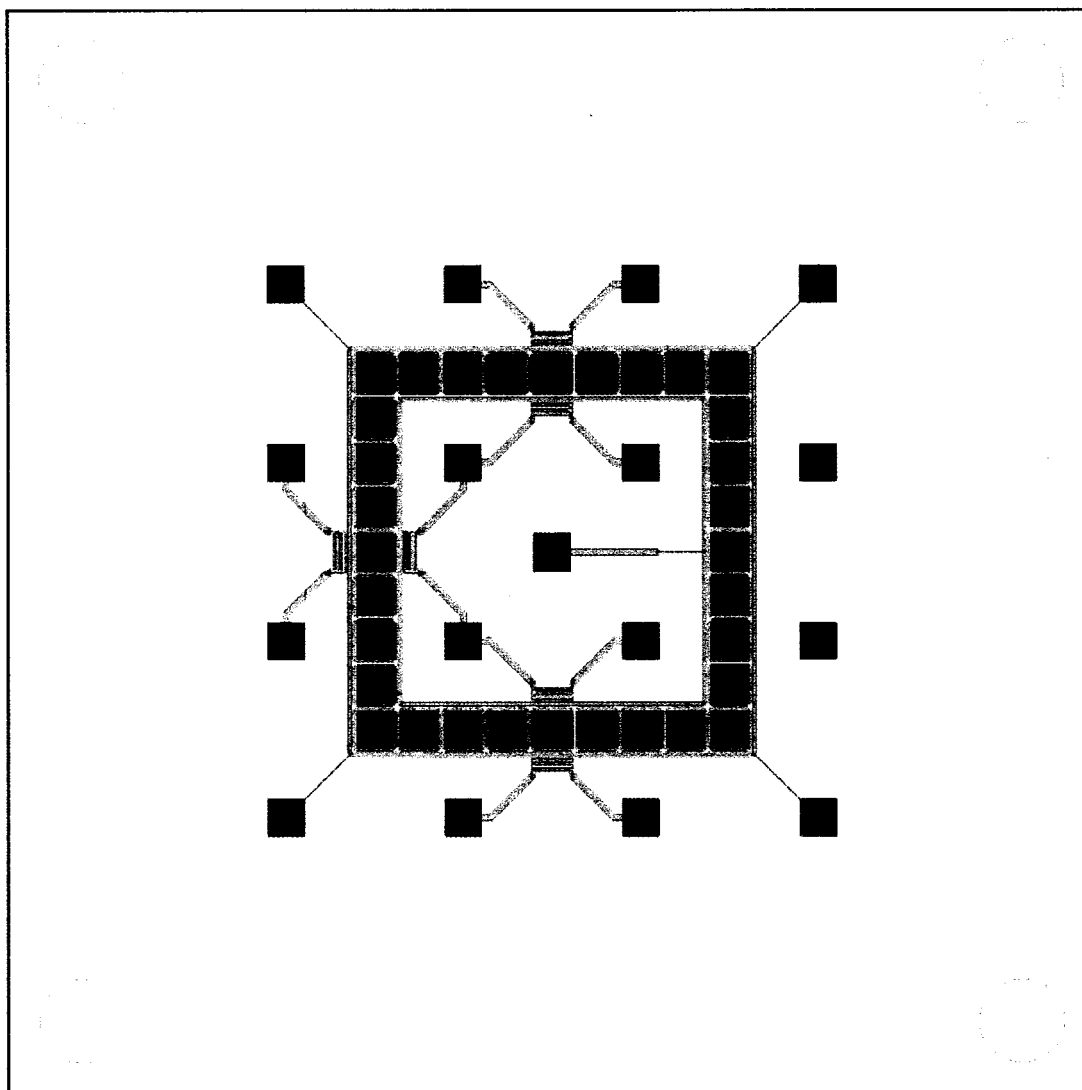
Figure B.1: First generation hot-spot cooling digital microfluidic chip. In this design, copper heaters were placed adjacent to the electrodes in the center of each side.

141
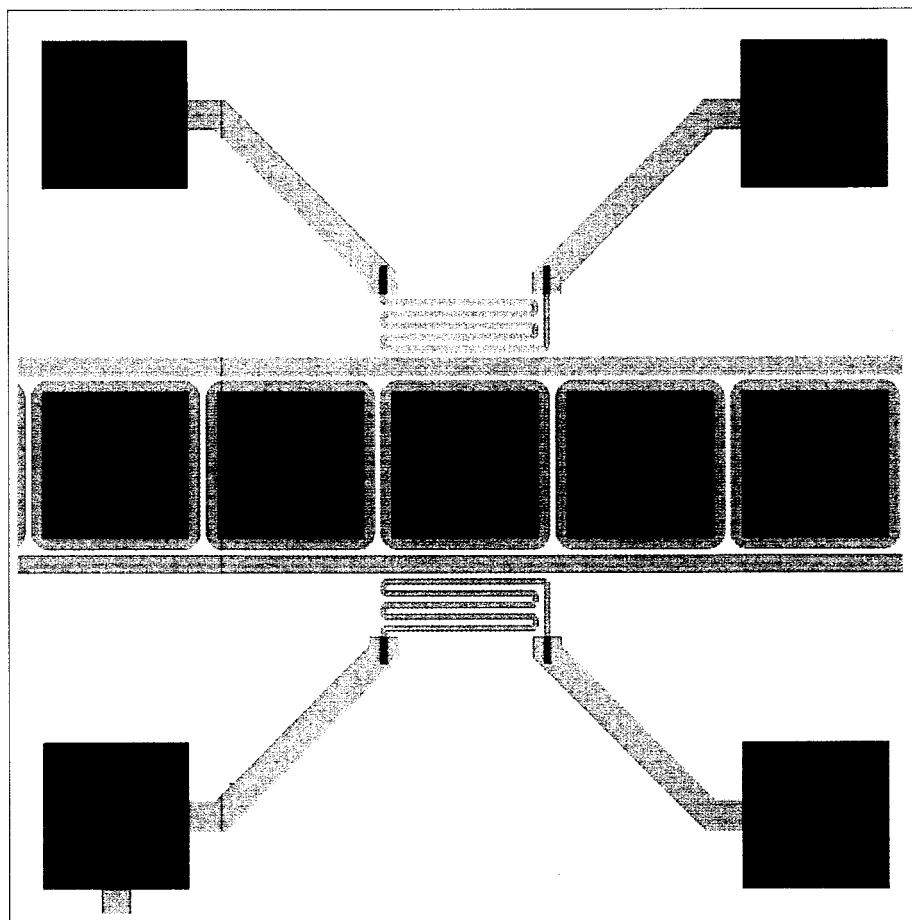
Figure B.2: Close-up view of the copper heaters.

142

B.2   PCB-R000D Chip Design
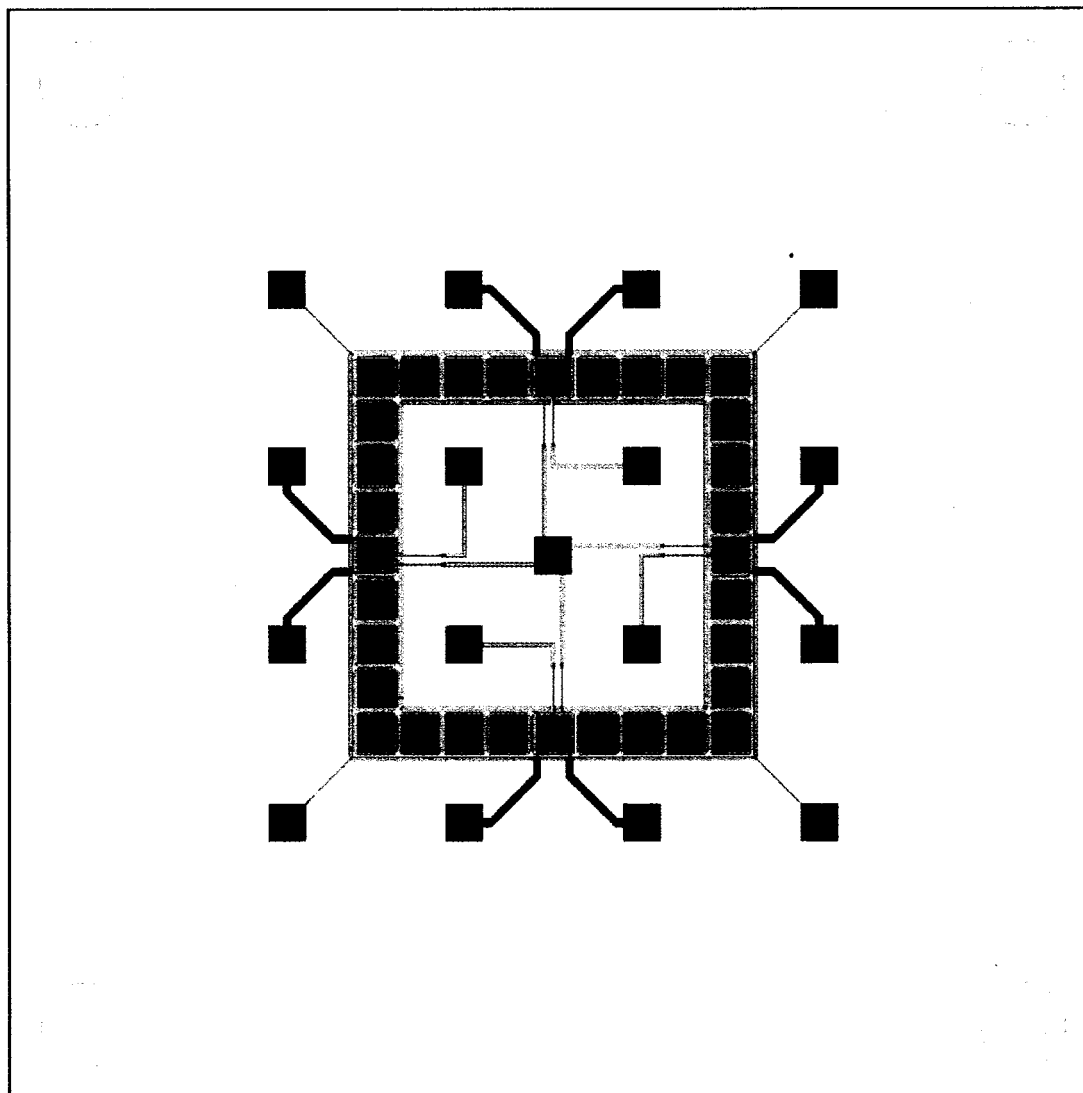
Figure B.3: First generation hot-spot cooling digital microfluidic chip. In this design, copper heaters were placed on the backside of the chip centered on an electrode.
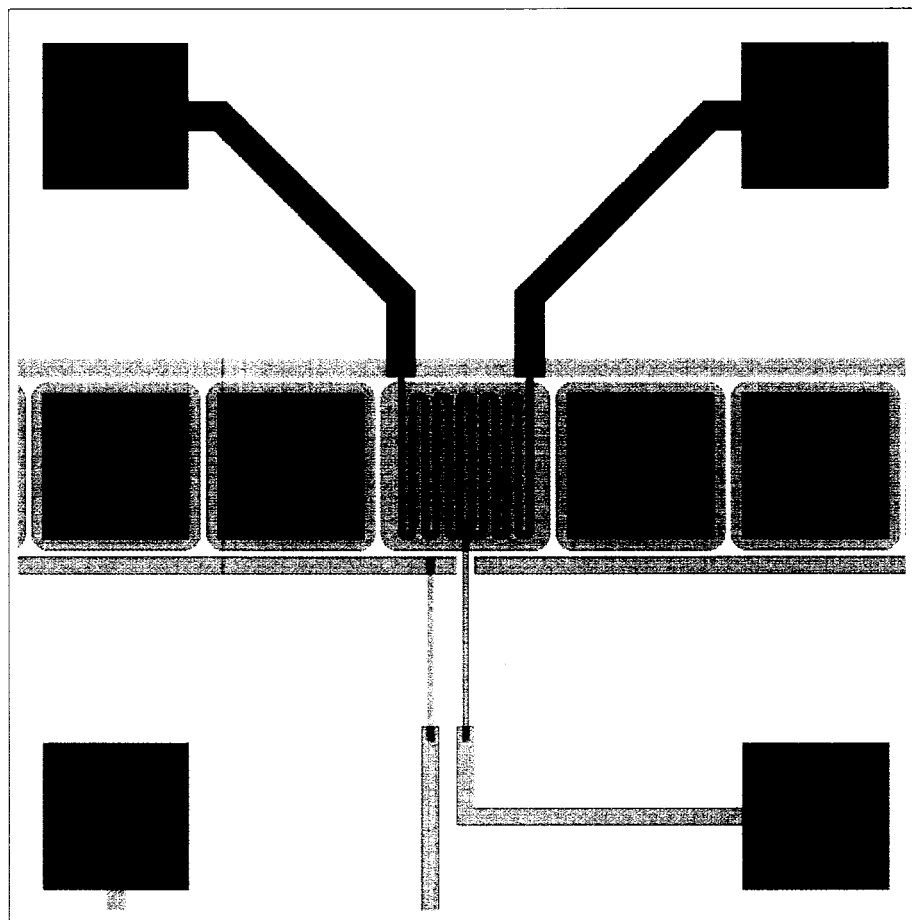
Figure B.4: Close-up view of the copper heaters.

144

B.3   PCB-R005 TM-01 Chip Design
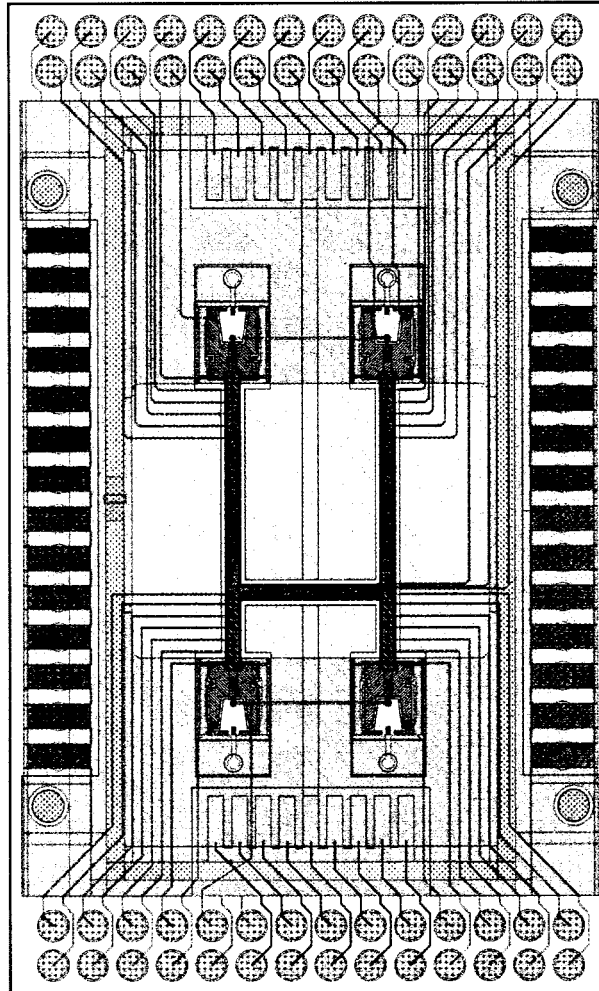
Figure B.5: Sixth generation hot-spot cooling digital microfluidic chip. In this design, four reservoirs are connected to an array of electrodes. This chip is to be used in conjunction with the RTD-001 top plate.
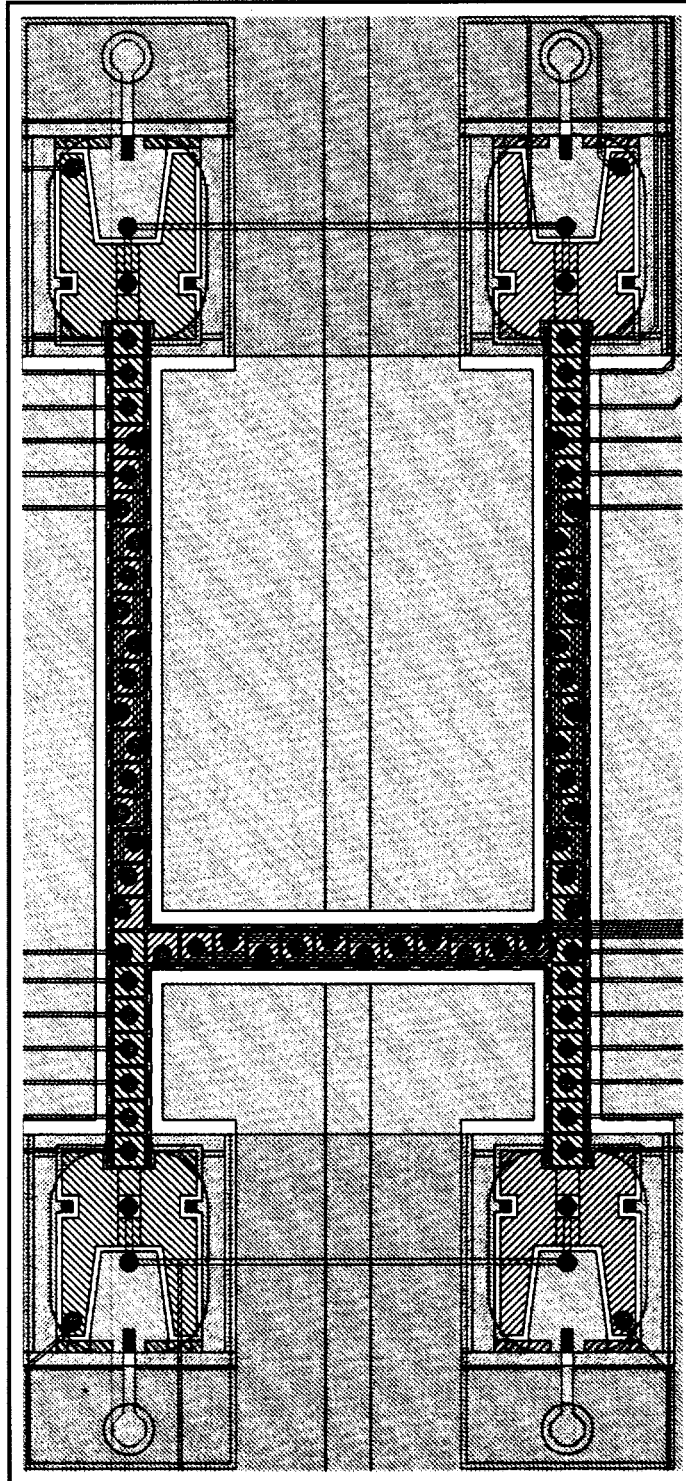
Figure B.6: Close-up view of the active area.

146

B.4   PCB-R005 TM-02 Chip Design
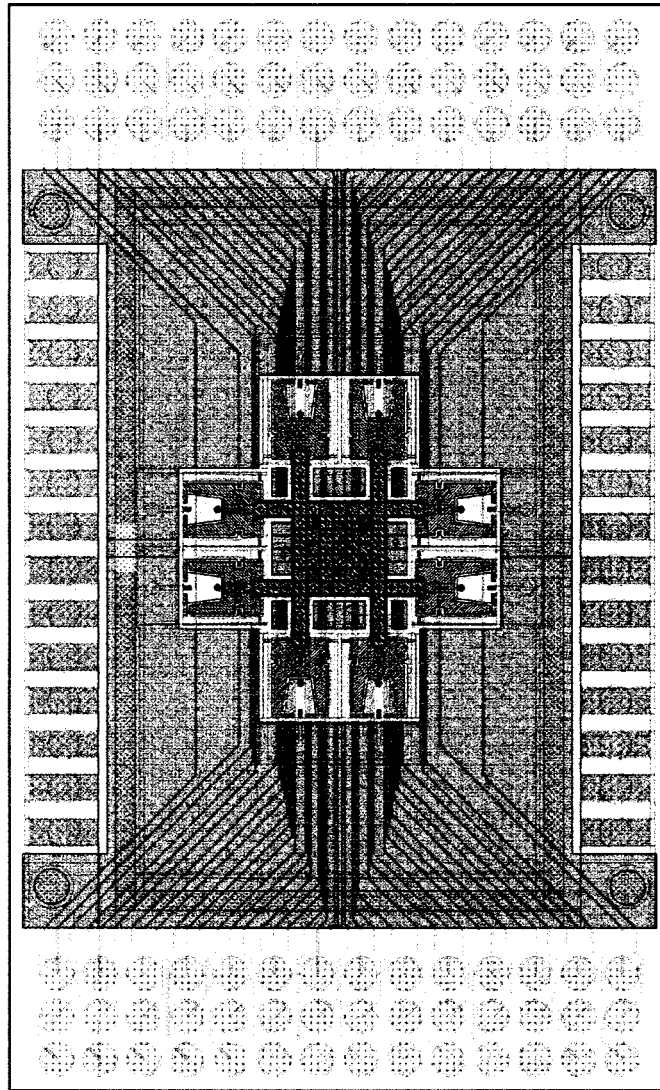
Figure B.7: Sixth generation hot-spot cooling digital microfluidic chip. In this design, eight reservoirs are connected to two-dimensional array of electrodes, enabling droplet recycling. This chip is to be used in conjunction with the RTD-003 top plate.
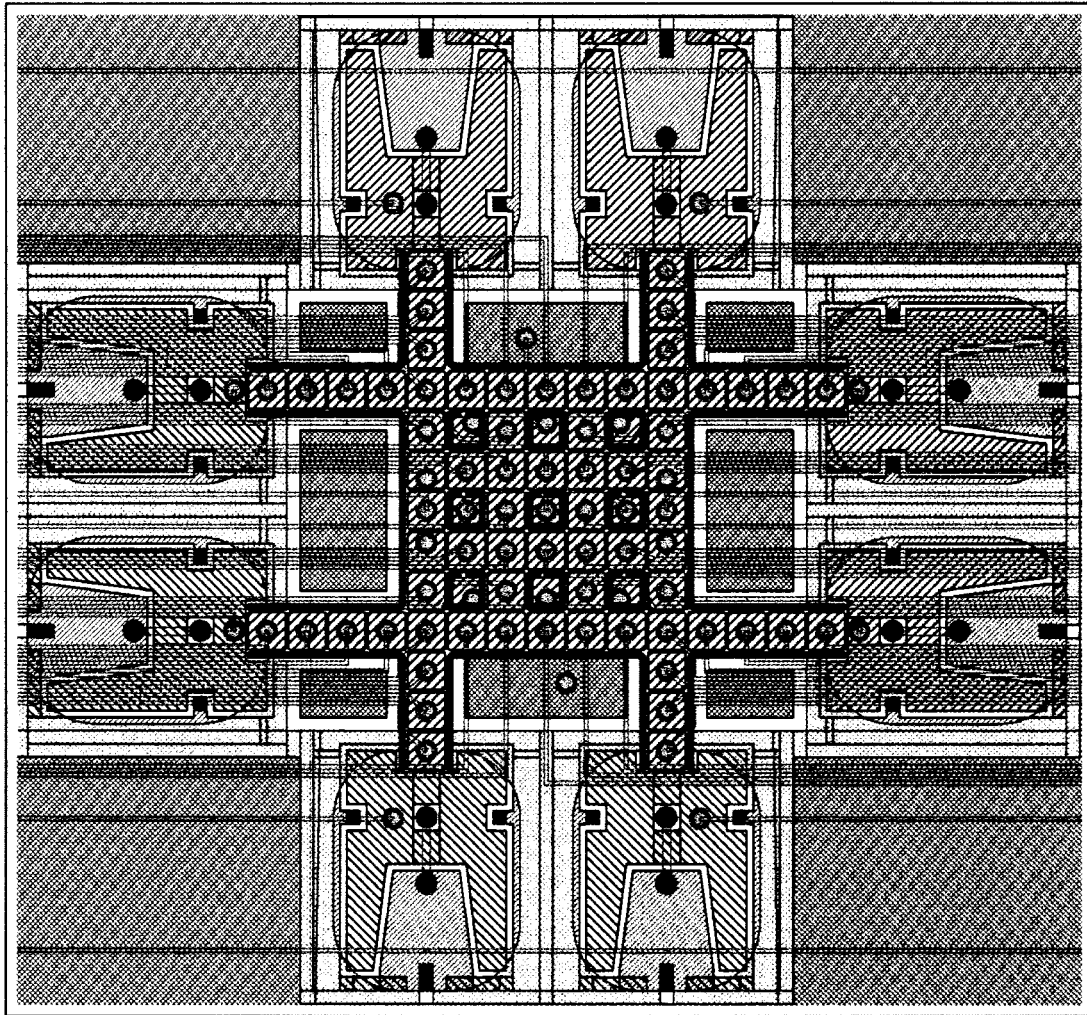
Figure B.8: Close-up view of the active area.

Appendix C

RTD/Heater Top Plate Reference

C.1 RTD-001 Top Plate Design
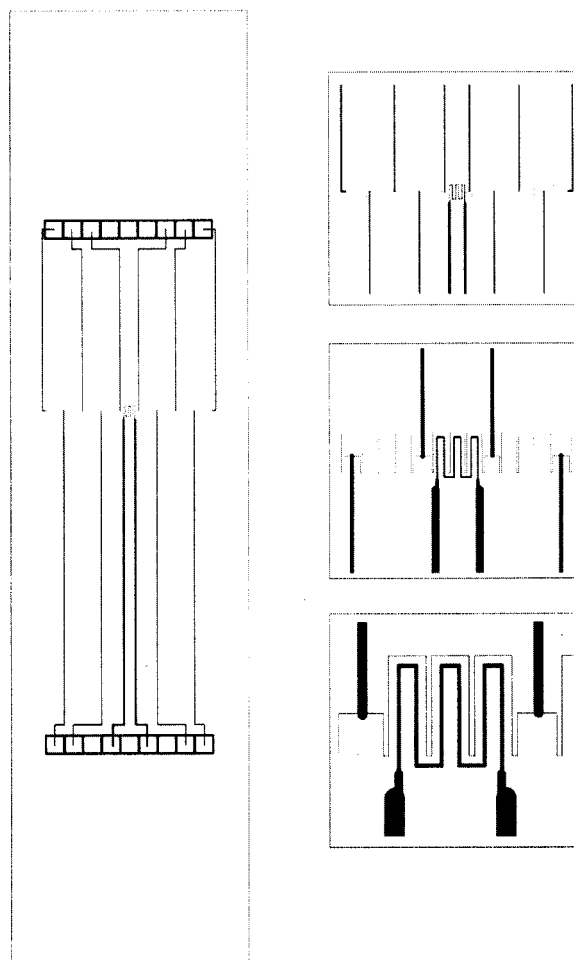
Figure C.1: First generation top plate used to simulate a hot-spot and obtain temperature measurements. These top plates are used in conjunction with either PCB-R000 or PCB-R005 TM-01 chips.

C.2 RTD-003 Top Plate Design
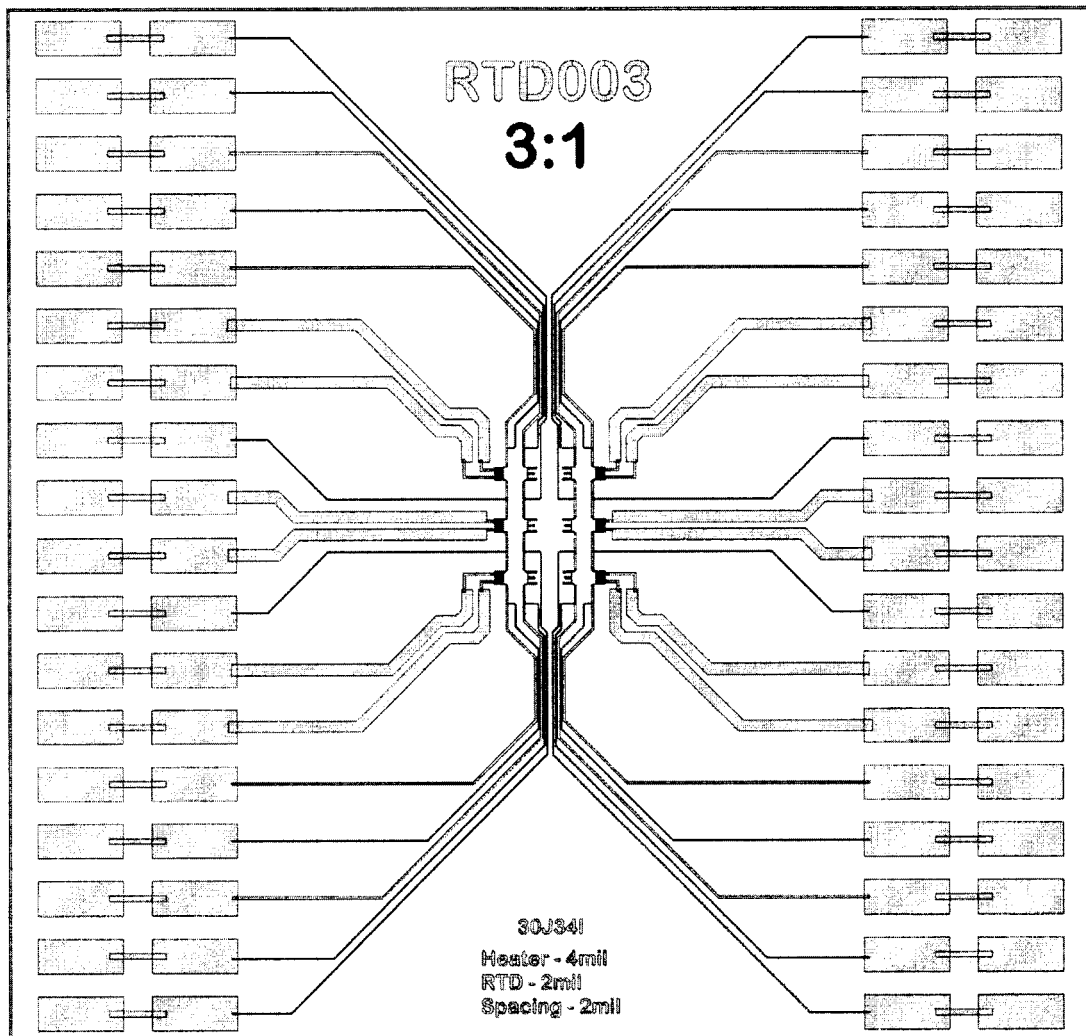
Figure C.2: Third generation top plate used to simulate a hot-spot and obtain temperature measurements. These top plates are used in conjunction with PCB-R005 TM-02 chips.
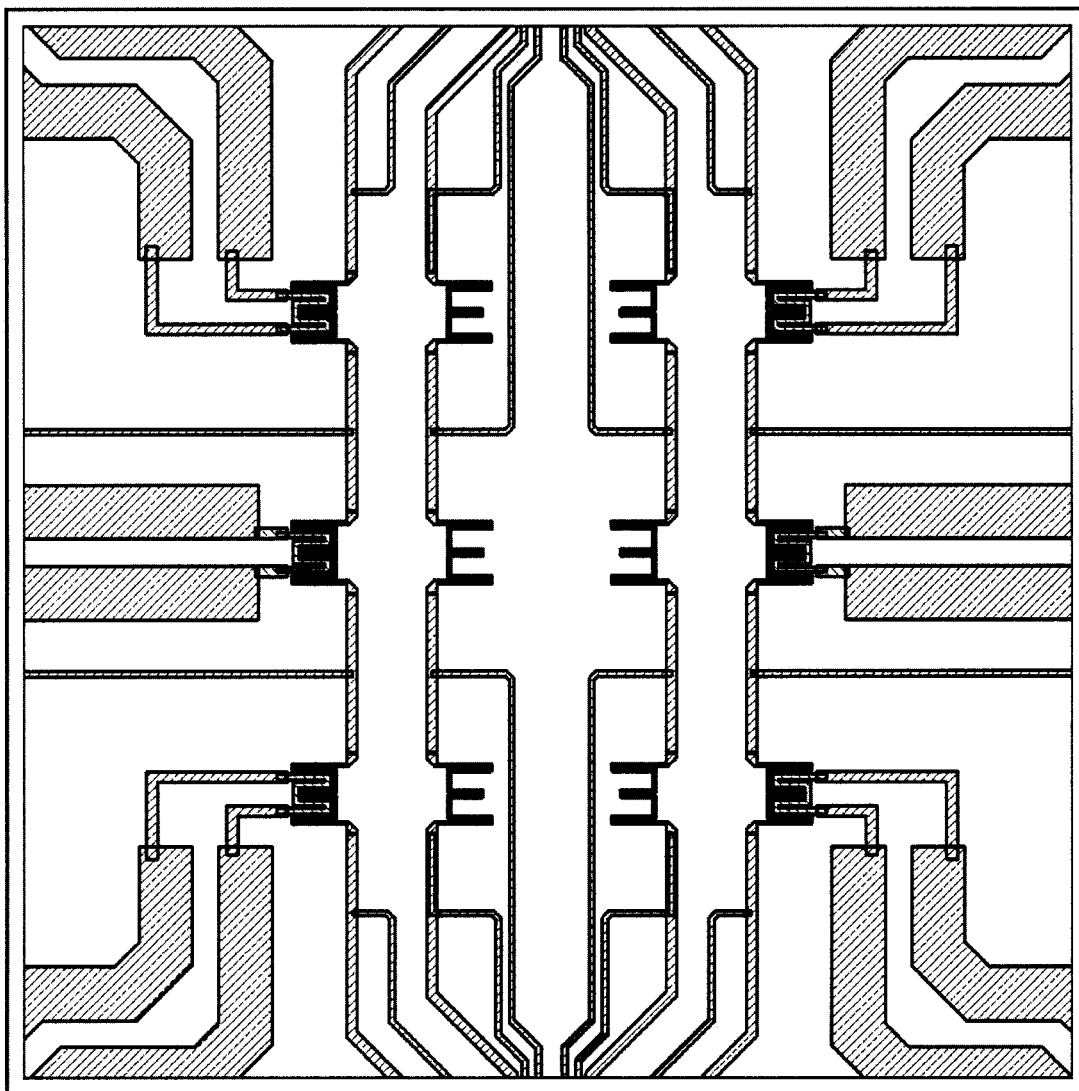
Figure C.3: Close-up view of the thin-film heaters and RTDs.

Appendix D

Material Safety Data Sheet for Mercury

The following information is selected information from the Material Safety Data Sheet for mercury as obtained from J.T. Baker Chemicals (Phillipsburg, NJ).

D.1   Product Identification

Synonyms: Quicksilver; hydrargyrum; Liquid Silver

CAS No.: 7439-97-6

Molecular Weight: 200.59

Chemical Formula: Hg

Product Codes: J.T. Baker: 2564, 2567, 2569

Mallinckrodt: 1278, 1280, 1288

D.2   Hazards Identification

D.2.1   Potential Health Effects

Inhalation: Mercury vapor is highly toxic via this route. Causes severe respiratory tract damage. Symptoms include sore throat, coughing, pain, tightness in chest, breathing difficulties, shortness of breath, headache, muscle weakness, anorexia, gastrointestinal disturbance, ringing in the ear, liver changes, fever, bronchitis and pneumonitis. Can be absorbed through inhalation with symptoms similar to ingestion.

Ingestion: May cause burning of the mouth and pharynx, abdominal pain, vomiting, corrosive ulceration, bloody diarrhea. May be followed by a rapid and weak pulse, shallow

152

breathing, paleness, exhaustion, tremors and collapse. Delayed death may occur from renal failure. Gastrointenstinal uptake of mercury is less than 5

Skin Contact: Causes irritaton and burns to skin. Symptoms include redness and pain. May cause skin allergy and sensitization. Can be absorbed through the skin with symptoms to parallel ingestion.

Eye Contact: Causes irritation and burns to eyes. Symptoms include redness, pain, blurred vision; may cause serious and permanent eye damage.

Chronic Exposure: Chronic exposure through any route can produce central nervous system damage. May cause muscle tremors, personality and behavior changes, memory loss, metallic taste, loosening of the teeth, digestive disorders, skin rashes, brain damage and kidney damage. Can cause skin allergies and accumulate in the body. Repeated skin contact can cause the skin to turn gray in color. A suspected reproductive hazard; may damage the developing fetus and decrease fertility in males and females. Aggravation of Pre-existing Conditions: Persons with nervous disorders, or impaired kidney or respiratory function, or a history of allergies or a known sensitization to mercury may be more susceptible to the effects of the substance.

D.3   First Aid Measures

Inhalation: Remove to fresh air. If not breathing, give artificial respiration. If breathing is difficult, give oxygen. Get medical attention immediately.

Ingestion: Induce vomiting immediately as directed by medical personnel. Never give anything by mouth to an unconscious person. Get medical attention immediately.

Skin Contact: Immediately flush skin with plenty of water for at least 15 minutes while removing contaminated clothing and shoes. Get medical attention immediately. Wash clothing before reuse. Thoroughly clean shoes before reuse.

Eye Contact: Immediately flush eyes with plenty of water for at least 15 minutes, lifting

lower and upper eyelids occasionally. Get medical attention immediately.

D.4   Fire Fighting Measures

Fire: Not considered to be a fire hazard.

Explosion: Not considered to be an explosion hazard.

Fire Extinguishing Media: Use any means suitable for extinguishing surrounding fire. Do not allow water runoff to enter sewers or waterways.

Special Information: In the event of a fire, wear full protective clothing and NIOSH-approved self-contained breathing apparatus with full facepiece operated in the pressure demand or other positive pressure mode. Undergoes hazardous reactions in the presence of heat and sparks or ignition. Smoke may contain toxic mercury or mercuric oxide. Smoke may contain toxic mercury or mercuric oxide.

D.5   Accidental Release Measures

Ventilate area of leak or spill. Clean-up personnel require protective clothing and respiratory protection from vapor.

Spills: Pick up and place in a suitable container for reclamation or disposal in a method that does not generate misting. Sprinkle area with sulfur or calcium polysulfide to suppress mercury. Do not flush to sewer. US Regulations (CERCLA) require reporting spills and releases to soil, water and air in excess of reportable quantities. The toll free number for the US Coast Guard National Response Center is (800) 424-8802. J. T. Baker CINNASORB and RESISORB are recommended for spills of this product.

D.6 Handling and Storage

Keep in a tightly closed container, stored in a cool, dry, ventilated area. Protect against physical damage. Isolate from any source of heat or ignition. Do not use or store on porous work surfaces (wood, unsealed concrete, etc.). Follow strict hygiene practices. Containers of this material may be hazardous when empty since they retain product residues (vapors, liquid); observe all warnings and precautions listed for the product.

D.7 Exposure Controls/Personal Protection

D.7.1 Airborne Exposure Limits:

- OSHA Acceptable Ceiling Concentration:

mercury and mercury compounds: 0.1 mg/m3 (TWA), skin

- ACGIH Threshold Limit Value (TLV):

inorganic and metallic mercury, as Hg: 0.025 mg/m3 (TWA) skin, A4 Not classifiable as a human carcinogen.

- ACGIH Biological Exposure Indices:

total inorganic mercury in urine (preshift): 35 ug/g creatinine; total inorganic mercury in blood (end of shift): 15 ug/l.

D.7.2 Ventilation System:

A system of local and/or general exhaust is recommended to keep employee exposures below the Airborne Exposure Limits. Local exhaust ventilation is generally preferred because it can control the emissions of the contaminant at its source, preventing dispersion of

it into the general work area. Please refer to the ACGIH document, Industrial Ventilation, A Manual of Recommended Practices, most recent edition, for details. Personal Respirators (NIOSH Approved): If the exposure limit is exceeded and engineering controls are not feasible, a half-face respirator with a mercury vapor or chlorine gas cartridge may be worn for up to ten times the exposure limit or the maximum use concentration specified by the appropriate regulatory agency or respirator supplier, whichever is lowest. A full-face piece respirator with a mercury vapor or chlorine gas cartridge may be worn up to 50 times the exposure limit, or the maximum use concentraiton specified by the appropriate regulatory agency or respirator supplier, whichever is lowest. For emergencies or instances where the exposure levels are not known, use a full-face piece positive-pressure, air-supplied respirator. WARNING: Air-purifying respirators do not protect workers in oxygen-deficient atmospheres.

D.7.3 Skin Protection:

Wear impervious protective clothing, including boots, gloves, lab coat, apron or coveralls, as appropriate, to prevent skin contact. Eye Protection: Use chemical safety goggles and/or a full face shield where splashing is possible. Maintain eye wash fountain and quick-drench facilities in work area.

D.8 Physical and Chemical Properties

Appearance: Silver-white, heavy, mobile, liquid metal.

Odor: Odorless.

Solubility: Insoluble in water.

Density: 13.55

pH: No information found.

Volatiles by volume @ 21C (70F): 100

Boiling Point: 356.7C (675F)

Melting Point: -38.87C (-38F)

Vapor Density (Air=1): 7.0

Vapor Pressure (mm Hg): 0.0018 @ 25C (77F)

Evaporation Rate (BuAc=1): 4

D.9   Stability and Reactivity

Stability: Stable under ordinary conditions of use and storage.

Hazardous Decomposition Products: At high temperatures, vaporizes to form extremely toxic fumes.

Hazardous Polymerization: Will not occur.

Incompatibilities: Acetylenes, ammonia, ethylene oxide, chlorine dioxide, azides, metal oxides, methyl silane, lithium, rubidium, oxygen, strong oxidants, metal carbonyls.

Conditions to Avoid: Heat, flames, ignition sources, metal surfaces and incompatibles.

D.10   Toxicological Information

Toxicological Data: Investigated as a tumorigen, mutagen, reproductive effector.

Reproductive Toxicity: All forms of mercury can cross the placenta to the fetus, but most of what is known has been learned from experimental animals. See Chronic Health Hazards.

Carcinogenicity: EPA / IRIS classification: Group D1 - Not classifiable as a human carcinogen.

Bibliography

[1] J.S. Campbell Jr., W.Z. Black, A. Glezer, and J.G. Hartley. Thermal management of a laptop computer with synthetic air microjets. *International Conference on Thermal, Mechanics, and Thermomechanical Phenomena in Electronic Systems (ITHERM)*, pages 43–50, 1998.

[2] S. Wu, J. Mai, Y.C. Tai, and C.M. Ho. Micro heat exchanger by using mems imping-ing jets. *Proceedings of the IEEE MEMS Conference*, pages 171–176, 1999.

[3] J.S. Go, S.J. Kim, G. Lim, H. Yun, J. Lee, I .Song, and Y.E. Pak. Heat transfer enhancement using flow-induced vibration of a microfin array. *Sensors and Actuators A*, 90:232–239, 2001.

[4] S. Mukherjee and I. Mudawar. Smart pumpless loop for micro-channel electronic cooling using flat and enhanced surfaces. *IEEE Transactions on Components and Packaging Technologies*, 26:99–109, 2003.

[5] L. Jiang, J. Mikkelsen, J. M. Koo, D. Huber, S. Yao, L. Zhang, P. Zhou, J. Maveety, R. Prasher, J. G. Santiago, T. W. Kenny, and K. E. Goodson. Closed-loop electroos-motic microchannel cooling system for vlsi circuits. *IEEE Transactions on Compo-nents and Packaging Technologies*, 25(3):347–355, 2002.

[6] S.N. Heffington, W.Z. Black, and A. Glezer. Vibration-induced droplet atomiza-tion heat transfer cell for high-heat flux applications. *International Conference on Thermal, Mechanics, and Thermomechanical Phenomena in Electronic Systems (ITHERM)*, pages 408–412, 2002.

[7] Engineer's edge - resistance temperature detector (rtd) - instrumentation. *http://www.engineersedge.com/instrumentation/rtd.htm*.

[8] H. Zeng, A. Feinerman, Z. Wan, and P. Pancham. Piston-motion micro-mirror based on electrowetting of liquid metals. *Journal of Microelectromechanical Systems*, 14(2):285, 2005.

[9] 2003 International Technology Roadmap for Semiconductors (ITRS). *Executive Summary*, page 57. 2003.

[10] C.H. Tsai and S.M. Kang. Cell-level placement for improving substrate thermal dis-tribution. *IEEE Transactions on Computer-Aided Design of Integrated Circuits and Systems*, 19:253–266, 2000.

[11] J.M. Rabaey and M. Pedram. *Low Power Design Methodologies*. Kluwer Academic Publishers, 1996.

[12] A.P. Chandrakasan, S. Sheng, and R.W. Broderson. Low power cmos digital design. *IEEE Journal of Solid-State Circuits*, 27:473–484, 1992.

[13] M.G. Pollack, R.B. Fair, and A.D. Shenderov. Electrowetting-based actuation of liquid droplets for microfluidic applications. *Applied Physics Letters*, 77:1725–1726, 2000.

[14] K. Pettigrew, J. Kirshberg, K. Yerkes, D. Trebotich, and D. Liepmann. Performance of a mems based micro capillary pumped loop for chip-level temperature control. *14th IEEE International Con-ference on Micro Electro Mechanical Systems (MEMS 2001)*, pages 427–430, 2001.

[15] M.G. Pollack, A.D. Shenderov, and R.B. Fair. Electrowetting-based actuation of liquid droplets for microfluidic applications. *Lab on a Chip*, 2:96–101, 2002.

[16] T. Sanmarco and M.A. Burns. Thermocapillary pumping of discrete drops in micro-fabricated analysis devices. *American Institute of Chemical Engineers*, 45(2):350–366, 1999.

[17] A. A. Darhuber, J. M. Davis, S. M. Troian, and W. W. Reisner. Thermocapillary actuation of liquid flow on chemically patterned surfaces. *Phys. Fluids*, 15:1295, 2003.

[18] A. A. Darhuber, J. P. Valentino, S. M. Troian, and S. Wagner. Thermocapillary actuation of droplets using microheater arrays. *Journal of Microelectromechical Systems*, 12:873, 2003.

[19] H. Ren, V.K. Pamula, M.G. Pollack, and R.B. Fair. Automated on-chip droplet dispensing with volume control by electro-wetting actuation and capacitance metering. *Sensors and Actuators - B*, 2:319–327, 2004.

[20] V. Srinivasan, V.K. Pamula, and R.B. Fair. An integrated digital microfluidic lab-on-a-chip for clinical diagnostics on human physiological fluids. *Lab on a Chip*, 4:310–315, 2004.

[21] V. Srinivasan, V.K. Pamula, P. Paik, and R.B. Fair. Protein stamping for maldi mass spectrometry using an electrowetting-based microfluidic platform. *Lab-on-a-Chip: Platforms, Devices, and Applications, Conf. 5591, SPIE Optics East*, 2004.

[22] P. Paik, V.K. Pamula, and R.B. Fair. Rapid droplet mixers for digital microfluidic systems. *Lab on a Chip*, 3:253–259, 2003.

[23] P. Paik, V.K. Pamula, and K. Chakrabarty. Coplanar digital microfluidics using standard printed circuit board processes. *9th International Conference on Miniaturized Systems for Chemistry and Life Sciences*, pages 649–654, 2005.

[24] J.A. Skidmore, B.L. Freitas, J. Crawford, J. Satariano, and E. Utterback. Silicon monolithic microchanne-cooled laser diode array. *Applied Physics Letters*, 77(1):10–12, 2000.

[25] E.G. Colgan, B. Furman, M. Gaynes, W. Graham, N. LaBianca, J.H. Magerlein adn R.J. Polastre, and M.B. Rothwell. A practical implementation of silicon microchannel coolers for high power chips. *21st IEEE SEMI-THERM Symposium*.

[26] L.J. Missaggia, J.N. Walpole, Z.L. Liau, and R.J. Phillips. Microchannel heat sinks for two-dimensional high-power-density diode laser arrays. *IEEE Journal of Quantum Electronics*, 25(9):1988–1992, 1989.

[27] D.B. Tuckerman and R.F.W. Pease. High-performance heat sinking for vlsi. *IEEE Electron Device Letters*, 2(5):126–129, 1981.

[28] R.M. Patel, D.K. Wagner, and A.D. Danner. Use of microchannel cooling for high-power two-dimensional laser diode arrays. *SPIE - Laser Diode Technology and Applications IV*, 1634, 1992.

[29] H.Y. Zhang, D. Pinjala, T.N. Wong, K.C. Toh, and Y.K. Joshi. Single-phase liquid cooled microchannel heat sink for electronic packages. *Applied Thermal Engineering*, 25:1472–1487, 2005.

[30] K.L. Yerkes, K. Pettigrew, B. Smith, C. Gamlen, and D. Liepmann. Development and testing of a planar, silicon mini-capillary pumped loop. *Space Technology and Applications International Forum*, pages 81–87, 2002.

[31] M. G. Pollack, P. Y. Paik, A. D. Shenderov, V. K. Pamula, F. S. Dietrich, and R. B. Fair. Investigation of electrowetting-based microfluidics for real-time pcr applications. *The 7th International Conference on Micro Total Analysis Systems (MicroTas 2003)*, 2003.

[32] J. Gong and C.J. Kim. Two-dimensional digital microfluidic system by multi-layer printed circuit board. *Proceedings of IEEE MEMS 2005*, pages 726–729, 2005.

[33] P. Paik, V.K. Pamula, and K. Chakrabarty. Thermal effects on droplet transport in digital microfluidics with applications to chip cooling processing for integrated microfluidics. *International Conference on Thermal, Mechanics, and Thermomechanical Phenomena in Electronic Systems (ITHERM)*, pages 566–568, 2004.

[34] S.K. Cho, H. Moon, and C.J. Kim. Creating, transporting, cutting, and merging liquid droplets by electrowetting-based actuation for digital microfluidic circuits. *IJournal of Microelectromechanical Systems*, 12(1):70–80, 2003.

[35] R. B. Fair, V. Srinivasan, H. Ren, P. Paik, V.K. Pamula, and M.G. Pollack. Electrowetting-based on-chip sample processing for integrated microfluidics. *IEEE Inter. Electron Devices Meeting (IEDM)*, 2003.

[36] P. Paik, V.K. Pamula, M.G. Pollack, and R.B. Fair. Electrowetting-based droplet mixers for microfluidic systems. *Lab on a Chip*, 3:28–33, 2003.

[37] V. Srinivasan, V.K. Pamula, M.G. Pollack, and R.B. Fair. A digital microfluidic biosensor for multianalyte detection. *Proc. of the IEEE MEMS Conference*, pages 327–330, 2003.

[38] V. Srinivasan, V.K. Pamula, K.D. Rao, M.G. Pollack, J.A. Izatt, and R.B. Fair. 3-d imaging of moving droplets for microfluidics using optical coherence tomography. *Proc. of Micro Total Analysis Systems*, 2003.

Biography

Full name: Philip Y Paik
Place of birth: New York, New York
Date of birth: November 15, 1979

Schools attended:

- Duke University, Durham, North Carolina, BSE, May 2001

- Duke University, Durham, North Carolina, MS, May 2003

- Duke University, Durham, North Carolina, PhD, May 2006

Publications:

- P. Paik, V.K. Pamula, and K. Chakrabarty, "Adaptive Hot-Spot Cooling of Integrated Circuits Using Digital Microfluidics ," *ASME International Mechanical Engineering Congress and Exposition (IMECE)*, 2005.

- P. Paik, V.K. Pamula, M.G. Pollack, and K. Chakrabarty, "Coplanar Digital Microfluidics Using Standard Printed Circuit Board Processes," *9th International Conference on Miniaturized Systems for Chemistry and Life Sciences (microTAS)*, 2005.

- P. Paik, V.K. Pamula, and K. Chakrabarty, "Droplet-Based Hot Spot Cooling Using Topless Digital Microfluidics on a Printed Circuit Board ," *International Workshops on Thermal Investigations of ICs and Systems (THERMINICs)*, 2005.

- V. Srinivasan, V.K. Pamula, P. Paik, and R.B. Fair, "Protein Stamping for MALDI Mass Spectrometry Using an Electrowetting-based Microfluidic Platform," *Lab-on-a-Chip: Platforms, Devices, and Applications, Conf. 5591*, SPIE Optics East, Philadelphia, Oct. 25-28, 2004.

- Phil Paik, Vamsee K. Pamula, and K. Chakrabarty. Thermal effects on Droplet Transport in Digital Microfluidics with Applications to Chip Cooling Processing for Integrated Microfluidics. *International Conference on Thermal, Mechanics, and Thermomechanical Phenomena in Electronic Systems (ITherm)*, pp.649-654, 2004.

- R. B. Fair, V. Srinivasan, H. Ren, P. Paik, V.K. Pamula, M.G. Pollack. Electrowetting-based On-Chip Sample Processing for Integrated Microfluidics. *IEEE Inter. Electron Devices Meeting (IEDM)*, 2003.

- Phil Paik , Vamsee K. Pamula and Richard B. Fair, "Rapid droplet mixers for digital microfluidic systems," *Lab on a Chip*, 3, pp. 253-259, 2003.

- M.G. Pollack, P.Y. Paik, A.D. Shenderov, V.K. Pamula, F.S. Dietrich and R.B. Fair. Investigation of electrowetting-based microfluidics for real-time PCR applications. *7th Int'l Conference on Micro Total Analysis Systems (uTAS)*, 2003.

- Phil Paik, Vamsee K. Pamula, Michael G. Pollack and Richard B. Fair. Electrowetting-based droplet mixers for microfluidic systems. *Lab On a Chip*, 3, pp. 28-33, 2003.

- Vamsee K. Pamula, Phil Paik, Jai Venkatraman, Michael G. Pollack, and Richard B. Fair, Microfluidic electrowetting-based droplet mixing. *Presented at MEMS Conference 2001*, Berkeley.

- Jun Chen, Phil Y. Paik, Anthony E. Baer and Lori A. Setton. Static Compression Effects on Cytoskeletal Gene Expression for Cells of the Intervertebral Disc. *Proceedings of the 2001 Annual Meeting of the Biomedical Engineering Society*, 3.9.6, 2001.

- Phil Y. Paik, Jun Chen, Anthony E. Baer, Wei Yan and Lori A. Setton. Extracellular Matrix Gene Expression in Intervertebral Disc Cells Subjected to Altered Osmolarity. *Proceedings of the 2001 Annual Meeting of the Biomedical Engineering Society*, P3.59, 2001.